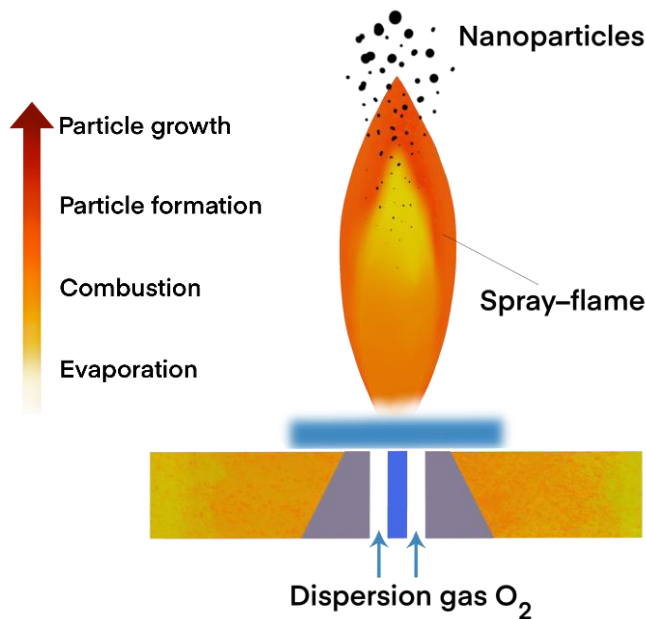
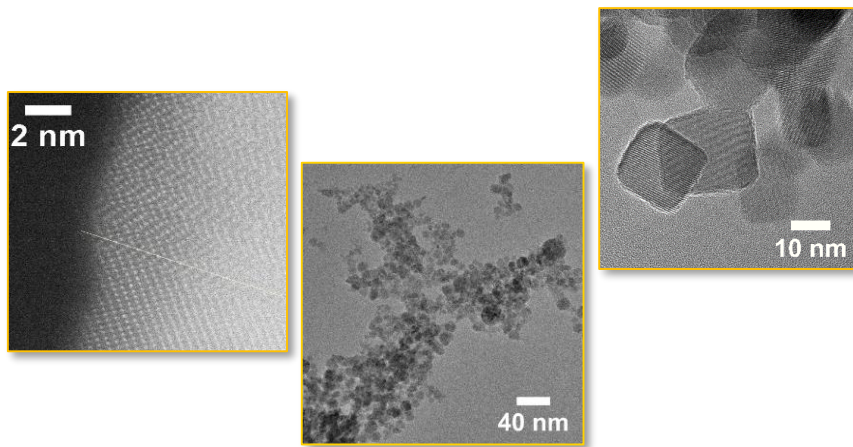


Alexander Tarasov

Spray-flame synthesis of BaTiO₃ nanoparticles for photocatalytic and energy storage applications



**Spray-flame synthesis of BaTiO₃ nanoparticles for photocatalytic
and energy storage applications**

Von der Fakultät für Ingenieurwissenschaften, Abteilung Maschinenbau und Verfahrenstechnik der

Universität Duisburg-Essen

zur Erlangung des akademischen Grades

eines

Doktors der Ingenieurwissenschaften

Dr.-Ing.

genehmigte Dissertation

von

Alexander Tarasov
aus
Moskau, Russland

1. Gutachter: Univ.-Prof. Dr. Christof Schulz
2. Gutachter: Priv.-Doz. Dr. Frank Marlow

Tag der mündlichen Prüfung: 18.06.2020

Zusammenfassung

In der vorliegenden Arbeit wurde die Synthese von ABO_3 -Perowskiten durch Sprayflammsynthese (SFS) untersucht. Das im Fokus stehende Materialsystem war das Perowskit $BaTiO_3$ (BTO), bei dem die A-Position im Gitter von Ba und die B-Position von Ti besetzt sind. Bisher berichten nur wenige Literaturquellen über die SFS von $BaTiO_3$, daher wurden im Rahmen dieser Doktorarbeit geeignete Lösungsmittel, Präkursoren und Syntheseparameter (Konzentration der Präkursoren, Gasflüsse, Reaktordruck) untersucht, um die optimalen Synthesebedingungen zu ermitteln. Die hergestellten Materialien wurden *ex situ* bezüglich ihrer physiko-chemischen Eigenschaften untersucht.

Bei den hergestellten Materialien handelt es sich um nanokristalline $BaTiO_3$ -Pulver, die neben einer Mischung von Materialien mit kubischer und tetragonaler Kristallstruktur auch eine zusätzliche unerwünschte hexagonale Phase aufweisen. Die hexagonale Phase tritt in allen hergestellten Proben auf. Ihre Entstehung wird auf das schnelle Abkühlen des austretenden Partikelstroms durch Vermischen mit Quenchgas zurückgeführt. Die Substituierung der A-Position mit Sr und der B-Position mit Zr hat gezeigt, dass die Herstellung von Materialien je nach Konzentration des substituierten Stoffes ohne die hexagonale Phase möglich ist. Untersuchungen der gebildeten Materialien mit IR-Spektroskopie zeigen, dass die Oberflächen der Materialien mit organischen Spezies verunreinigt sind, die durch unvollständige Verbrennung der Lösungsmittel und Präkursoren entstehen. Eine thermische Nachbehandlung der Pulver nach der Synthese führt zu Materialien mit saubereren Oberflächen und höher Kristallinität mit einem verringerten Anteil der hexagonalen Phase, während die mittlere Partikelgröße auf der Nanoskala bleibt.

Die erzeugten Materialien wurden hinsichtlich ihrer Eigenschaften bezüglich photokatalytischer Wasserspaltung mit UV-Licht (BST, $Ba_{1-x}Sr_xTiO_3$) und kapazitiver Energiespeicherung (BTZ, $BaTi_{1-x}Zr_xO_3$) getestet. Die photokatalytische Aktivität von BTO- und BST-Proben mit und ohne Wärmebehandlungen wurde mit denen einer kommerziellen $BaTiO_3$ -Probe verglichen. Die Ergebnisse zeigen, dass die durch SFS hergestellten Materialien eine zur kommerziellen Probe ähnliche Aktivität aufweisen. Bei der photokatalytischen Aktivität wurde kein nennenswerter Unterschied zwischen wärmebehandelten und nicht wärmebehandelten Proben beobachtet. Um die Energiespeichereigenschaften der Materialien abschätzen zu können, wurden dielektrische Tests an kompaktierten und gesinterten BTZ-Pulvern durchgeführt. Niedrige Zr-Konzentrationen ($x = 0-0.15$) liefern dabei eine gute Kombination aus Dielektrizitätskonstante und von dielektrischen Verlusten ($\tan \delta$). Die Ergebnisse wurden stark von den relativ kleinen Dichten der erzeugten Materialien beeinflusst, die den niedrigeren Sintertemperaturen und Sinterzeiten im Vergleich zu konventionellen Herstellungsmethoden von Keramiken zugeschrieben wurden.

Die vorliegende Arbeit hat gezeigt, dass die Herstellung von komplexen und hochqualitativen Materialien wie Perowskiten durch Sprayflammsynthese möglich ist. Die Flexibilität der Herstellungsmethode wurde durch die gezielte Herstellung variabel ($0 < x < 1$) substituierter Materialien mit den Zusammensetzungen $Ba_{1-x}Sr_xTiO_3$ und $BaTi_{1-x}Zr_xO_3$ nachgewiesen.

Abstract

The production of ABO_3 perovskites via spray-flame synthesis (SFS) was investigated in this thesis. The materials system of interest was the perovskite $BaTiO_3$ (BTO) where the A-site is occupied by Ba and the B-site is occupied by Ti. Considering the scarcity of information on the SFS of $BaTiO_3$, suitable solvents, precursors, and synthesis parameters (precursor concentrations, gas flows, reactor pressure) were investigated to identify appropriate synthesis conditions. The as-synthesized powders were extensively characterized *ex situ* regarding their physico-chemical properties.

It was found that nanocrystalline $BaTiO_3$ powders were produced. They consisted of a mixture of cubic and tetragonal phases but also contained a secondary hexagonal phase. Its formation is attributed to steep temperature gradients downstream of the reaction zone because of the introduction of quenching gas. Atomic substitution of the A-site with Sr and of the B-site with Zr showed that materials without the hexagonal phase can be produced at specific compositions. IR spectroscopy of the as-synthesized materials revealed surface contamination with organic species that originate from incomplete combustion of the solvents and precursors. A post synthesis heat treatment of the powders was shown to aid in obtaining cleaner surfaces and highly crystalline powders with a lower amount of the hexagonal phase, while retaining the nanometer size range. The powders were tested for photocatalytic water splitting ($Ba_{1-x}Sr_xTiO_3$, BST) and capacitive energy storage ($BaTi_{1-x}Zr_xO_3$, BTZ).

Photocatalytic performance of the pristine and heated BTO and BST powders in water splitting was examined and compared to that of a commercial $BaTiO_3$ powder. The results suggest that the spray-flame synthesized powders perform similarly to the commercial sample. Additionally, no significant differences between the catalytic activities of the as-synthesized and heat-treated samples were observed. Dielectric tests were performed on the compacted and sintered BTZ powders to assess the capabilities for capacitive energy storage. Low Zr concentrations ($x = 0-0.15$) were found to deliver a good combination of the dielectric permittivity values and low dielectric losses ($\tan \delta$). However, the results were strongly influenced by the relatively low volumetric density of the materials, which was attributed to the lower sintering temperatures and sintering times compared to those applied in conventional sintering of ceramic materials.

The feasibility of the SFS method towards producing complex and high-quality materials such as perovskites was demonstrated. The flexibility of the spray-flame synthesis method was demonstrated through the selective atomic substitution of the host perovskite material in a wide range ($0 < x < 1$), which opens up new ways for the synthesis of more complex material systems.

Table of contents

List of Symbols.....	VI
Abbreviations.....	VIII
Constants.....	IX
1 Introduction.....	1
2 Materials systems of interest.....	4
2.1 The perovskite ABX ₃ structure.....	4
2.2 BaTiO ₃ and the cation displacement.....	5
2.3 A-site substitution of BaTiO ₃ with Sr ²⁺	7
2.4 B-site substitution of BaTiO ₃ with Zr ⁴⁺	7
3 Photocatalytic energy conversion and capacitive energy storage in BaTiO₃-based perovskites.....	11
3.1 Semiconductor photocatalysis.....	11
3.1.1 Fundamentals of photochemistry.....	11
3.1.2 Photochemical water splitting.....	13
3.1.3 Materials requirements for photocatalysts towards water splitting.....	14
3.1.4 Titanate-related perovskites for photocatalytic water splitting.....	16
3.2 Capacitive energy storage.....	17
3.2.1 Working principle of capacitors.....	18
3.2.2 Classification of <i>P-E</i> curves in relation to energy storage.....	20
3.2.3 BaTiO ₃ -related perovskites for capacitive energy storage.....	22
4 Gas-phase synthesis of nanoparticles.....	24
4.1 Nucleation.....	25
4.2 Coagulation and coalescence.....	26
4.3 Spray-flame reactor.....	27
5 Characterization methods.....	29
5.1 X-ray diffraction (XRD).....	29
5.2 Transmission electron microscopy (TEM).....	31
5.3 Raman spectroscopy.....	32
5.4 Fourier transform infrared spectroscopy (FTIR).....	33
5.5 Specific surface area measurements (BET).....	35
5.6 Thermogravimetric analysis (TGA).....	36
6 Experimental results.....	38
6.1 Synthesis of BaTiO ₃ nanoparticles.....	38
6.1.1 Investigation of process parameters, solvents, and precursors.....	38
6.1.2 Investigation of the influence of solvent composition.....	48
6.2 Synthesis of Ba _x Sr _{1-x} TiO ₃ nanoparticles.....	54
6.2.1 Characterization of as-synthesized Ba _x Sr _{1-x} TiO ₃ powders.....	55
6.2.2 Characterization of heat-treated Ba _x Sr _{1-x} TiO ₃ powders.....	59

6.3	Photocatalytic water splitting of $\text{Ba}_{1-x}\text{Sr}_x\text{TiO}_3$ nanoparticles.....	65
6.3.1	Photocatalytic reactor setup.....	65
6.3.2	Photocatalytic tests and discussion.....	66
6.4	Synthesis of $\text{BaTi}_{1-x}\text{Zr}_x\text{O}_3$ nanoparticles.....	67
6.4.1	Characterization of as-synthesized $\text{BaTi}_{1-x}\text{Zr}_x\text{O}_3$ powders.....	68
6.4.2	Powder compaction and sintering.....	70
6.4.3	Characterization of sintered $\text{BaTi}_{1-x}\text{Zr}_x\text{O}_3$ pellets.....	71
6.5	Dielectric measurements of $\text{BaTi}_{1-x}\text{Zr}_x\text{O}_3$ pellets	76
7	Conclusions	80
	Appendix	82
	Literature	83
	List of publications and conferences.....	95
	Acknowledgements.....	96

List of Symbols

Symbol	Meaning	Unit
ΔG	Gibbs free energy	J
A	Capacitor plates area	m ²
a_{ij}	Radii of the colliding particles	m
C	Capacitance	F
d	Dielectric layer thickness	m
D	Electric displacement	C/m ²
D	Diffusion coefficient	m ² /s
d	Distance between two diffracting planes	Å
d	Resolution	m
d_p	Penetration depth of the radiation	m
d_p	Particle size	nm
E	Electric field	V/m
e_i	Atomic charge	C
f	Friction coefficient	kg/s
ΔH	Combustion enthalpy	kJ/mol
I	Intensity of Raman scattering	-
m	Particle mass	kg
M	Molar concentration	mol/L
M	Molecular weight of the adsorbate	g/mol
n	Number of clusters	-
n_A	Number of moles in vapor	-
n_B	Number of moles in cluster phases	-
n_c	Refractive index of the ATR-FTIR crystal	-
$N_{i,j}$	Collision frequency of two particles	-
n_s	Refractive index of the sample	-
P	Electric polarization	C/m ²
p	Vapor pressure of the species	Pa
P	Adsorbate pressure	Pa
P_0	Saturation pressure of the fluid	Pa
ρ_p	Particle density	g/cm ³
p_s	Equilibrium vapor pressure	Pa
Q	Electric charge	C
r	Radius of a cluster	m
r	Atomic position	m

S	Saturation	-
T	Temperature	K
t	Time	s
$\tan \delta$	Loss tangent	-
U	Energy density	J/m ³
U	Applied acceleration voltage	V
V	Voltage	V
V	Volume	m ³
W	Weight of the incompletely adsorbed monolayer	kg
W_m	Weight of the completely adsorbed monolayer	kg
α	Polarizability	C m ² /V
δ	Surface charge density	C/m ³
δ	Surface tension	J/m ²
δ	Specific surface area	m ² /g
ε	Absolute dielectric permittivity	-
ε_r	Relative permittivity of the dielectric material	-
η	Energy storage efficiency	-
θ	Angle	°
Θ	Surface Coverage	-
λ	Wavelength	nm
μ	Electric dipole moment	C m
μ_A	Chemical potential of the liquid phase	J/mol
μ_B	Chemical potential of the vapor phase	J/mol
v	Particle velocity	m/s
$v_{i,j}$	Particle volumes	m ³
ρ	Density of a material	kg/cm ³
τ_c	Characteristic collision time	s
τ_f	Characteristic sintering time	s
χ	Electric susceptibility	-
$\overline{\chi^2}$	Mean square displacement	m ²
T_{bp}	Boiling point of a solvent	°C
T_{mp}	Melting point of a precursor	°C

Abbreviations

AFE	Antiferroelectric
ATR	Attenuated total reflectance
BG	Band gap
BST	Barium strontium titanate
BTO	Barium titanate
BTZ	Barium titanium zirconate
CB	Conduction band
CMD	Count median Diameter
DPT	Diffuse phase transition
DSC	Differential scanning calorimetry
EDX	Energy-dispersive X-ray spectroscopy
EELS	Electron-energy loss spectroscopy
FASP	Flame-assisted spray pyrolysis
FE	Ferroelectric
FSP	Flame-spray pyrolysis
FWHM	Full width at half maximum
HER	Hydrogen evolution reaction
ICSD	Inorganic crystal structure database
IR	Infrared radiation
OER	Oxygen evolution reaction
PNR	Polar nanoregions
PSD	Particle-size distribution
PVDF	Polyvinylidene fluoride
QMS	Quadropole mass spectrometer
RFE	Relaxor ferroelectric
SEM	Scanning electron microscopy
SFS	Spray-flame synthesis
slm	standard liter per minute
SR	Surface recombination
SSA	Specific surface area
STEM	Scanning transmission electron microscopy
STO	Strontium titanate
TEM	Transmission electron microscopy
TGA	Thermogravimetric analysis
UV	Ultraviolet
VB	Valence band

VR Volume recombination
XRD X-ray diffraction

Constants

k_B	Boltzmann constant	$1.3806488 \times 10^{-23} \text{ J/K}$
N_A	Avogadro constant	$6.02214129 \times 10^{23} \text{ mol}^{-1}$
h	Planck constant	$6.62 \times 10^{-34} \text{ J s}$

1 Introduction

The term “nanotechnology” was first indirectly coined by Richard P. Feynman in 1959 while addressing the problems of miniaturization and prospects of investigating “small” things on the scale of individual atoms [1]. It was not until the early 1980s when the first scanning tunneling microscope was developed, which provided enough resolution to observe single atoms, thus marking the actual beginning of the nanotechnological era. Meanwhile, the official definition of nanotechnology describes it as a manipulation of a system which has at least one dimension sized from 1 to 100 nm. The word “system” in this case implies a material where at least one dimension falls into the nano-range. If all three dimensions are on the nanoscale, such system is called a nanoparticle and is a special case of nanomaterials [2].

Owing to their dimensions, nanoparticles possess new unique properties (e.g., increased catalytic activity, tunable optical absorption and electronic properties, improved mechanical properties) compared to their “bulk” counterparts, which has already opened up new horizons for the application of the former in diverse areas such as microelectronics, pharmacy, chemistry, catalysis, etc. [3]. Of particular importance today is the issue of sustainable energy conversion and storage, which would facilitate the use of regenerative energy sources and thus minimize the detrimental impact on the environment caused by the extensive use of fossil fuels. This topic motivates researchers to put a lot of effort into the design and investigation of functional nanomaterials with pre-defined performance characteristics [4].

Among diverse groups of nanomaterials (binary metal oxides, carbon-based materials, etc.), perovskite materials are considered particularly interesting in the context of catalysis (oxygen evolution reaction [5]), energy conversion (solar cells [6]), and energy storage (ceramic capacitors [7]). Perovskites are a class of crystalline materials described by the ABX_3 chemical formula, where A is a large cation, B is a medium-sized cation and X is an anion. This results in a large number of possible compositions within the perovskite family with remarkable catalytic, dielectric, magnetic, electric, thermal, and optical properties [8]. One of the greatest advantages of the perovskite structure is its flexibility that allows substitution of the A, B, and X sites, where the former two are typically metal ions and the latter can be occupied by C, N, O, organic molecules, and halides. This, for example, provided ground for the rapid emergence of the hybrid organic-inorganic perovskites for high-efficiency photovoltaic devices [6, 9].

The oxygen atom on the X site gives rise to another large class of perovskite materials – perovskite oxides with the idealized cubic perovskite structure embodied by the mineral $CaTiO_3$, which in turn belongs to a prominent subclass of titanate perovskites, where the B site is occupied by a Ti atom. A particular research interest in the titanate-based type of perovskites dates back to the 1940s, when $BaTiO_3$ ceramics were employed in capacitors owing to their excellent dielectric properties [10]. Some well-known derivatives of the $BaTiO_3$ structure like $PbZr_xTi_{1-x}O_3$ or $Ba_{1-x}Sr_xTiO_3$ have been extensively studied since then towards improving dielectric performance in connection with capacitive energy storage [7, 10-14]. Today, the focus is directed on the downscaling of energy storage device while increasing their volumetric efficiency, which necessitates the use of nanograined ceramics with enhanced dielectric properties [15]. In this respect, perovskite materials on the $BaTi_{1-x}Zr_xO_3$ basis are considered promising due to their strong performance characteristics such as high dielectric permittivity and low energy losses, combined with an environment-friendly nature [12-14]. Furthermore, interest has grown in recent years in highly active catalytic nanomaterials for energy conversion that provide adequate performance [16]. This allowed some of the members of the titanate perovskite family (e.g., $SrTiO_3$) to emerge as potent catalysts for hydrogen production through electrocatalytic water splitting [17-19], electrocatalytic CO_2 reduction [20], and water decontamination [21]. Despite these recent developments, the overall research

on titanate-based perovskites regarding catalytic applications remains incomplete. For instance, only a handful of works is present in the literature describing photocatalytic performance of titanate-based perovskite systems such as BaTiO_3 and its derivatives [19, 22-24].

A question of significant importance is to develop suitable synthesis methods that enable reliable production of nanoparticles. Conventional methods can be divided into three approaches: solid-state, wet chemistry, and gas-phase techniques [25]. Solid-state synthesis deals mostly with high-temperature (close to the melting points of initial substances) reactions of metal salts, sometimes yielding inhomogeneous, highly agglomerated, and sintered powders in the micrometer-size range [26, 27]. Established wet chemistry techniques are in position to yield monodisperse powders in the nanometer range, but require additional calcination steps after the synthesis to remove residual organics and to improve crystallinity of the material [28, 29]. Diverse forms of hydro- and solvothermal processes allow precise control over the particle size distribution and compositional range [30, 31], but have potential problems like organic contaminations and the requirement of stringent reaction conditions [21, 25]. Another point to consider is the scalability of the mentioned techniques, which is usually limited to batch-like production [32]. However, it has been shown recently that solvothermal approaches can deliver industry-scale production rates [25].

Alternatively, gas-phase methods can also be applied to the production of nanoparticles, for example, microwave plasma synthesis, hot-wall reactor processing, and combustion-based methods [33, 34]. Combustion techniques, specifically spray-flame synthesis (SFS or also known as flame-spray pyrolysis, FSP), takes advantage of the energy that is supplied by burning solvents in order to force metal precursor species into the gas phase and is appropriate for the production of various oxide materials with the prospect to be scalable to generate commercial materials quantities [35, 36]. The benefits of using SFS is that it provides good control over the following properties: particle size in the nanometer range, crystallinity, and phase composition of the final products [37-41]. An additional strength of SFS is that it offers the option of performing a reliable and relatively straightforward wide-range doping/substitution as a part of a continuous process [42, 43]. In brief, the SFS method is a combustion process in which a premixed pilot flame (typically CH_4/O_2 or H_2/O_2) stabilizes a turbulent spray flame that is fueled by a dispersed solution (spray) containing dissolved metal precursors and solvents, which is continuously fed into the reactor. High temperatures of the burning spray lead to the evaporation of the dissolved metal precursors and subsequent gas-phase reactions, whereby particles form and undergo growth processes [33, 34]. One of the benefits of the method is a possibility to flexibly vary both solution compositions and synthesis parameters, which gives the operator a wide spectrum of combinations to directly control the properties of the final product. In the SFS environment, it is possible to synthesize and preserve metastable phases through rapid cooling of the particle-laden gas mixture after the reaction, which are otherwise not attainable by any other synthesis technique [42, 44].

Extensive literature exists describing synthesis of nanoparticles via SFS starting from the pioneering works of Ulrich [45, 46] on fumed silica. Meanwhile, many binary oxides like TiO_2 , Fe_2O_3 , Al_2O_3 , ZnO [35], NiO/CoO catalysts [47] have been synthesized and studied in detail, and the research has been extended since to encompass more complex systems like LiFePO_4 [48], $\text{Li}_7\text{Ti}_5\text{O}_{12}$ [49], and some perovskites as well, mostly restricted to LaCoO_3 -related systems for catalysis [42, 50-55].

The number of works on titanate perovskites produced via SFS is rather modest and is restricted to pure BaTiO_3 . Kudas and Brewster [56] were the first to describe the synthesis of BaTiO_3 via flame-assisted spray pyrolysis (FASP) technique, which is essentially a spray-drying process [57, 58], where a flame

is used¹ instead of a furnace as a heat source. The authors reported production of the powders with a particle size around 200–500 nm with tetragonal and hexagonal phases present, the latter being an undesired secondary phase. The occurrence of the hexagonal phase was attributed to the high temperatures of the flame. Purwanto *et al.* [59] and Terashi *et al.* [60] also showed the synthesis of BaTiO₃ nanoparticles with FASP and confirmed particle sizes around 100 nm and the emergence of the hexagonal phase along with a barium carbonate BaCO₃ by-product impurity, which is routinely detected in as-synthesized powders. Choi *et al.* [61] described production of core–shell Ag-BaTiO₃ composite nanopowders using FASP. They report low crystallinity of the as-synthesized powders, which can be improved in a subsequent prolonged powder calcination step starting at temperatures around 600°C and above. Recently, Schädli *et al.* [62] reported the production of BaTiO₃ nanoparticles using an SFS setup with a H₂/O₂ flame in order to reduce the amount of CO₂ in the off-gas compared to the conventional methane combustion reaction and to provide more energy for the spray combustion and therefore facilitate formation of highly-crystalline carbonate-free particles. In addition, they investigated the influence of the reactor tube length on the particle size and crystallinity of the powders. They found that the freshly-prepared powders demonstrate a multi-phase system with a significant amount of amorphous product and carbonates. Changing the reactor length helps anneal the powders *in situ*, which resulted in larger particle sizes (24 versus 51 nm before and after increasing the height, respectively), but also allowed to decrease the number of unwanted by-products and secondary phases. No literature references regarding the substitution of the host BaTiO₃ and related systems in the SFS or related processes have been found so far, which together with the outlined challenges (contaminations, phase impurity) is the driving motivation for the present research. Expectedly, no information on the use of the flame-synthesized titanate perovskites in either photocatalysis or as dielectric material in ceramic capacitors were found in the literature, which strengthens the motivation behind the present work. Therefore, in this study, barium titanate (BaTiO₃, further referred to as BTO), barium strontium titanate (Ba_{1-x}Sr_xTiO₃, referred to as BST), and barium zirconium titanate (BaTi_{1-x}Zr_xO₃, referred to as BTZ) were chosen to examine applicability of the SFS technique to the synthesis of the named materials. Obtained results should help in establishing a deeper understanding and providing insight in the SFS of various titanate systems and perovskite oxides in general.

The focus of this work is to investigate the synthesis of BaTiO₃ nanoparticles and related systems (BaTiO₃, substituted with Sr on the Ba site and Zr on the Ti site) using the SFS technique. In order to obtain a profound understanding of the process, it was vital to conduct experiments describing the synthesis of pure BaTiO₃ powders while varying process parameters and/or solvent compositions to find any correlation between them and particles properties. Another important integral part of the present work is to understand if a desired substitution with various elements during the SFS process can be successfully performed. The synthesized powders were extensively characterized in connection with their performance as photocatalysts for water splitting reaction (Ba_{1-x}Sr_xTiO₃) or dielectric materials for capacitive energy storage (BaTi_{1-x}Zr_xO₃).

¹ The fundamental difference between SFS and FASP is that in the former, the particle formation succeeds through gas-to-particle process, which makes it a gas-phase process. In the latter particles are formed by droplet-to-particle conversion process, hence spray drying [33]

2 Materials systems of interest

Through the course of this chapter, the perovskite structure and some of the most important concepts describing the relation between structure and properties are examined. The main focus is on introducing BaTiO₃ and related systems. Additionally, approaches to structural modifications through substitution of the atoms of the host BaTiO₃ perovskite are considered with two particular substitution cases (Sr²⁺ on the Ba site and Zr⁴⁺ on the Ti site) examined in detail.

2.1 The perovskite ABX₃ structure

The ABX₃ formula is used for a general description of the elemental composition of perovskite crystals, where the A site is occupied by a large cation, the B site is a medium-sized cation, and X is an anion, in most cases oxygen but not exclusively [8]. A typical perovskite structure is usually visualized by SrTiO₃ as a prototype, a system very similar to BaTiO₃. At room temperature, SrTiO₃ adopts a cubic structure with a characteristic *Pm3m* space group, where Sr atoms occupy the corners of the unit cell with a Ti atom placed in the center of the unit cell surrounded by six oxygen atoms, thus forming an octahedron, as shown in Figure 2-1a. Typically, the cell origin is translated to the Ti atoms, which then renders the structure as a framework consisting of an array of regular corner shared BO₆ octahedra or TiO₆ in the case of SrTiO₃. This is especially useful for comparison purposes of various perovskite structures, since they are built up from the stacked sequences of BO₆ octahedra (Figure 2-1b).

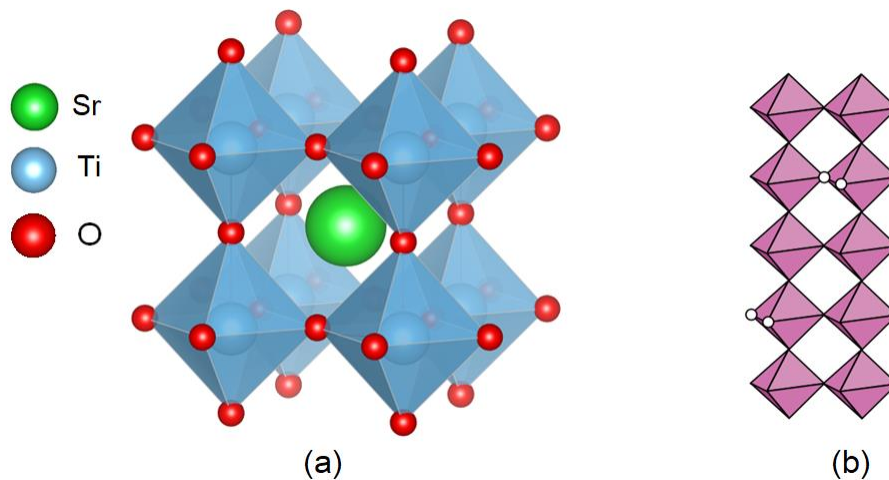


Figure 2-1. (a) ABO₃ perovskite structure of SrTiO₃, (b) stacking sequence of BO₆ octahedra in a conventional perovskite. Adapted from [8].

Perovskite structures are frequently viewed as ionic crystals, which need to maintain electroneutrality to be thermodynamically stable. Consequently, a combination of two ions of various sizes has important implications for the structure and therefore its properties. The merit of how likely they form a stable perovskite structure can be described through the so-called tolerance factor (Goldschmidt's rule):

$$t = \frac{(r_A + r_X)}{\sqrt{2}(r_B + r_X)} \approx 1 \quad \text{Equation 2-1}$$

where r_A is the radius of the A-site cation, r_B is the radius of the B-site cation and r_X is the radius of the anion (X) [8]. The idea behind the tolerance factor is that a perovskite structure would form when the

value of t is close to 1. The Goldschmidt factor is used extensively to predict if a structure is more likely to converge to the ideal cubic structure of SrTiO₃ ($t \approx 0.9$ – 1.0), hexagonal ($t > 1.0$), or to other lower symmetry phases such as tetragonal, rhombohedral, and orthorhombic ($t \approx 0.71$ – 0.9) [63]. Decreasing the t value generally corresponds to an increased disorder of the structure, and thus deviation from the ideal perovskite configuration shown in Figure 2-1b [64].

The tolerance factor holds a reasonable predictive power for the theoretical analysis of perovskite structures and their stability. For instance, in the case of organic–inorganic halide perovskites, where the structures with t values of 0.8 – 1 possess the key photoactive phase, and the structures whose t values lie slightly beyond these values demonstrate compositional disorder, which leads to the formation of secondary phases that negatively affect the performance [9].

2.2 BaTiO₃ and the cation displacement

Many valuable properties of conventional ABO₃ perovskites are determined by the chemistry of the BO₆ octahedra, specifically by the electron configurations of the B-site cations. In contrast, the larger A-site cations are chemically less responsive and serve as a framework for the BO₆ octahedra. For instance, a change in the oxidation state of the B-site cation or introduction of B-site cations with different oxidation states might result in stoichiometries ranging from the standard ABO₃ to non-stoichiometric, oxygen-deficient ABO_{3- δ} compositions. The final structure in these cases is stabilized by introducing oxygen vacancies and a corresponding change in the coordination of the BO₆ octahedra [63, 64].

In reality, any structural modification of the principal ABO₃ stoichiometry is accompanied by either or a combination of the following changes in the BO₆ chemistry: B-cation displacement, BX₆ octahedra tilt/rotation or BX₆ distortion (elongation or flattening) [8]. B-site cation displacement is the one most frequently observed of the three and is very well studied on the example of BaTiO₃, which is considered more closely in the present chapter.

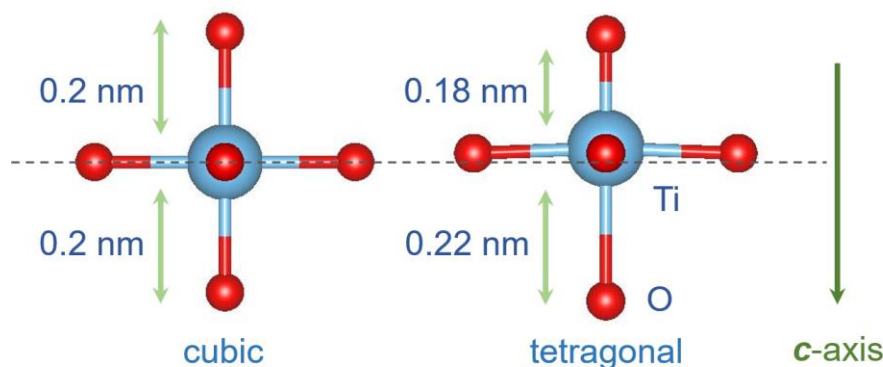


Figure 2-2. Comparison between TiO₆ octahedra in the cubic and tetragonal phases of BaTiO₃.

A classic example of the BO₆ displacement is the displacement of the Ti⁴⁺ ions of the TiO₆ octahedra in BaTiO₃ caused by the second-order Jahn-Teller effect, which states that symmetry deviations occur that help minimize the ground-state energy of the system with a non-degenerate electronic ground state under the influence of a sufficiently low-lying excited state [65]. In more simple terms, even for high-symmetry systems such as a cubic system in a ground state, symmetry distortions are favorable to preserve the minimum energy state driven by the improved covalent bonding between the highest occupied (HO) and lowest occupied (LO) molecular orbitals. In BaTiO₃ this is realized by the coupling between the 3d

orbitals of the Ti^{4+} and the highly electronegative oxygen $2p$ orbitals [8, 66-68]. Therefore, to preserve the minimal energy state and at the same time to retain the highest possible symmetry, a displacement along one axis happens to compensate for the excess energy provided by the unfavorable initial electron configuration. To demonstrate the implications this effect has on the structure, a projection of the corresponding TiO_6 octahedra of the cubic and tetragonal phase of BaTiO_3 are shown in Figure 2-2.

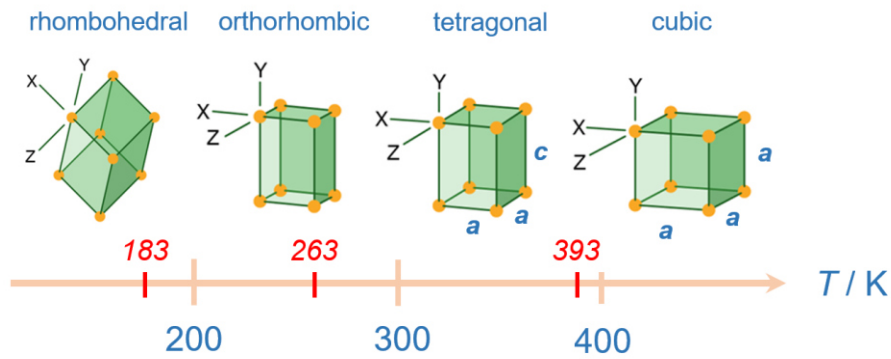


Figure 2-3. Phase transitions of BaTiO_3 . Red mark ticks indicate the respective phase-transition temperatures.

The cubic structure of BaTiO_3 with the highest symmetry (space group $Pm\bar{3}m$) is thermodynamically stable at temperatures above 393 K (120°C) (Figure 2-3), with the six Ti–O bond lengths being equal to 0.2 nm in each octahedron (Figure 2-2). As the system cools down below 393 K, a phase transition into the lower symmetry tetragonal phase (space group $P4mm$) occurs as the cubic structure can no longer be retained because of the above described second-order Jan-Teller effect. The consequence is that the Ti–O bond lengths adjust (either lengthen or shorten), also leading to a unit cell expansion along the c axis, while the two remaining a axes slightly compress (Figure 2-3) [69]. The displacement of the Ti^{4+} ions happens along the c axis and the bond lengths parallel to the c axis are ~ 0.22 and 0.18 nm, while the equatorial bond lengths remain ~ 0.2 nm and thus the average bond length across the unit cell stays 0.2 nm (Figure 2-2). The ultimate effect of the cation displacement is that it gives rise to dielectric dipoles in each TiO_6 octahedron owing to the polar nature of the Ti–O bond, which is the source of a spontaneous electric polarization (ferroelectricity) in tetragonal BaTiO_3 . Thus, changes in the chemical environment of the BO_6 octahedra have a profound influence on the structure and properties not only in BaTiO_3 but also in any other perovskite system [69-71]. With further temperature decrease, the tetragonal structure of BaTiO_3 undergoes subsequent phase transitions, which leads to systems with even lower symmetry (orthorhombic and rhombohedral phases) accompanied by changes in unit cell dimensions and bond lengths. Both phases display ferroelectric properties, and the former occurs between 263 and 183 K, while the latter is found below 183 K [8] (Figure 2-3).

It is important to understand that phase transitions can not only be induced by changing temperature. Intentional manipulation of the ABO_3 perovskite structure can be achieved by performing substitutions on either A- or B- site with generally two main aspects considered: ionic radius and valency of the substituting elements. While discussing numerous individual cases of structural variations is beyond the scope of this thesis, some cases of structural modifications of the BaTiO_3 perovskite structure are examined, specifically how one can customize and tailor the properties of interest.

2.3 A-site substitution of BaTiO₃ with Sr²⁺

Possible substitution cases of BaTiO₃ on the A-site are generally described in terms of introducing elements from group 2 of the periodic table (alkaline earth metals), which gives rise to perovskites like MgTiO₃, ZnTiO₃, CaTiO₃, and SrTiO₃. For instance, MgTiO₃ is known for its dielectric properties and is used in electronic filters, resonators, and microwave antennas [72, 73], while ZnTiO₃ is used as a catalyst for dehydrogenation reactions and oxidation of chemical wastes [74], and has been also examined regarding its photocatalytic performance [75]. A disorder-engineered CaTiO₃ was shown to demonstrate good photocatalytic activities in dye degradation compared to the unmodified samples [76]. Substitution of the A-site with Sr produces a series of technologically important materials owing to their excellent dielectric performance [7, 77-79]. Moreover, pure SrTiO₃ nanoceramics have received substantial attention in catalytic community due to their reliable hydrogen production in water splitting reaction, coupled with its stability and favorable band-edge positions [80, 81], which strengthens the interest in investigating synthesis of SrTiO₃ nanopowders for photocatalytic applications. Their catalytic performance can be further boosted by adding co-catalysts like Ni, Pd, or Rh [18, 19, 82-84].

The similarity between BaTiO₃ and SrTiO₃ is apparent with the former having a slightly expanded unit cell compared to the latter (3.9906 Å and 3.905 Å, respectively) due to the difference in the ionic radii: Sr²⁺ ion is slightly smaller than Ba²⁺ (1.44 Å versus 1.61 Å, respectively) [78]. Therefore, at room temperature, SrTiO₃ possesses an ideal cubic perovskite structure (*Pm3m*) and is not ferroelectric – a fact that is additionally emphasized by the Goldschmidt tolerance factor ~ 1 . This also means that introduction of Sr does not directly interfere with the TiO₆ octahedra chemistry observed in BaTiO₃. Both SrTiO₃ and BaTiO₃ share almost identical electronic structures with an indirect band-gap of ~ 3.2 eV [81]. Substitution of BaTiO₃ with Sr shows complete solubility and creates a homogenous solid solution with no secondary phases over the whole composition range [85]. Upon introduction of Sr, the tetragonal phase of BaTiO₃ is preserved at room temperature up to at least 15 mol% Sr [78] although the degree of tetragonal distortions (the ratio between the *c* and *a* cell constants) diminishes with increasing Sr concentration [86]. Further increase in Sr concentration converts the structure completely into cubic with a linear decrease in the calculated cell constant values [25].

So far, the synthesis of SrTiO₃ via SFS has not been reported in the abundant literature on the various, mostly wet-chemistry synthesis methods of SrTiO₃ [25, 83, 86]. It is therefore the goal of this thesis to investigate the feasibility of producing SrTiO₃ and Sr-substituted BaTiO₃ nanoceramics via SFS, and to examine their performance in water splitting reaction regarding hydrogen production.

2.4 B-site substitution of BaTiO₃ with Zr⁴⁺

The number of options regarding the substitution of the B-site in BaTiO₃ is typically limited to the elements from groups 4, 5, 8, and 9 of the periodic table that have a similar ionic radius to Ti (0.605 Å). That leads, for instance, to the following well-known systems: BaZrO₃, BaSnO₃, BaFeO₃, and BaCoO₃, though some additional combinations are possible. BaSnO₃ finds its use as an electrode for organic solar cells, in gas sensors, and as a thin-film transistor [87], while Ba(Fe,Co)O₃ perovskites are known for their conductive properties for cathode materials in solid oxide fuel cells [88]. Since the focus in the present work is directed on the substitution of the B-site towards capacitive energy storage, the only viable option from the mentioned systems above is Zr, therefore leading to BaTi_{1-x}Zr_xO₃. This system received much attention owing to its strong dielectric characteristics, which render it attractive for energy storage applications in ceramic capacitors [12-14, 89]. In addition, the emergence of the diffuse

phase transition (DPT) and relaxor behavior gives the $\text{BaTi}_{1-x}\text{Zr}_x\text{O}_3$ system another edge in the topic of capacitive energy storage, where materials with pure ferroelectric characteristics suffer from pronounced hysteretic behavior despite their strong permittivity values [7]. This is not the case for DPT and relaxor-based ceramics, because hysteretic behavior is much less pronounced due to the partial or total absence of the seamless domain structure, which therefore allows to store higher amount of electric energy in a ceramic material. The topic of ferroelectric hysteresis and its importance for energy storage is addressed in greater detail in Chapter 3.2. An additional significant benefit is that $\text{BaTi}_{1-x}\text{Zr}_x\text{O}_3$ (BTZ) is non-toxic unlike its lead-containing analogues (e.g., $\text{Pb}(\text{TiZr})\text{O}_3$ or $(\text{Pb,Lu})(\text{Ti,Zr})\text{O}_3$), which are being skeptically viewed due to environmental and safety concerns [7]. In this chapter the key features of the BTZ systems are concisely summarized that would help understand what makes it stand out when compared to BaTiO_3 with respect to energy storage applications.

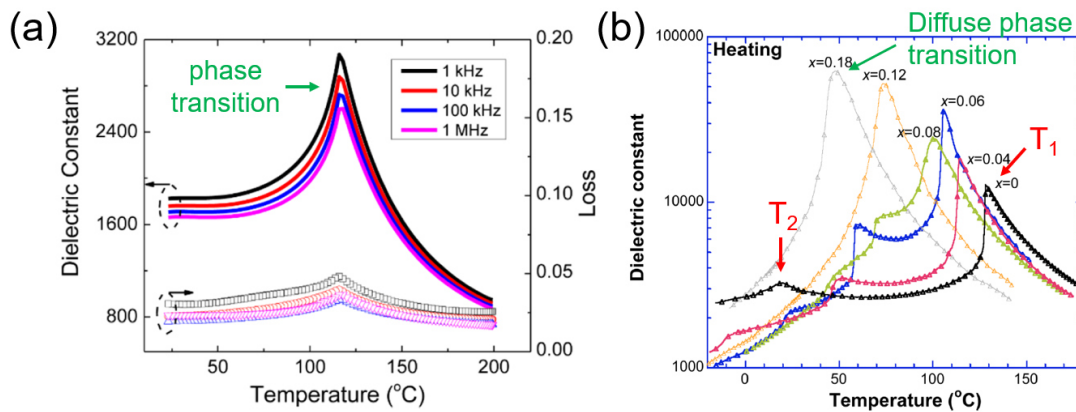


Figure 2-4. Temperature dependence of the dielectric constant and losses for pure BaTiO_3 (a) and $\text{BaTi}_{1-x}\text{Zr}_x\text{O}_3$ ceramics with various Zr concentrations (b). Arrows indicate phase transitions, T_1 and T_2 stand for transition 1 (tetragonal/cubic) and 2 (orthorhombic/tetragonal), respectively. Adapted from [89, 90].

As described in Chapter 2.2, ferroelectricity in the tetragonal phase of BaTiO_3 occurs through the displacement of Ti^{4+} ions, which ultimately renders every TiO_6 octahedra a dipole. Neighboring dipoles are polarized and an aligned array of dipoles with identical orientation is called a ferroelectric domain, which contributes to the spontaneous polarization of the material. Domains are formed to minimize the electrostatic energy associated with an uneven distribution of the spontaneous polarization throughout the material, therefore forming a long-range ferroelectric order. An important fact is that any ferroelectric material can be turned into a non-ferroelectric material (paraelectric) through an induced phase transition, for instance, by applying heat. The phase transition is accompanied by a strong change in the dielectric permittivity values and changes in the unit-cell dimensions dictated by the symmetry of the system, as discussed in Chapter 2.2. The observed change of the dielectric permittivity versus temperature is described by the Curie-Weiss law, and the temperature at which the peak permittivity is registered is called the Curie temperature (T_C). A typical example of that is shown in Figure 2-4a.

A different case emerges when taking into account the incorporation of Zr substituting Ti atoms (ionic radii 0.72 Å and 0.605 Å, respectively [91]) in BaTiO_3 . Briefly, introduction of Zr leads to the development of local inhomogeneities so that a ferroelectric domain is made up of microregions, each with a slightly different distribution of Zr and Ti, which in turn leads to the breakage of the long-range ferroelectric order. These microregions were shown to have nanometer dimensions (2–10 nm) and demonstrate only locally correlated polarizations and therefore are called polar nanoregions (PNR) [92]. Each such PNR has a slightly different T_C value from its neighbors, which results in a significant broadening of the

permittivity maximum – frequently described as a diffuse phase transition (DPT), as shown in Figure 2-4b for $x = 0.18$ [8, 92]. The phase composition has a profound influence on the existence of PNRs and therefore dielectric properties of substituted $\text{BaTi}_x\text{Zr}_{1-x}\text{O}_3$ ceramics depend on the Zr concentration. The first event to occur is that phase transitions of various ferroelectric phases (tetragonal/cubic and orthorhombic/tetragonal, T_1 and T_2 , respectively) in pure BaTiO_3 (Figure 2-4b) draw closer to each other at $x \leq 0.1$. At $x \approx 0.1-0.15$, the T_1 and T_2 phase transitions completely merge – a phenomenon frequently called a “pinched phase transition”, and the system is then said to preserve a rhombohedral symmetry up to $x \approx 0.2-0.25$, which is still actively discussed in the literature [89, 92-94]. At the same time as the pinched phase transition occurs, the DPT phenomenon can be observed over $x \approx 0.15-0.25$ in Zr-substituted BaTiO_3 , which is no longer correctly described by the Curie-Weiss law, and the maximum permittivity value is simply denoted as T_m . It should be stressed that despite DPT, the material’s behavior is still regarded as a pure ferroelectric one.

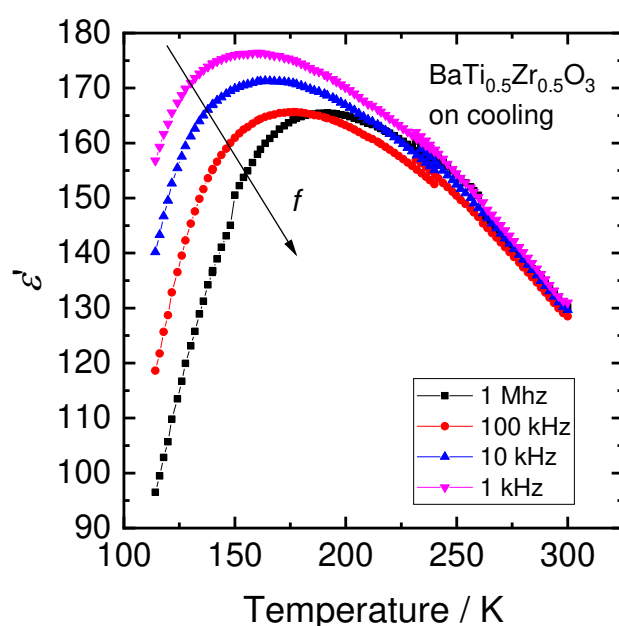


Figure 2-5. Temperature dependence of the dielectric permittivity (ϵ') for $\text{BaTi}_x\text{Zr}_{1-x}\text{O}_3$ with $x = 0.5$.

At higher substitution stages with Zr concentration $x \approx 0.25-0.35$, a transition (crossover) to a so-called relaxor state occurs. The relaxor state is described by the frequency dispersion of the dielectric permittivity values, as shown for $x = 0.5$ by the arrow in Figure 2-5. The origin of the frequency dispersion is related to the kinetics of the reorientation process of PNRs during cooling, which is a frequency-dependent process [92, 93]. However, there is still some controversy regarding the phase composition at room temperature at $x \approx 0.25-0.35$. For instance, Buscaglia *et al.* [95] showed that at $x = 0.2$ the rhombohedral phase can coexist with the cubic phase. Miao *et al.* [94] argue that at $x = 0.25$ and 0.35 , the cubic structure prevails with rhombohedral-like distortions. Maiti *et al.* [93] conducted dielectric permittivity experiments with various Zr concentrations and proposed a phase diagram, suggesting that the materials at $x > 0.25-0.35$ are macroscopically cubic judging from the measured neutron diffraction data but with local symmetry deviations, as suggested by thorough Raman measurements. The relaxor behavior in $\text{BaTi}_x\text{Zr}_{1-x}\text{O}_3$ ceramics is expected at $0.35 < x < 0.95$ with all materials being cubic at room temperature. Above $x = 0.95$, paraelectric behavior is observed [91-93]. It should be pointed out that the phase composition of the synthesized materials heavily depends on the synthesis method and the processing conditions.

In this thesis, the focus is on the SFS of $\text{BaTi}_{1-x}\text{Zr}_x\text{O}_3$, which has not been described in the existing literature on the synthesis of BTZ ceramics. In addition, in the present work an attempt was made to synthesize BTZ covering the entire Zr concentration range. A benefit provided by SFS is the generation of nanoscale powders. This is advantageous for the production of dense fine-grained ceramics with good dielectric characteristics, because the nanoscale powders demonstrate much better densification during sintering (faster powder consolidation and less porosity without significant grain growth that usually sets on at later stages of sintering) compared to particles in the micrometer range [15, 96-98].

3 Photocatalytic energy conversion and capacitive energy storage in BaTiO₃-based perovskites

This chapter is devoted to addressing photocatalytic energy conversion and capacitive energy storage using perovskite ceramic materials on the BaTiO₃ basis. The aim of this relatively large section is not to give an exhaustive review of both photocatalytic processes and capacitive energy. Rather, the focus here is on giving fundamentals and approaches to both topics, which is then applied on the material systems of choice, namely BaTiO₃ and its derivatives.

3.1 Semiconductor photocatalysis

According to the IUPAC terminology, photocatalysis is defined as “change in the rate of a chemical reaction or its initiation under the action of ultraviolet, visible, or infrared radiation in the presence of a substance – the photocatalyst – that absorbs light and is involved in the chemical transformation of the reaction partners” [99]. Photocatalytic reactions such as water disinfection [100], conversion of carbon dioxide [101], and water splitting [18, 81] have attracted much attention in view of sustainable energy technology. Water splitting especially has been the research focus for many decades, all with the aim to better understand the process and increase its efficiency.

The main emphasis of this chapter is to briefly introduce the fundamentals of photochemistry and photocatalytic processes in general with a focus on the water splitting reaction using a conventional n-type semiconductor. Basic interaction between material and light, processes occurring in the semiconductor and at its surface are considered, with a brief examination of thermodynamic aspects. Furthermore, essential material properties and requirements are discussed in connection with catalytic activity. Finally, the attention is turned to titanate ATiO₃ perovskite oxides, where their activities in water splitting are examined depending on the amount of the substituting material introduced.

3.1.1 Fundamentals of photochemistry

The main processes that occur in a photocatalytic reaction are graphically outlined in Figure 3-1a. The interaction between light and a semiconductor implies absorption of photons and a subsequent excitation of electrons from the energetically low state (ground state) to a state with higher energy (excited state) as shown schematically in Figure 3-1b. In other words, the interaction of light with the electronic structure of the semiconductor takes place, whereby an electron–hole pair forms (exciton), and the electron with sufficient energy (higher than the bandgap value) is excited into the conduction band (CB), leaving a positively charged hole in the valence band (VB) [81]. After migration of the photogenerated charge carriers to the surface, single electron or energy² transfer processes to a redox system (oxidizable and reduceable species) at the semiconductor surface may occur. Additional events such as emission of light (fluorescence and phosphorescence) and radiation-less deactivation (internal and external conversion when a molecule transits from a higher to a lower electronic state) can occur during migration and at the surface causing very short charge-carrier lifetimes on the order of ns or shorter. Electron-transfer processes are the only ones that lead to chemical reactions as discussed below [102, 103].

² Electron exchange or dipole–dipole resonant coupling. Refer to [102]

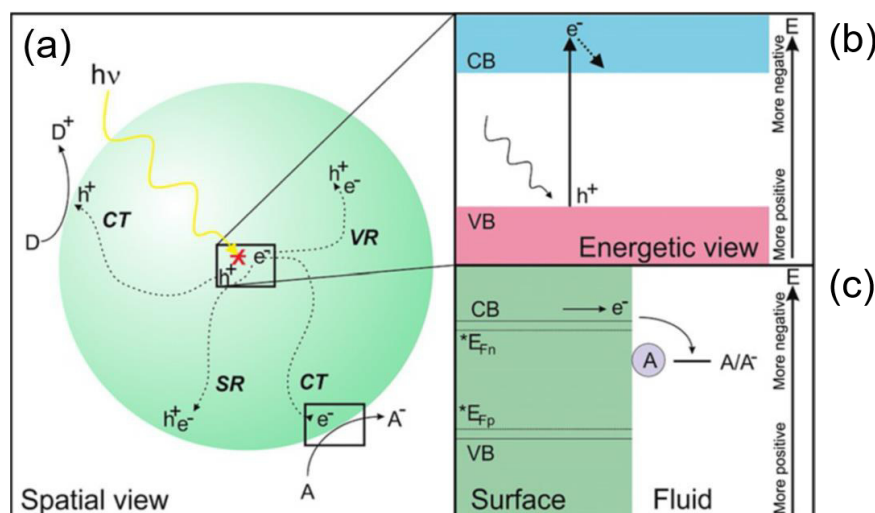


Figure 3-1. Schematics of the processes in heterogeneous photocatalysis. a): Spatial view of charge-carrier generation symbolized by h^+ and e^- upon irradiation, recombination events: volume (VR) and surface recombination (SR), charge-transfer processes (CT). b): Excitation of an electron from the valence band (VB) to the conduction band (CB) and relaxation to the bottom of the conduction band. c): Electron transfer onto an adsorbed acceptor molecule. Adapted from [104].

In order to maintain an ongoing chemical reaction, it is necessary to preserve a continuous electron transfer process from the VB of the material to the acceptor species and from the acceptor species to the hole in the CB of the materials (Figure 3-1c), which vastly depends on the average lifetime of the charge carriers involved in the process. Electron transfer proceeds via electron tunneling – a phenomenon that can occur across the solid/liquid (or solid/gas) interface enabled by the distances less than a nanometer. A competing process with the electron transfer is electron and hole recombination – a process, which decreases the number of available charge carriers for the reaction and is detrimental to the overall efficiency of the photocatalytic processes because the recombination rates lie roughly on the same timescale as the interfacial electron transfer [103]. Recombination (schematically shown in Figure 3-1a) can occur either in the volume (volume recombination) or at the surface (surface recombination), and inhibiting its rate is crucial to increasing the efficiency of the catalytic processes [102, 105].

In a model reaction where a semiconductor is in contact with a redox system, the ability to perform charge transfer depends on the existence of an electrochemical potential gradient in the system. This means that the oxidation and reduction potentials of the adsorbed species (acceptors and donors) have to be located below the CB edge potential for the acceptor species and above the VB potential for the donors, i.e., within the bandgap of the semiconductor. However, it is very often the case that higher potentials are required to drive reactions with high rates, which is called overpotential. The better the catalytic function of the catalyst, the lower is the kinetic barrier and therefore overpotential values [104]. If the established charge transfer is continuous and exergonic ($\Delta G < 0$), the process is then termed heterogeneous photocatalysis [81, 102, 105].

A very important consequence of the electron transfer for solid/liquid interfaces is that it causes redistribution of charges in the semiconductor and at its surface, which results in a phenomenon called band bending [24]. This leads to the development of a space-charge region in the semiconductor, which in turn varies the potentials of electrons and holes. The potential difference creates an internal electric field that serves as an effective charge separator, preventing electron–hole recombination and driving opposite charges in opposite directions [102]. The same principle is used in the formation of a Schottky

barrier at the metal-semiconductor interface and also exploited in the photocatalysis when doping with noble metals like Pt on TiO₂ nanoparticles for a more effective charge separation [24, 102, 105, 106].

3.1.2 Photochemical water splitting

In this section, the attention is focused on water splitting and its main aspects are discussed. Photocatalytic water splitting (or photochemical cleavage to hydrogen and oxygen) is an endergonic reaction ($\Delta G > 0$) where stoichiometric amounts of H₂ and O₂ (2:1) form from water upon interaction of light with the electronic structure of a semiconductor. The basic thermodynamic requirement for water splitting is that the standard oxidation and reduction potentials for water match the electrochemical potentials of the reactive electrons and holes, i.e., more negative than -0.42 eV and more positive than 0.81 eV according to Equation 3-1–Equation 3-3. Thus, the theoretical minimum bandgap of a semiconductor to produce one molecule of H₂O is 1.23 eV [105]. Equation 3-2 and Equation 3-3 are called half reactions of water splitting.



These thermodynamic considerations apply only at standard conditions (pH = 7) and zero reorganization energies (solvent relaxation after electron exchange) of the transfer reactions. In reality, many factors must be considered (thermodynamic losses, kinetic considerations of the charge transfer), and therefore a more realistic bandgap value ~of 2.0 eV has been proposed [105, 106]. Additionally, after closer examination of Equation 3-2, it is obvious that the oxygen evolution reaction (OER) is more complicated because four electrons are needed to generate one O₂ molecule, which is regarded as one of the main barriers to increasing overall efficiency [107]. In contrast, in the hydrogen reaction the uptake of only two electrons is required. Moreover, the kinetics of the OER are more intricate and proceed through the production of OH radicals, which requires 1.9 V reduction potential of the reacting hole, and is thus regarded as the rate-limiting step in complete water splitting [105]. Furthermore, light-induced electrons and holes are always in close proximity to each other, which favors back reactions of the reaction products to form water. These instances make water splitting a demanding reaction, and, therefore complete water splitting is rarely observed under the irradiation of an aqueous complex. For this reason, frequently only reduction or oxidation reactions (half-cell reactions) are performed to test the performance of a material [81].

One way to increase the catalytic activity of a semiconductor is to modify its surface through doping with noble metals. This is a widely applied practice, where small nanoparticles are deposited on the semiconductor surfaces to selectively improve production rates of both H₂ oxidation (Pt, Pd, Rh) and O₂ reduction reactions (IrO₂, Co_xO_y, etc.). Metal nanoparticles act as Schottky barriers that help separate opposite charges thus suppressing recombination events. Another benefit of this type of surface modification is that metal nanoparticles themselves also act as active sites for the reaction [102, 103].

Another efficient way of enhancing production rates of either hydrogen or oxygen is the use of sacrificial agents (electron or hole scavengers). Upon addition of such agents one half-reaction can be avoided so that the rate of the other half-reaction is increased [102]. For example, photocatalytic H₂ production can be improved by introducing electron donors such as methanol (CH₃OH) or other alcohols into aqueous solution, whose oxidation potential is much lower than that of water (0.02 and 1.23 eV, respectively).

The introduced alcohol is then oxidized during the reaction by positive holes to produce CO₂. The same concept can be applied to O₂ production reaction, where silver cations Ag⁺ can be employed as electron acceptors that react with the photogenerated electrons from the valence band. The disadvantage of the method is that sacrificial agents must be constantly added to maintain constant reactions [105, 108, 109].

3.1.3 Materials requirements for photocatalysts towards water splitting

The ultimate goal behind any photocatalytic reaction is to increase the yield of the forming species, in other words, the efficiency of the process. The main impediment is the occurrence of recombination and the thermodynamically favored reverse reaction yielding water. In this chapter, essential factors that are considered important for a photocatalyst are presented.

Arguably, the most critical factor is the light absorption spectrum of a photocatalyst, which is controlled by its bandgap value. A sufficient overlap between the employed radiation and the bandgap is an important prerequisite for higher quantum yield (number of molecules decomposed per photons absorbed) values and therefore efficiencies of the process. The problem is that most of the available semiconductor materials are only UV-light sensitive, which makes up as much as 10% of the total solar radiation. Shifting the absorption spectrum towards longer wavelengths (lower bandgap values) allows visible light harvesting, i.e., $\lambda > 420$ nm with the corresponding bandgap value of 2.94 eV ($BG = 1240 \text{ eV}/(\lambda/\text{nm})$). The result is that more photons (with less energy) can interact with the electronic structure of a semiconductor, therefore producing more electron-hole pairs, which then can participate in the surface reactions. Visible light absorption is commonly achieved by manipulating the band structure of a semiconductor through the introduction of dopants [105, 110]. Unfortunately, energy is lost due to thermodynamic considerations, non-radiative recombination, interfacial kinetics, and band-bending [111]. Therefore, the maximum theoretical efficiency for water splitting is only 14% for a bandgap of 2.5 eV [24]. An optimal bandgap value of 2.03 eV was suggested for an ideal material with no loss mechanisms taken into account that would theoretically lead to a solar-hydrogen efficiency of 16.8% [106].

A proper alignment of the bandgap edges in a semiconductor with respect to the reduction and oxidation potentials of water is a thermodynamic requirement that shows feasibility of performing either complete water splitting or its half reactions. This relationship is usually illustrated as band levels of various semiconductor materials versus redox potentials of water splitting, i.e., H₂ and O₂ generation as shown in Figure 3-2. It can be seen from the Figure 3-2 that most materials are suitable either only for hydrogen evolution or oxygen evolution, but not for both reactions, as it is restricted by the bandgap alignment. In this respect, perovskite materials such as SrTiO₃ have the advantage of possessing a favorably aligned but relatively large (3.2 eV) bandgap. Some uncertainty exists in the exact band edge levels of the materials largely due to surface electronic structure (dangling bonds, irregularities) and energy losses associated with the charge transfer [106]. Even if the bandgap alignment requirement is seemingly satisfied, due to thermodynamic reasons either hydrogen or oxygen evolution reaction but not both are observed at the same time, as is the case for TiO₂ (Figure 3-2).

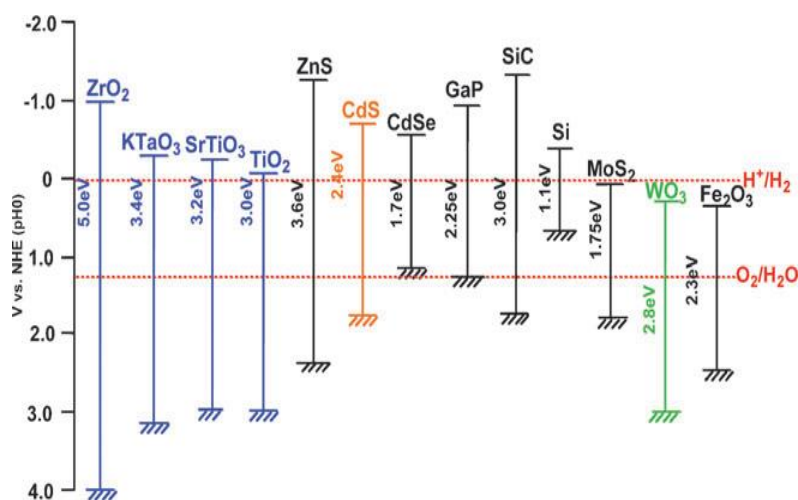


Figure 3-2. Band-edge positions of some semiconductor materials. Adapted from [81].

Another critically reviewed factor is the availability of active surface sites where photocatalytic reactions can occur mediated through the specific surface area of a semiconductor. As a consequence, nanoscale powders are preferred over their bulk counterparts due to their high surface-to-volume ratios [19]. Another benefit of having smaller particles is that the photogenerated carriers have to travel shorter distances to the reaction sites, thereby decreasing the recombination probability [24].

Operating with nanoparticles has some shortcomings as well. For instance, electrons and holes are in closer proximity to each other, which can increase the probability of recombination [81]. Moreover, the electronic structure of nanoparticles is directly influenced by the size reduction, meaning that space charge region is smaller, which leads to the decrease in the band bending potentials, and therefore less effective charge separation during the transfer process and performance degradation [24]. It is clear that compromises need to be made between having more surfaces sites and increased recombination, and no unanimous opinion exists in the current literature regarding the optimal particle size for photocatalysis, though nanoscale particles (~30–50 nm) are generally favored [82, 112]. An effective solution to the problem might be careful design of heterostructures, which combine positive sides of both material systems while diminishing charge recombination and staying at the nanoscale [23].

Crystallinity of a material affects the probability of recombination events and bulk transport. Essentially, the more crystalline the material is, the fewer defects it has, and therefore the fewer scattering and recombination events can be promoted by various structural irregularities such as grain boundaries, dislocations, and substitutional impurities [24, 81]. High crystallinity is conventionally achieved by performing high-temperature treatment, which on the other hand leads to unwanted particle coarsening and thus reduced surface availability [19, 81].

The crystal structure of a photocatalyst was also shown to be of importance for high catalytic activities, as it directly reflects the electronic structure of a material, with the best example being TiO₂ with its anatase and rutile polymorphic forms. The differences in lattice structures and overall lower symmetry of the anatase phase lead to different electronic band structure configurations (3.3 eV for the anatase phase and 3.1 eV for the rutile phase), which allows the latter to show better catalytic activity [102]. In connection with crystal structure, the particle shape has been found to play an important role, demonstrating that certain surface configurations are more reactive than others [113].

In conclusion, higher catalytic activities are achieved after a careful scrutiny of all factors and finding the right balance between them. Essentially, nanoscale and highly crystalline particles with the light

absorption spectrum extended into the visible range are preferred. This correlates directly with the production method of a photocatalyst, therefore encouraging the need to optimize catalysts and process parameters towards the photocatalytic reaction of interest.

3.1.4 Titanate-related perovskites for photocatalytic water splitting

Titanate perovskites with the general $ATiO_3$ formula like $BaTiO_3$, $SrTiO_3$, and $CaTiO_3$ are stable, non-toxic, and are wide-bandgap semiconductors suitable for photocatalytic reactions such as hydrogen production in water splitting, CO_2 reduction, and degradation of organic pollutants [19-21]. While the performance of pristine and unmodified (by doping or substitution) titanate perovskites in photocatalytic reactions sometimes cannot match that of common catalysts (Pt, Pd, Ni, Co, etc.) or the benchmark heterogeneous photocatalyst TiO_2 , they are thermally stable and resilient against photo-corrosion. The main advantage of the titanates lies in their flexibility and non-toxicity. This instance renders them promising in terms of structural modification, which allows tailoring of the properties of interest, e.g., bandgap width or introduction of defects like oxygen vacancies [17]. The range of titanate-based photocatalysts that are reasonably well studied up-to-date is rather limited and includes mostly $BaTiO_3$ and $SrTiO_3$, with the latter being examined most because of its robustness, stability, spatial reaction selectivity [114], and performance in water splitting [19]. The catalytic performance of $SrTiO_3$ can be boosted through the introduction of noble metal (Ag, Au, Pt etc.) onto the surface, as they help suppress detrimental charge recombination on the surface. Band modification is also a common technique to shift the optical absorption edge towards the visible light region, where elements like S, C, F, N, etc. are used to widen the light absorption window [19, 115]. Tan *et al.* [17] showed that preparing a non-stoichiometric $SrTiO_{3-x}$ with oxygen defects results in a better photocatalytic activity compared to stoichiometric $SrTiO_3$. A comprehensive review on the subject of the perovskite photocatalysis with a large section dedicated to $SrTiO_3$ is given by Grabowska *et al.* [18]. The author examined various synthesis methods of pure and doped/surface-modified $SrTiO_3$ nanoparticles and their photocatalytic activities, concluding that extending optical absorption window into the visible range and loading the particle surface with noble metals is an effective way of enhancing photocatalytic activity of $SrTiO_3$.

Despite $SrTiO_3$ being by far the most studied titanate perovskite system, $BaTiO_3$ is also of certain interest for photocatalysis owing to its ferroelectric properties, as discussed in Chapter 2.2. Ferroelectricity has been shown to significantly influence the surface-charge chemistry [116, 117]. For instance, Burbure *et al.* [116, 117] demonstrated that titania films grown on $BaTiO_3$ substrates can photochemically reduce Ag^+ to Ag^0 and oxidize Pb^{2+} to Pb^{4+} while exposed to UV light. The authors argued that dipolar electric fields from the ferroelectric domains cause carriers generated in the $BaTiO_3$ substrates to migrate to surfaces and participate in the respective redox reactions [116]. Later it was shown that ferroelectrics can also assist in the charge separation process in photocatalysis, and thus amend the charge recombination problem [22-24]. This concept had inspired some works in the field of photocatalysis, and proof of concept had been demonstrated by Inoue *et al.* [22, 23, 118-121]. They showed that the use of either poled single ferroelectric materials or in combination with other materials positively affects various catalytic reactions, including water splitting. Later, the effect was studied in detail for $BaTiO_3$ by Li *et al.* [23, 24], showing that inclusion of relatively large $BaTiO_3$ nanoparticles (hundreds of nm) in a core-shell heterostructure significantly enhances the H_2 production rate. Cui *et al.* [22] also demonstrated that annealed micrometer-sized $BaTiO_3$ particles modified with Ag nanoparticles show higher dye degradation rates than unmodified $BaTiO_3$ particles in the nanometer range, thereby attributing the better catalytic performance to a more prominent ferroelectric effect in particles with larger sizes.

Recently, Alammar *et al.* [19] described the use of sonochemically prepared CaTiO_3 , BaTiO_3 , and SrTiO_3 nanopowders all adopting the cubic perovskite structure for photocatalytic water splitting with a sacrificial agent. The authors compared activities of the powders after different treatment conditions (heat-treatment, doping with Rh) with a commercial TiO_2 (P25) sample. They stated that as-synthesized SrTiO_3 demonstrated a matching activity with P25, and even outperformed the latter while loaded with 0.025 wt.% Rh. Performing calcination of SrTiO_3 powders was shown to result in increased particle size and agglomeration, which negatively affected the overall performance. Some other works showed practicality of using SrTiO_3 for various photocatalytic reactions such as [17, 21, 82, 114, 122, 123].

In summary, titanate perovskites offer a consistent photocatalytic performance, which can be further enhanced by introducing dopants, surface modification or performing structural substitution. Possible utilization of the ferroelectric phenomenon inherent to tetragonal BaTiO_3 to increase the catalytic performance of H_2 production in water splitting is a particularly interesting option to explore. Considering the scarcity of works regarding BaTiO_3 nanoparticles for water splitting reaction, the main goal of the present study is the production of nanoscale and non-agglomerated powders for photocatalytic hydrogen production in water splitting. In particular, the feasibility of producing pure and substituted perovskite materials vis SFS for photocatalytic water splitting, challenges, and possible solutions are examined. A direct comparison of the photocatalytic activities between BaTiO_3 , SrTiO_3 , and Sr-substituted BaTiO_3 has never been done in the literature, which is an additional motivation for this thesis.

3.2 Capacitive energy storage

Energy storage technologies in the form of batteries and capacitors are extremely important today and are widely used in constantly growing fields of microelectronics, power grids, for electric vehicles, and renewable energy devices [7, 124]. Though batteries and capacitors are both energy storage devices, the respective approaches to energy storage and transport differ. While the main focus with batteries lies within maintaining high energy densities (10–300 Wh/kg), capacitors fall short in this respect demonstrating much lower values (30 Wh/kg) compared to batteries. On the other hand, capacitors possess high power densities (10^8 W/kg), which contrasts much lower values typical for batteries (500 W/kg) [125]. This means that batteries can store more energy but have much less energy output than capacitors (Figure 3-3a). Conversely, capacitors are capable of delivering huge amounts of electric power over a short period of time at the expense of long-term storage capabilities. Nevertheless, high energy throughput makes capacitors suitable as parts of various electronic devices such as inverters, rectifiers, and capacitive power supplies. In recent years, interest in high pulse-power applications like pulse generators (electronic flashes, electroshock generation, defibrillators) dramatically increased, where high energy densities and fast charge transfer are essential [7, 124-128].

In the following section, a correlation between important characteristics of capacitors such as the dielectric permittivity, capacitance, and energy density is established. For that, first a simple ceramic capacitor system is examined, and a theoretical background of its functioning principles is provided. In order to deliver a better understanding of the topic, the outlined concepts are later supported with some examples of specific material systems. Towards the end of the chapter, the focus is shifted towards BaTiO_3 -based systems, and strategies of improving energy storage in them are discussed.

3.2.1 Working principle of capacitors

Ceramic capacitors are passive electronic devices, where a dielectric material is placed between two conductive plates, and energy is stored on the plates in the form of electric charge [129, 130]. When an electric field is applied on a capacitor as shown in Figure 3-3b, an internal electric field develops inside the dielectric material that acts oppositely to the applied external field which is sustained by equal opposite charges Q on the surfaces of the plates. As a result, the dielectric material polarizes.

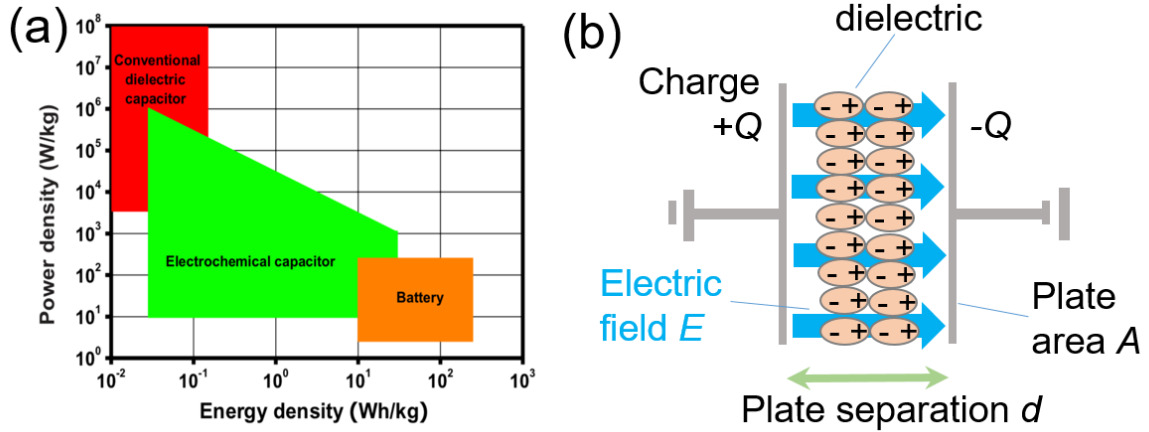


Figure 3-3. a) Power density as a function of energy density in various energy storage devices. Adapted from [125]. b) General schematics of a parallel-plate capacitor. The dielectric polarizes under the application of an electric field E .

A capacitor is said to be fully charged when the voltage between the plates is equal to the voltage supplied externally. The amount of the electric charge stored or capacitance C is described then by:

$$C = \frac{Q}{V} \quad \text{Equation 3-4}$$

where V is the voltage between the conductive plates. Changing the magnitude $E = \delta/\epsilon$ of the electric field causes a corresponding change in the surface charge density $\delta = Q/A$ and the voltage between the conductive plates according to:

$$V = Ed = \frac{Qd}{\epsilon A} \quad \text{Equation 3-5}$$

where ϵ is the permittivity of the dielectric material, A is the area of the capacitor plates, and d is the thickness of the dielectric layer. The maximum charge that the capacitor can store therefore depends on the permittivity values ϵ of the dielectric material and its dimensions. The relationship between these is described by

$$C = \frac{\epsilon A}{d} \quad \text{Equation 3-6}$$

The permittivity of a dielectric can be also expressed in a slightly different form: $\epsilon = \epsilon_r \epsilon_0$, where ϵ_r is the relative permittivity of a material and ϵ_0 is the permittivity of vacuum. As discussed above, when an electric field E is applied on a dielectric, it causes polarization of the material (Figure 3-3), which is described by the electric polarization P

$$P = \epsilon_0 \chi E \quad \text{Equation 3-7}$$

where χ is the electric susceptibility. The latter indicates the degree of polarization of a dielectric in response to an applied field and is related to the relative permittivity of the material in the following way: $\epsilon_r = 1 + \chi$. The total charge density (both free and induced by the electric field) is then described by the electric displacement D defined as

$$D = \epsilon_0 E + P \quad \text{Equation 3-8}$$

Substituting Equation 3-7 into Equation 3-8 and directly simplifying it, yields

$$D = \epsilon_0 E + \epsilon_0 \chi E = \epsilon_0 E (1 + \chi) = \epsilon_r \epsilon_0 E \quad \text{Equation 3-9}$$

The relationship between the total energy density U (in J/cm³) of the capacitor and an applied electric field E is described as an integral of the E values over displacement values

$$U = \int E dD \quad \text{Equation 3-10}$$

For dielectric materials with high ϵ values, the electric displacement D is equal to the polarization density P , and combining Equation 3-9 and Equation 3-10 results in

$$U = \int E dP = \int \epsilon_r \epsilon_0 E dE \quad \text{Equation 3-11}$$

Equation 3-11 has a defining role in the topic of capacitors, since the form of the $P - E$ curve describes the behavior of an individual energy storage system, and the energy density can be therefore directly extracted from the graph. For instance, a direct way of calculating the energy density of a system can be then represented by a linear relation after integrating Equation 3-11

$$U = \frac{1}{2} \epsilon_0 \epsilon_r E^2 \quad \text{Equation 3-12}$$

It follows from Equation 3-11 that high permittivity values of the dielectric material together with large electric fields (typically kV/cm to MV/cm range) are the prerequisites for high energy densities [7, 11, 125]. Equation 3-12 and its graphical form (Figure 3-4a) suggests that linearly increasing the strength of an applied electric field results in a corresponding linear increase of the polarization values. However, at some value of the electric field the material can sustain dielectric breakdown, i.e., it becomes conductive, and therefore ceases to be an insulator. Breakdown strength of a capacitor is thus a vital parameter that determines the stability of the capacitor at high voltages [7]. An additional inherently related characteristic to the energy storage is the energy storage efficiency η of a capacitor

$$\eta = \frac{U_{\text{rec}}}{U_{\text{tot}}} \times 100\% \quad \text{Equation 3-13}$$

where U_{rec} and U_{tot} are the recovered and the total energy density, respectively.

Another aspect that is inevitably associated with the performance of capacitors is the amount of dielectric losses, which is given by the loss tangent ($\tan \delta$). Dielectric losses are an inherent dissipation of electromagnetic energy in a dielectric associated with the dipole relaxation phenomenon when an electric field is applied. Low values of $\tan \delta$ represent good electrical resistivity of the dielectric, and therefore a capacitor with low losses, whereas large values are attributes of a lossy capacitor.

One issue that needs to be addressed is that the performance of a capacitor is a complex function of the various materials properties. To achieve good performance, mechanical stability, and miniaturization that result in high volumetric efficiencies, the dielectric material of choice must be a dense fine-grained ($<1\ \mu\text{m}$) ceramic, preferably with high polarizability (e.g., ferroelectrics) [15]. For instance, it was shown that continuously improving the ability to produce dense fine-grained ceramics has resulted in a constant increase in permittivity values for sub-100 nm grain sizes for BaTiO_3 [10, 15, 131-135]. Densities approaching the maximum theoretical values ($\geq 95\%$) for specific materials are controlled by applying various sintering techniques with carefully selected temperatures and timescales, while limiting and, ideally, inhibiting grain growth [136, 137]. Grain growth and densification are competing processes during sintering, and if one to retain the beneficial properties of nanograined ceramics, densification has to be promoted. In this regard, the main benefit of using nanoscale ceramics is that they offer a much faster and better densification than coarse-grained ceramics [96-98, 135]. However, it should be pointed out that on decreasing grain sizes below $1\ \mu\text{m}$, the measured permittivity values also decrease, which is related to changes in density and mobility of grain boundaries, and their dilution with low permittivity grain boundaries [15]. Moreover, in ferroelectrics the measured dielectric response decreases with decreasing grain sizes, which is associated with a reduced tetragonality of the unit cell, as well as decreased complexity of domain structures and their stable variants [15]. Thus, careful consideration of many factors is vital to maintaining the balance between high efficiencies and compactness of the final devices.

3.2.2 Classification of P - E curves in relation to energy storage

After having laid out theoretical foundations for capacitors with respect to energy storage, various types of the P - E dependencies are examined and how can Equation 3-11 can be applied in practice.

The simplest case is described by Equation 3-12 and graphically shown in Figure 3-4a, which applies to linear dielectrics and, to some extent, to paraelectrics with their ability to develop a more enhanced polarization when an electric field is applied. This results in larger permittivity values compared to linear dielectrics. Generally, linear dielectrics possess low permittivity values, moderate electric breakdown strength, and fairly high efficiencies. Metal oxides such as Al_2O_3 , TiO_2 , and fluor-containing polymers (e.g., PVDF) are the classic representatives of the linear dielectrics group whose typical behavior is shown in Figure 3-4a, while SrTiO_3 is a classic example of a paraelectric material. For example, in a review by Yao *et al.* [7] a TiO_2 system with ϵ values of ~ 110 at an electric field of $350\ \text{kV/cm}$ is mentioned. In contrast, Mg-modified SrTiO_3 shows higher ϵ values of ~ 300 , low dielectric losses (~ 0.001), which results in the total energy density of $1.86\ \text{J/cm}^3$ and high efficiency of 89.3% at an electric field of $\sim 362\ \text{kV/cm}$. However, despite the seeming linearity of the P - E dependence for both linear dielectrics and paraelectrics, energy losses for these systems originate from the interfacial or space charge polarization and result in lower efficiencies of the capacitors [7, 11].

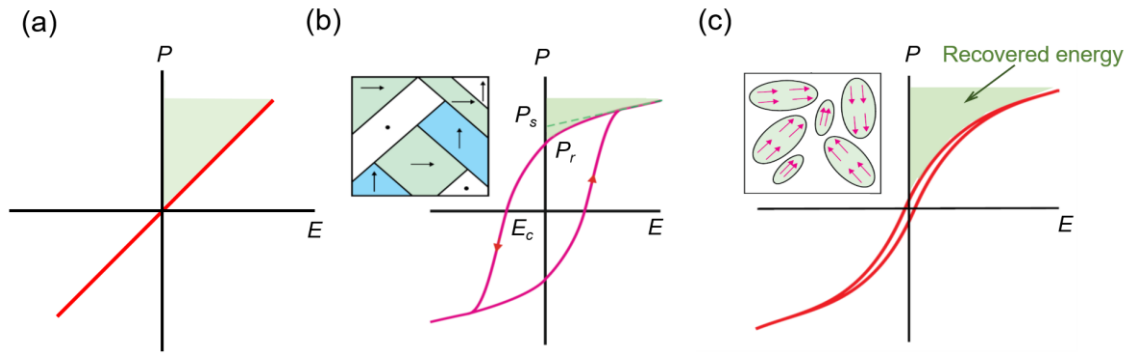


Figure 3-4. Dependence of polarization P from electric field E for (a) linear dielectrics, (b) ferroelectric materials, and (c) relaxor ferroelectrics. Additionally, ferroelectric domain (b) and relaxor microstructures (c) are schematically shown. The green colored areas show the recovered energy. Based on [8].

Accomplishing higher energy densities is inherently linked to the ability of a material to exhibit higher polarization values. This directly correlates with the ability of a material to retain polarization caused both by the creation of induced dipoles and by the relative ion displacements like in the structure of ionic crystals when an electric field is removed. The former case guarantees polarization enhancement in paraelectrics and thus higher permittivity values than in linear dielectrics, while the latter is the cause of ferroelectricity in materials [7].

The classic treatment of ferroelectric materials is that they have permanent spontaneous polarization in the absence of an electric field owing to the fact that they are made up of an array of dipoles. The dipoles form ferroelectric domains, provided that they are uniformly oriented [138]. A very distinctive characteristic of ferroelectrics is that the polarization orientation can be switched (reversed) by changing the direction of an electric field. Particularly important is the occurrence of a ferroelectric hysteresis (Figure 3-4b), which is associated with the domain size rearrangements when an electric field is applied or reversed. As the field strength increases, the polarization of the domains with unfavorable direction of polarization starts to switch along the directions that are as close as possible to the direction of the applied electric field, until at some value all domains share the same orientation. When reversing and decreasing the field, the P - E curve does not follow the same trend as before and at zero electric field the polarization value does not equal zero and shows an offset, the remanent polarization (P_r). Zero polarization can only be reached by continuing to decrease the electric field in the opposite direction. The value of the electric field at zero polarization upon reversal is called coercive field (E_c). Extrapolation of the linear segment in ferroelectric hysteresis to the electric field gives the value of the spontaneous polarization (P_s) (Figure 3-4) [8, 138].

The essential implication of the hysteresis phenomenon for energy storage is that energy needs to be spent during the domain reorientation process, and the amount of the energy invested graphically expressed is equal to the area between the upward (charge) and downward (discharge) curves (Figure 3-4b) [7]. This adversely affects the effective energy density and therefore renders ferroelectric materials with large hysteresis unfavorable for energy-storage applications despite their high permittivity values [7, 8]. Ferroelectricity is generally associated with perovskite materials like BaTiO_3 and PbTiO_3 due to the B-site cation displacements inside of the TiO_6 octahedra, which results in the polarization of the octahedra as discussed in Chapter 2.2 [8, 68, 138].

A significant enhancement in the energy density of ferroelectric systems can be achieved by retaining high polarization values while at the same time substantially minimizing hysteretic losses. The practice

so far has been to modify ferroelectric structures by substituting elements in the initial structure to create disorder and thus disrupt the ferroelectric ordering in the material towards either diffuse phase transition (DPT) or relaxor ferroelectric (RFE or relaxors) or antiferroelectric (AFE) behavior [7, 11, 139, 140].

The advantages of DPT/RFE materials is that they demonstrate lower remanent polarization values (graphically shown in Figure 3-4c), which therefore implies lower hysteretic losses, hence slimmer P - E loops [7]. The main difference between DPT, relaxors, and conventional ferroelectrics lies in the domain structure, more specifically, in the interaction between the dipoles. In a conventional ferroelectric material, a long-range ferroelectric order exists, whereas in a DPT/relaxor ferroelectric, polar nanoregions across the material have reduced long-range or only short-range interaction between them [7, 8, 92, 125]. This effect is usually accomplished by substituting a host ferroelectric perovskite material on either the A- or B-sites so that inhomogeneities arise that cause an overall compositional disorder. For instance, for ferroelectric BaTiO₃, the long-range ferroelectric order that was initially preserved by the polarized TiO₆ octahedra, is disrupted by breaking the link between the corner-sharing octahedra. The consequence is that each of these created individual polar regions behaves as an individual ferroelectric with slightly deviating characteristics (T_m) from its neighbors, leading to a smeared phase transition and less pronounced hysteresis [8]. An excellent review on the topic of relaxor materials and their theory is given by Shvartsman *et al.* [92].

The range of RFE materials includes largely well-studied lead-based systems, such as Pb(Mg_{1/3}Nb_{2/3})O₃, Pb(Zn_{1/3}Nb_{2/3})O₃, (Pb,La)(Zr,Ti)O₃ etc. [7, 8, 92, 125]. Since lead became the cause of environmental concern, it is constantly discarded from the research despite convincing dielectric characteristics of the materials. This revitalized interest in BaTiO₃-based ceramics and resulted in some encouraging results with systems like BaTiZrO₃-BaCaTiO₃ [141], BaTiO₃-BiScO₃ [7, 92], BaTiO₃-BiYbO₃ [140], and BaTiO₃-Bi(Mg,Ti)O₃ [68].

In conclusion, a combination of high polarization due to ferroelectric effect while minimizing energy losses associated with hysteresis is regarded as a key to obtaining higher energy densities and therefore leads to more efficient capacitive devices.

3.2.3 BaTiO₃-related perovskites for capacitive energy storage

Titanate perovskites, especially ferroelectric BaTiO₃ became popular as dielectric materials for ceramic capacitors owing to their excellent dielectric properties. As pointed out above, the major downside and obstacle in achieving better performance is the hysteresis phenomenon and losses associated with it. Additionally, a strong dependence of the dielectric permittivity values from temperature coupled with a phase transition from the ferroelectric tetragonal to the paraelectric cubic phase is observed around ~120°C (Figure 2-4a) [10, 131]. This results in unstable performance of the material, as both permittivity values and dielectric losses can show considerable fluctuation over a narrow temperature range. Improvement of this situation and others (hysteretic losses, phase composition, and particle size) in BaTiO₃ ceramics is traditionally accomplished by performing a wide-range substitution on either the A- or B-site of the host perovskite structure. This gives rise to certain structural rearrangements in the microstructure with the purpose of steering the properties towards improving energy storage characteristics. In this respect, dielectric materials based on the ferroelectric BaTiO₃ structure can be modified with the aim of achieving DPT or relaxor behavior. As was previously pointed out in the preceding chapter, RFEs combine high permittivity values with low energy losses, because of slimmer P - E loops (Figure 3-4c), which are exactly the requirements for high-performance capacitors [7].

One of the most prominent and extensively studied RFE systems is Zr-substituted BaTiO₃ (BTZ) [92]. Depending on the amount of Zr, BTZ can display a wide range of various ferroelectric behavior types [142]. The region of particular interest lies within the values of Zr concentration ≤ 0.30 , where conventional ferroelectricity, DPT, and relaxor phenomena occur [92]. An additional asset of the system is that it is not toxic, unlike its Pb-containing analogues.

Unfortunately, BTZ systems have been continuously neglected with respect to energy storage applications despite the potential they might hold. For instance, Sun *et al.* [13] studied the energy-storage capabilities of BaTi_{0.8}Zr_{0.2}O₃ film capacitors grown on SrTiO₃ substrates. The total layer thickness was about ~90 nm while the dielectric constant values registered were in the range between 130–190. The system was able to achieve volumetric energy storage values of 30.4 J/cm³ with 81.7% energy efficiency under an electrical field of 3.0 MV/cm. Liang *et al.* [12] investigated the BaTi_{0.65}Zr_{0.35}O₃ system with the focus on varying the thickness of film capacitors deposited on SrTiO₃ substrates. They showed that increasing the thickness of the film from 20 to 440 nm results in dielectric constants of ~200, higher breakdown voltages of 6.6 MV/cm, and higher recoverable energy densities of 78.7 J/cm³ that are comparable with lead-based systems like Pb_{0.8}Ba_{0.2}ZrO₃. Additionally, great thermal stability of the investigated BTZ systems is emphasized in both works. Instan *et al.* [14] studied BTZ films prepared by pulsed laser deposition while varying the concentration of Zr. For a film with 30% of Zr they found the best recoverable energy density around 156 J/cm³ at an electric field of ~3 MV/cm with an efficiency of 72.8%. This provides an excellent example of the energy storage capabilities of BTZ ceramics.

The use of fine BTZ nanoparticles towards energy storage in ceramic capacitors has not been explored in the literature so far. As mentioned above, fine nanoparticles deliver better densification behavior during sintering than bulk ceramics, therefore contributing to the production of dense fine-grained ceramics. The latter in turn allow for a decrease in layer thickness of a capacitor which leads to higher volumetric efficiencies, and ultimately better performance. Considering the convincing performance on the examples of various thin film BTZ systems discussed above, BTZ is an excellent candidate to test in the nanoparticle synthesis. The aim of the current study is to apply the SFS synthesis technique and examine its viability for production of BaTi_xZr_{1-x}O₃ nanopowders with various x values. The powders have to be later compacted, sintered, and, lastly, tested in regard to their dielectric performance. Powder characterization, post synthesis processing, and dielectric tests are described in detail in chapters 6.4 and 6.5.

4 Gas-phase synthesis of nanoparticles

With the material systems discussed in the preceding chapters, the question that arises next is which production method can be suitable for the synthesis of nanoparticles. This matter was briefly addressed in the introduction, where a few typical synthesis routes such as wet chemistry, solid state, and gas-phase approaches were introduced. In this chapter, the attention is focused on the gas-phase synthesis methods, specifically on the spray-flame synthesis process.

As it becomes quite evident from the name of the technique, the SFS method is based on a combustion process, where energy is supplied by the exothermic reaction of a burning pilot flame, which is typically a CH_4/O_2 mixture. It is also apparent that the final products in combustion-based processes are oxide materials. The technique is very flexible: organic precursors like metal salts or soluble metal complexes can be directly dissolved in appropriate organic solvents, which also serve as combustible fuel. One additional advantage is that the prepared solutions can be directly supplied into the reaction zone [35].

One of the essential processes associated with SFS is spray formation, whereby solutions are dispersed into a spray consisting of fine droplets. The droplets are then ignited by the pilot flame and combust. Combustion of droplets is a very complex topic, which was in detail studied by Rosebrock *et al.* [143, 144]. Essentially, the authors showed that homogeneous powders form from specific solvent/precursor mixtures that facilitate droplet disruptions via microexplosions. In brief, in droplets that consist of high melting/boiling point precursors and a solvent with a lower boiling point first evaporation of the solvent takes place through combustion of the droplet. At some point, as the solvent evaporates, the concentration of the precursor species in the outer layer of the droplet leads to a viscous shell formation that “traps” evaporating species from underneath the shell. The vapor pressure of the precursor species steadily rises until the droplet explodes. Strobel and Pratsinis [40] also showed that homogeneity of the synthesized powders can be controlled by varying solvent/precursor composition. Thus, careful consideration of solvent/solution mixtures is crucial to obtaining high-quality particles in SFS.

Ideally, homogeneous particles are produced through a gas-to-particle route, which implies complete transition of the precursor into the gas-phase, where then nucleation takes place and from that the onset of particle growth (Figure 4-1). A competing process is droplet-to-particle conversion, where a solid phase formed in the droplet through a variety of routes, e.g., precipitation, gelation, and therefore isn't a gas-phase process [33]. It should be noted though that both conversion route may occur in SFS, we'll address the gas-to-particle route, as it is supposed to be the only dominant mechanism in the flame-synthesis of homogeneous nanoparticles.

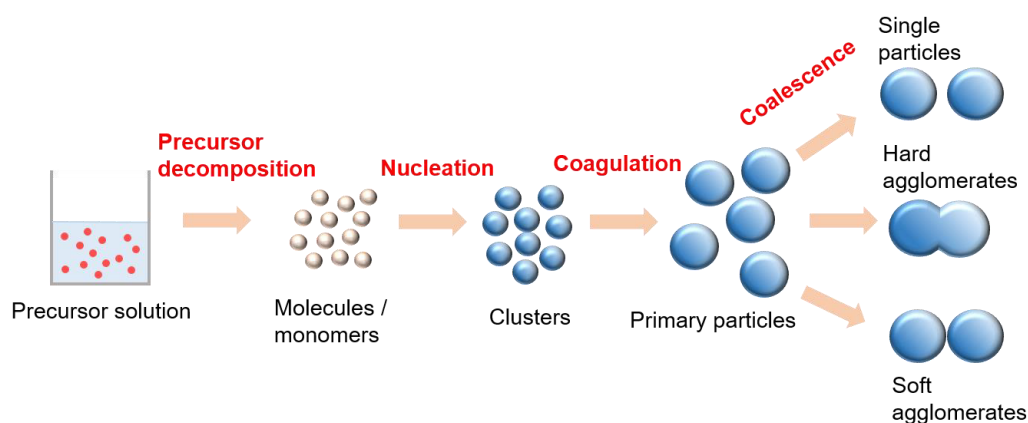


Figure 4-1. Particle formation steps in the gas-phase synthesis via an SFS process. Based on [34].

The focus of this chapter is to describe the main processes during the gas-phase synthesis of nanoparticles. The theoretical fundamentals that are given further in the text are applicable to any gas-phase method and are not restricted solely to the SFS technique. For a more profound theoretical description of the aerosol-based processes, the reader is referred to [33, 145]

4.1 Nucleation

Nucleation in the gas-phase is the process whereby gas atoms and molecules form solid or liquid particles. The process is intimately linked with the condensation of small ensembles of gas atoms, molecules, and monomers (also called clusters), and occurs only if the vapor pressure of the species in a cluster is higher than their equilibrium vapor pressure, in other words supersaturation has been reached [33, 145]. This phenomenon is described by the following expression:

$$S = p/p_s \quad \text{Equation 4-1}$$

Once $S > 1$, the system becomes unstable and is said to be supersaturated. Before the nucleation process sets on, clusters of various sizes formed by multiple collisions with other molecules or clusters exist in the gas-phase. Most of them are thermodynamically unstable with respect to evaporation and eventually break up. It is assumed that clusters have a spherical shape (similar to water droplets in the atmosphere), and the vapor pressure around a curved surface of such cluster is different from that over a flat surface. The free surface energy of the cluster will then be described by $4\pi r^2 \delta$ term, where r is the radius of the cluster and δ (J/m²) is the surface tension of the bulk material over a planar surface. Therefore, the Gibbs free energy of the whole system comprising of the vapor and the cluster is given by [145]:

$$G = n_A \mu_A + n_B \mu_B + 4\pi r^2 \delta \quad \text{Equation 4-2}$$

where n_A and n_B the number of moles in the vapor and cluster phases, respectively, and μ_A and μ_B are the corresponding chemical potentials. Since the condition for equilibrium is $\Delta G = 0$ and the mass transfer from the gas-phase to solid particles is $dn_B = -dn_A$, the first two terms result in the negative difference in the free energy between the vapor and the cluster of a critical size:

$$\Delta G = (\mu_B - \mu_A)n_B + 4\pi r^2 \delta = 0 \quad \text{Equation 4-3}$$

Knowing that for an ideal vapor [146] chemical potentials of the liquid and vapors are equal ($\mu_B = \mu_A$) and considering that the energy difference between the two components for n molecules is

$$(\mu_B - \mu_A)n_B = -n_B k_B T \ln \frac{p}{p_s} \quad \text{Equation 4-4}$$

and for a spherical cluster n can be written as follows

$$n = \frac{4\pi r^3}{3V} \quad \text{Equation 4-5}$$

Equation 4-3 can be rewritten in a similar manner:

$$\Delta G = -\frac{4\pi r^3}{3V} k_B T \ln \frac{p}{p_s} + 4\pi r^2 \delta \quad \text{Equation 4-6}$$

Taking the differential of Equation 4-6 with respect to r and performing additional transformations, one comes to the final expression, which is known as the Kelvin equation:

$$\ln \frac{p}{p_s} = \frac{2\delta V}{k_B T r} \quad \text{Equation 4-7}$$

where V is the atomic volume, k_B Boltzmann constant, T is the temperature. The Kelvin equation relates vapor pressure over a flat surface and that over a curved one. Remembering that $p/p_s = S$, one can rewrite the expression above in a similar way:

$$r^* = \frac{2\delta V}{k_B T \ln S} \quad \text{Equation 4-8}$$

where r^* corresponds to the critical diameter or size of a thermodynamically stable cluster, which can serve as a nucleation center for further particle growth through collisions with other clusters. Below this r^* value the clusters are unstable and can disperse. The implication of Equation 4-8 is that the supersaturated state is always required to activate nucleation process. It is important to mention that if the nucleation centers were generated in the vapor without the presence of a foreign body, the process is termed homogenous nucleation [33, 145, 146]. The theory has some limitations, for example, in the case of very small clusters, huge saturation values are required for a cluster to reach equilibrium with the vapor around it. Even smaller clusters a few molecules large cannot be treated as macroscopic entities, which requires surface tension and density values of a nanodimensional system. Another extreme is when the clusters are large enough (1 μm), which allows to treat them as flat surfaces [146].

4.2 Coagulation and coalescence

After nucleation occurred, further particle growth can proceed by two processes called coagulation and coalescence. The former is described as a collision of two spherical particles largely governed by the Brownian motion of these particles. As a result, the particles stick to each other to form a larger spherical particle. Coalescence is defined as particle fusion due to sintering, which strongly depends on temperature, particle size, and some material characteristics. The driving force for coalescence is the same as for sintering, namely the minimization of surface energy. Both processes always occur simultaneously but with different rates, which determines the final particle morphology [33].

In general terms, the collision frequency of two colliding particles n_i and n_j was described by the Smoluchowski equation [147]

$$N_{ij} = \beta(v_i, v_j)n_i n_j = 4\pi(D_i + D_j)(a_i + a_j) \quad \text{Equation 4-9}$$

where v_i, v_j are the particle volumes, $\beta(v_i, v_j)$ is the collision frequency function, which depends on temperature and on the radii of the colliding particles (a_i, a_j) and the diffusion coefficients (D_i, D_j), which describe the relative motion of two particles. The diffusion coefficient D is related to the properties of the particle and the medium through the Stokes-Einstein expression:

$$D = \frac{\chi^2}{2t} = \frac{k_B T}{f} \quad \text{Equation 4-10}$$

where χ^2 is the mean square displacement of the diffusing particles, f is the friction coefficient, whose exact expression depends on the form and size of the particles and how they behave in the gas medium relative to the gas mean free path. The particles are said to be in the free molecular regime if their sizes

are much lower than the mean free path ($d_p \ll \lambda, Kn \gg 1$), where $Kn = 2\lambda/d_p$. In the continuum regime, the particle is larger than the gas mean free path ($d_p \gg \lambda, Kn \ll 1$). Both regimes are used to describe particle transport through the medium and effectively describe particle growth at different times, which allows comparison with other important times like process residence time [33].

In an idealized situation and for spherical particles, in the continuum regime ($Kn \ll 1$) coagulation can be described using [145]

$$\beta(v_i, v_j) = \frac{2k_B T}{3\mu} \left(\frac{1}{v_i^{1/3}} + \frac{1}{v_j^{1/3}} \right) \left(\frac{1}{v_i^{1/3}} + \frac{1}{v_j^{1/3}} \right) \quad \text{Equation 4-11}$$

where v_i and v_j are the particle volumes, k_B is Boltzmann constant and μ is the gas viscosity. A similar expression is also available for the free-molecule regime ($Kn \gg 1$), when the molecules are much smaller than the gas mean free path and collide in a ballistic (elastic) manner:

$$\beta(v_i, v_j) = \left(\frac{3}{4\pi} \right)^{1/6} \left(\frac{6k_B T}{\rho_p} \right)^{1/2} \left(\frac{1}{v_i} + \frac{1}{v_j} \right)^{1/2} (v_i^{1/3} + v_j^{1/3})^2 \quad \text{Equation 4-12}$$

where ρ_p is the particle density. Using both expressions and applying the definition of the fractal dimension D_f to describe morphology of the agglomerate that formed (e.g., $D_f \rightarrow 3$ for spheres and $D_f \rightarrow 1$ for a chain-like structure), one can study particle agglomeration in both regimes [148]. For instance, Matsoukas and Friedlander studied the effect of the primary particle size on agglomerate growth [149]. They showed that the smaller the primary particle size the more rapid is the agglomerate growth. They also observed that the observed effect is much more pronounced in the free molecular regime, since agglomerates collide faster than the spheres of the same volume and is a strong function of D_f . In most industrial processes, however, an interpolation formula is used, which takes into account agglomeration in the transition from the free molecule regime to the continuum mode ($Kn \approx 1$) [33, 145].

After collision, two particles may rapidly coalesce to form a larger spherical particle. The opposite case is when the rate of coalescence is slow with respect to that of coagulation, which results in agglomerated particles. A ratio between the characteristic sintering τ_f and collision τ_c times is thus used to describe the resulting final particle morphology. If the characteristic time for collisions is much longer than the characteristic time for sintering ($\tau_c \gg \tau_f$), then the particles instantaneously fuse together and have spherical shape before the next collision occurs. A completely opposite case occurs when $\tau_c \ll \tau_f$. If the value of τ_f is much larger than τ_c , then growth is said to be sintering-limited, and so-called soft agglomerates are said to form, which are held together by the van der Waals forces. When $\tau_c \sim \tau_f$, hard agglomerates or aggregates form, since the temperature is no longer high enough to guarantee complete sintering, and therefore partially sintered particles are formed [33, 36, 145, 148, 150]. These cases are graphically visualized in the right portion of Figure 4-1.

4.3 Spray-flame reactor

The reactor system used in this work is an in-house designed spray-flame synthesis setup, which in detail is described by Hardt *et al.* [151], where the authors demonstrated production of small Fe_2O_3 and TiO_2 nanoparticles with various process conditions.

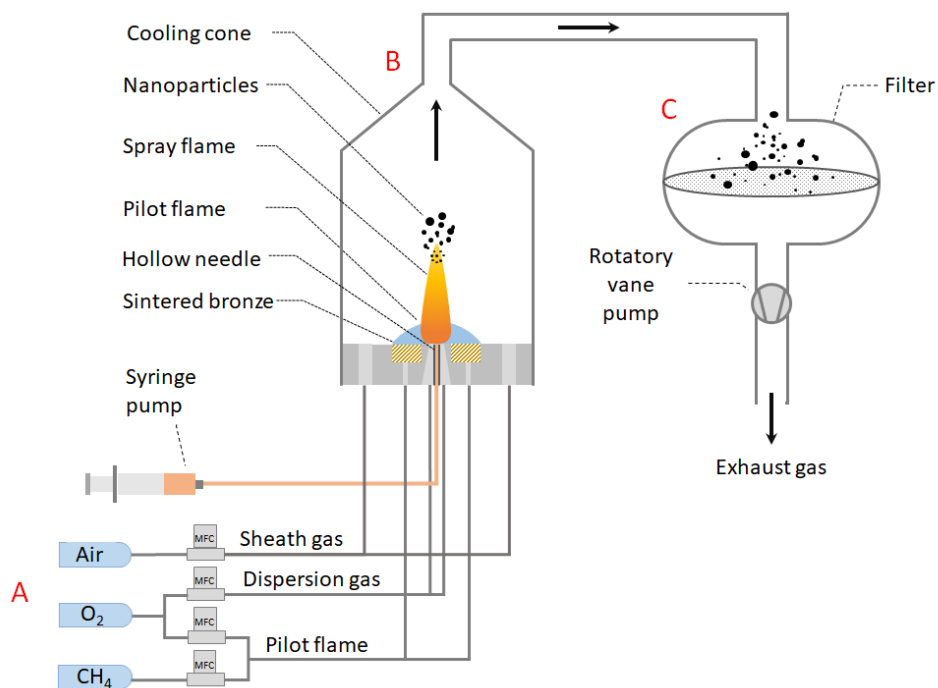


Figure 4-2. Schematics of the spray-flame reactor. (A) gas and liquid supply; (B) burner and reaction zone; (C) powder collection system [152].

The setup can be separated into three main sections as illustrated in Figure 4-2: (A) gas and liquid supply, (B) spray burner and reaction zone, and (C) powder collection system. The gas flow is adjusted by mass flow controllers (MFC, Bronkhorst, Netherlands) while the solution containing the precursor is supplied by means of a syringe pump (Nemesys, Germany). The liquid is fed through a hollow needle mounted in the middle of a two-fluid nozzle, which enables atomization of the precursor solution with oxygen (Air Liquide, 99.95%). The spray is ignited by a premixed pilot flame (CH₄/O₂ ratio of 1:2) on a porous sintered bronze support and surrounded by a coaxial sheath gas flow (air) for stabilization. Particles produced during the synthesis are subsequently transported through the cooling cone and sampled on a round sheet of a filter material (R+B Filter, Germany). A rotatory vane pump is used to control the pressure inside the reactor that enables to run the reactor at pressures between 250 and 1200 mbar [153].

5 Characterization methods

This section provides a brief outline of the experimental techniques that were used to characterize the produced nanoparticle powders.

5.1 X-ray diffraction (XRD)

X-ray diffraction is one of the most established analysis techniques that allows examination of structure on atomic scale. X-rays are electromagnetic radiation with the wavelengths ranging from 0.01 to 10 nm and energies from 100 eV to 100 keV, which puts them between γ -rays and UV radiation. The short wavelengths of X-rays are similar to the spacing of atomic planes in crystals. Therefore, X-rays are able to “probe” the crystal structure and obtain information on the atomic positions and help distinguish between different crystal structures. A crystal structure is formed when the atoms in a material are periodically arranged in space, and the smallest repeating unit of the crystal structure is called a unit cell. The periodic arrangement of unit cells extends over large distances forming a long-range order. Non-crystalline or amorphous materials have no regular periodicity of their crystalline counterparts and are said to have only a short-range order.

Like all electromagnetic waves, X-rays are characterized by a locally oscillating electric field, which exerts a force on any charged particle such as an electron in an atom, which will leave the electron oscillate about its mean position. The oscillation means that the electron will continuously accelerate or decelerate thereby emitting an X-ray photon during its, and therefore the electron is said to “scatter” X-rays. If the scattered beam is characterized by the same wavelength and frequency as the incident X-ray beam, the scattering event is then described as elastic. The scattered waves from various crystal planes interfere with each other and if the waves are in- or out-of-phase, two different types of interference can occur. If the waves are in-phase, constructive interference takes place, whereas when the waves are out-of-phase, destructive interference occurs. Ultimately, the former leads to the superposition of the scattered waves and therefore diffraction in specific directions (schematically shown in Figure 5-1), whereas in the latter case, the waves cancel each other out and no diffraction occurs.

If an atomic arrangement of repeating unit cells is considered with d being the distance between the diffracting planes within one family of planes, diffraction will occur for constructive interference at specific angles which are determined by the Bragg law

$$2d \sin\theta = n\lambda, \quad \text{Equation 5-1}$$

where θ is the incident angle, n is any integral number describing the order of the reflection (e.g., $n = 1, 2, 3, \dots$), and λ is the wavelength of the incident X-ray beam. The important implication of Bragg law is that diffraction occurs only at specific angles (Bragg angles) and depends on the arrangement of atoms within the unit cell. From the observed reflections d -spacings can be determined using Equation 5-1, which hold information about the corresponding crystal planes, which are described by the Miller indices (Each crystal structure has a unique set of diffracting hkl planes, which therefore allows phase determination of the examined materials according to the appearing peaks in a diffraction pattern [154].

In reality, diffraction occurs not only at the exact Bragg angle, but also at angles that are slightly smaller or larger than 2θ , which leads to the appearance of peaks and not just straight lines. Another important consequence is that intensity and broadening of the observed peaks depend on the number of repeating unit cells a material is made up of, i.e., crystal or crystallite size. In the course of the present work, only

nanocrystalline powders are examined, where each particle is ideally a small crystal with a random orientation with respect to the incident beam. This means that every set of lattice planes will produce a diffraction pattern unlike a single crystal, where diffraction from only specifically aligned orientations can be obtained [154].

Analysis of the acquired diffraction patterns can be conveniently done by performing Rietveld refinement. The main idea of the method is that a diffraction pattern is calculated that matches as closely as possible the measured one. From there it is possible to obtain information on unit cell dimensions, crystallite sizes, and additionally extract weighted fractions of the phases present if a multi-phase material is under investigation. The mathematic part of the refinement is governed by the least-squares method whereby the best solution or fit minimizes the sum of the squared residuals, i.e., the difference between the observed and calculated diffraction patterns.

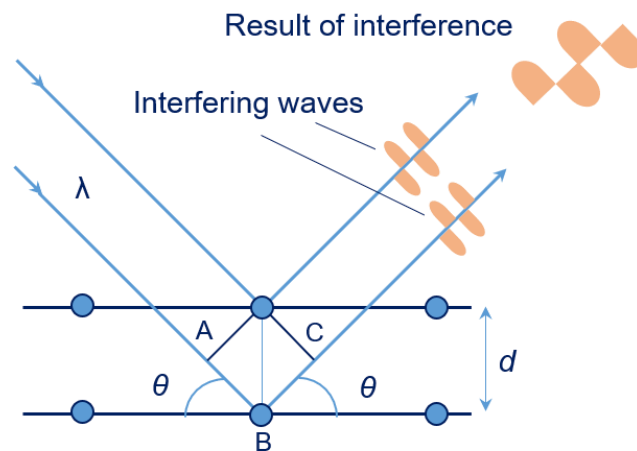


Figure 5-1. Bragg diffraction from a set of planes in the case of constructive interference.

For calculating the crystallite size of a phase, the Scherrer equation is used:

$$d_{\text{XRD}} = \frac{K \lambda}{B \cos \theta} \quad \text{Equation 5-2}$$

where K is the Scherrer constant and depends on the shape of the crystallites (typically 0.9 is taken for spherical crystallites), λ is the wavelength of the incident monochromatic X-ray beam, B is the full width at the half maximum (FWHM) of a diffraction peak, and θ is the Bragg angle. The most significant value in the equation is the FWHM B value, which should be determined properly to guarantee correctness of the calculated crystal size. In a typical refinement program, the peak shape is represented by a convolution of a Lorentzian and a Gaussian function, which is used to fit the observed peaks from where B is determined. Additionally, the instrument contribution must be subtracted from the observed B_{sample} value, such that $B_{\text{total}} = B_{\text{sample}} + B_{\text{instrument}}$. The instrumental broadening can be determined by measuring a Si or LaB₆ standard [155].

In the present work, X-ray diffractometers from PANalytical X'pert Pro and Empyrean with a Cu anode were used with a wavelength of $\lambda = 1.5405 \text{ \AA}$. The acquired patterns were analyzed using the GSAS-II software to extract crystallite sizes and phase ratios [154, 156, 157].

5.2 Transmission electron microscopy (TEM)

Transmission electron microscopy (TEM) is an extensively used imaging technique that allows examination of particle sizes, crystal structure, defects and more owing to its extremely high resolution of about 0.2 nm. Modern TEMs include many operating modes like conventional imaging, scanning TEM (STEM), selected area electron diffraction (SAED), various spectroscopic modes (EELS, EDX), etc.

The resolution of a TEM is determined primarily by the nature of electrons according to the Abbe equation

$$d = \frac{0.61 \lambda}{n \sin \alpha}, \quad \text{Equation 5-3}$$

where λ is the wavelength of the electron wave, n is the refractive index of the medium, and α is the aperture angle. It follows that the smaller λ , the better the resolution d . The relation between λ of the particle and its velocity v is introduced by the de Broglie relation:

$$\lambda = \frac{h}{m v} \quad \text{Equation 5-4}$$

where m is the mass of the particle and h is the Planck constant. Equation 5-4 implies that shorter wavelengths require high particle velocities and therefore high kinetic energies, which is attainable if one uses electrons instead of light. The relation between the wavelength and the acceleration voltage of electrons is provided by

$$\lambda = \frac{h}{\sqrt{2m U e}}, \quad \text{Equation 5-5}$$

where U is the acceleration voltage, and e is the charge of an electron. It is evident that high voltages are needed to guarantee small λ values, therefore TEMs are typically operated at 100–200 kV or even higher. As electrons are used for imaging in TEM, they are manipulated by applying electromagnetic field to create a convex lens that resembles that in a light microscope to focus the electron beam. An operation in ultra-high vacuum is required to prevent electron losses.

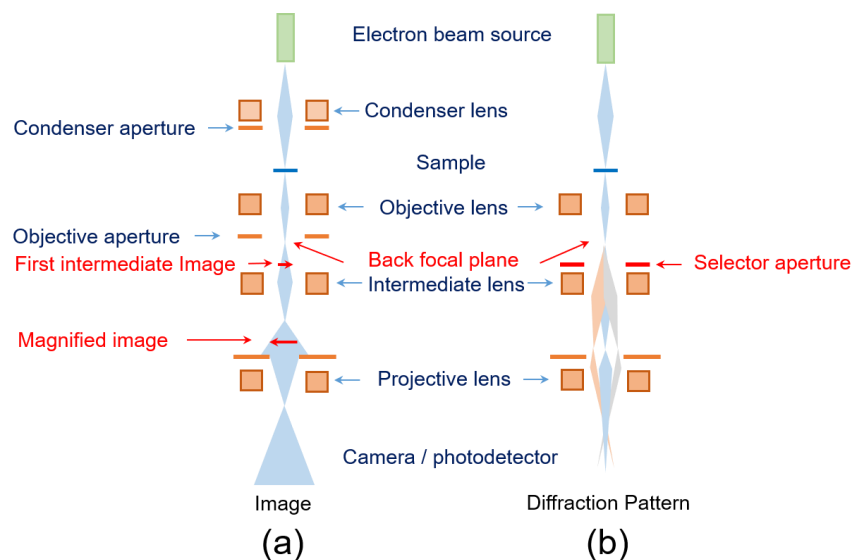


Figure 5-2. Schematics of TEM components showing formation of (a) bright field image and (b) diffraction pattern. Based on [158].

Another important constituent of a TEM is the lense system, which manipulates the electron beam and is usually comprised of condenser, objective, and intermediate/projector lenses. The primary objective of the condenser lens is to focus the electron beam onto the sample to obtain sufficient intensity. The electron beam then impinges on the sample and the latter which must be thin enough (under 0.1μ) to let at least some of the electrons pass through it. The electron beam undergoes elastic or inelastic interaction with the sample resulting in different contrasts.

After the beam has passed through the sample it is then focused by the objective lens and forms the first bright field intermediate image behind the objective aperture with a magnification of 20–50 times (Figure 5-2a). In diffraction mode, the objective aperture is removed, and the interfering waves are focused at the back focal plane behind the objective lens (Figure 5-2b). Selector aperture can be then introduced to define the region of the obtained diffraction pattern. Further magnification of the first image is adjusted by changing the operating coil current of the lens. The projector lenses situated further down the beam path are used to guide the beam onto the imaging device, which can be a photo plate or a phosphor screen coupled with a CCD (charged coupled device) camera. Figure 5-2 shows the layout of the components and outlines the working principle of a TEM. In the present work, a TEM microscope JEOL 2200FS was used to acquire high magnification images and electron diffraction patterns [158]. The TEM samples were prepared from small amounts of powder dispersed and sonicated in ethanol. A droplet of a slightly turbid solution was deposited on a lacey carbon copper grid and dried.

5.3 Raman spectroscopy

Raman spectroscopy is a very important and widespread spectroscopy technique for analyzing vibrational modes of molecules and condensed matter based on scattering of light by a substance, whereby electromagnetic radiation interacts with the electron cloud in a molecule to induce a dipole moment. At the same time, two different types of photon scattering events can occur: Rayleigh and Raman. The former one describes elastic scattering, whereas the latter is inelastic, which means that some energy is lost or gained in the process relative to the energy of the incoming radiation, with the Rayleigh scattering being the dominant process with a much larger scattering cross-section. A high-power monochromatic light source such as laser is used for analysis to provide good spectral resolution and sufficient signal from the rather inefficient scattering process.

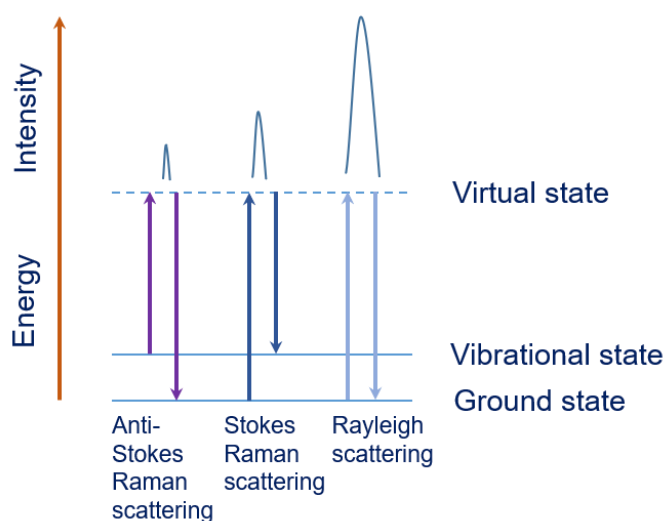


Figure 5-3. Schematics of Rayleigh scattering and Stokes and anti-Stokes Raman scattering.

Both processes are two-photon processes meaning that upon the initial interaction of the incident photons with the electron cloud of a molecule or a crystal, the electrons oscillate (often described as a “virtual state”) and almost immediately release a new photon. In Rayleigh scattering, the emitted photon carries the same energy as the incoming one. Raman scattering is much less probable than Rayleigh scattering and thus generates signal with a much lower intensity. During the scattering, an interaction with the vibrational/rotational energies (in molecules) or phonons (in the solid state) occurs and the scattered signal thus carries information about the local material. There are two types of Raman scattering exist: Stokes and anti-Stokes. In the first case, energy is lost during the scattering process, in the second case, energy is gained, for example from thermally-excited lattice vibrations. All the processes described in the preceding paragraph are schematically shown in Figure 5-3.

The intensity of Raman scattering is expressed by

$$I \propto \nu^4 I_0 N \left(\frac{\partial \alpha}{\partial Q} \right)^2, \quad \text{Equation 5-6}$$

where I_0 is the incident laser intensity, N is the number of scattering molecules in a given state, ν is the frequency of the exciting laser, α is the polarizability of the molecules, and Q is the vibrational amplitude. The use of the Equation 5-6 has some important implications for Raman analysis. The most important is that only molecular vibrations which cause change in polarizability are Raman active. This is addressed by

$$\left(\frac{\partial \alpha}{\partial Q} \right) \neq 0. \quad \text{Equation 5-7}$$

In solid crystalline materials, the incident laser beam causes polarization of the dipoles by interacting with the phonons of the crystal lattice. The polarization of the dipoles depends on the polarizability tensor α^*

$$P = \sum \alpha^* E. \quad \text{Equation 5-8}$$

This expression can predict both elastic and inelastic scattering and the latter occurs only if the vibrations (or rotations in molecules) change the (non-zero) polarizability of the molecule. The condition expressed by Equation 5-8 is dictated by the symmetry of the molecules/crystals, therefore, Raman activity can be predicted by applying group theory [159, 160].

Measurements in the present work were carried out on a RENISHAW Invia 0113-20 Raman microscope using a 532 nm laser with 1800 grooves/mm grating and an $\times 20$ objective.

5.4 Fourier transform infrared spectroscopy (FTIR)

Infrared spectroscopy is an important tool that allows examination of surfaces to study their coverage with organic groups. As the name already suggests, IR portion of the electromagnetic spectrum is used to illuminate the sample, whereupon the alternating electric field of the IR light interacts with the electrons of a molecule and causes the molecule to displace (vibrate or rotate) when the resonance condition is provided. The resonance condition means that the frequency of the incident IR radiation matches the natural frequency of a particular vibration/rotation mode of the molecule and the radiation is then said to be absorbed. The absorption process therefore raises the energy of the molecule from its initial state to a higher specific quantized excited state. More importantly, in order for an IR photon to be

absorbed, its energy must be transferred to the molecule causing a change in the dipole moment of the molecule. This is a so-called selection rule for IR spectroscopy, which is frequently expressed in the following form:

$$\mu = \sum e_i r_i, \quad \text{Equation 5-9}$$

where μ is the dipole moment, e_i are the atomic charges, and r_i are the atomic positions. Motion of a diatomic molecule is usually depicted using the harmonic oscillator model where atoms are connected by a spring, and the vibration frequency depends on the mass of the atoms and the bond energy between them. A change in the dipole moment relates to the symmetry of the molecule or the charge distribution in it. For instance, symmetric homonuclear molecules like O_2 or N_2 exhibit no dipole moments and therefore are said to be IR-inactive, whereas heteronuclear molecules like CO have dipole moments and are IR-active. Important to stress is that for IR-inactive molecules no absorption occurs. Group theory can be applied to IR spectroscopy to predict the frequencies of the expected bands.

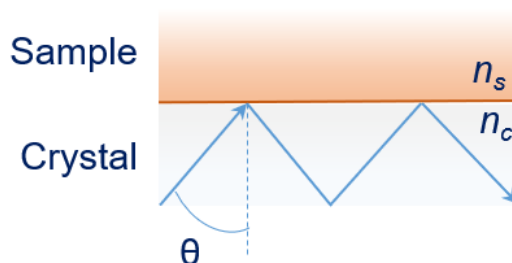


Figure 5-4. ATR-FTIR principle at the interface schematically depicted.

In IR spectroscopy, it is typically differentiated between transmission and reflectance measurement methods. For transmission methods of powder or thoroughly ground samples, pellets are typically pressed using KBr as a non-absorbing matrix. Though when correctly prepared the pellets deliver good quality spectra with no absorption bands from KBr, it is hygroscopic which might result in the presence of unwanted water bands and therefore requires careful handling. Reflection techniques specifically attenuated total reflectance IR spectroscopy (ATR- IR) have become popular due to easiness in handling and absence of any sample preparation. ATR-IR is a contact method where non-transmitting and are in contact with an ATR crystal, the latter having a refractive index n_c much higher than that of the sample (n_s) to allow for internal reflections at moderate angles of incidence. The incident angle must be greater than the critical angle θ so that total internal reflection back into the crystal occurs at the interface:

$$\sin \theta = \frac{n_s}{n_c} \quad \text{Equation 5-10}$$

where n_s is the refractive index of the ATR crystal and n_r is the refractive index of the sample. During reflection, the incident IR beam partially passes through the crystal surface and the reflected radiation penetrates for a short distance into the sample in the form of an evanescent wave. The effective penetration depth is described by

$$d_p = \frac{\lambda}{2\pi n_c \sqrt{\sin^2 \theta - (n_s/n_c)^2}}, \quad \text{Equation 5-11}$$

where λ is the wavelength of the IR radiation. Typically, the penetration depth is in the range of 0.5–2 μm . The reflected light is then partially absorbed through resonant interaction of the evanescent wave with the material (e.g., a powder sample) positioned on top of the ATR crystal. Commercial IR spectrometers can be equipped with a wide variety of ATR crystal materials (diamond, Ge, Si) and make use of an interferometer to generate an interferogram that is later converted to an IR spectrum of the sample by applying a Fourier transformation, and for this reason are called FTIR spectrometers. After a spectrum is recorded, band assignment can be carried out based on the spectral features or “fingerprints” of the individual organic groups [159, 161, 162]. For surface analysis in the present work, attenuated total reflectance infrared spectroscopy measurements (ATR-FTIR) were measured using a Bruker Vertex 80 spectrometer in the 400–4000 cm^{-1} wavelength range with a resolution of 4 cm^{-1} .

5.5 Specific surface area measurements (BET)

Gas-adsorption methods allow for examination of the sample’s specific surface area and porosity. The former can yield information on the particle size values if morphology and density of the sample are known. The most common approach is the use of the BET (Brunauer-Emmet-Teller) multilayer adsorption theory, which is in essence an extension of the monolayer adsorption theory introduced by Langmuir. The pinnacle of the BET theory is that it enables the determination of the number of physically adsorbed molecules required to cover exactly one monolayer even though that monolayer is never actually formed. In this case, an uneven random distribution of sites covered by a different number of molecules is said to occur, and gas molecules infinitely adsorb on a solid surface. Important assumptions of the theory are that all layers after the first one have the same adsorption and desorption constants and the same energy of adsorption E . Additionally, E is independent of the surface coverage θ , which therefore implies a homogeneous surface of the solid. For a monolayer adsorption, the coverage is described

$$\theta_1 = \frac{N}{N_m} = \frac{W}{W_m} \quad \text{Equation 5-12}$$

where N and N_m are the number of molecules, W and W_m is the weight adsorbed in the incomplete and complete monolayer, respectively. Assuming that the number of the adsorbed layers is infinite, the surface coverage for the n^{th} layer is then

$$\frac{\theta_n}{\theta_{n-1}} = 1 \quad \text{Equation 5-13}$$

which physically means that the adsorbate condenses on the surface or $p/p_0 = 1$, where p is the adsorbate pressure and p_0 is the saturation pressure of the bulk fluid. One arrives then at the final expression known as the BET equation

$$\frac{1}{W(1 - p/p_0)} = \frac{1}{W_m} + \frac{C - 1}{W_m C} (p/p_0), \quad \text{Equation 5-14}$$

where C is the BET constant and is related to the heat of adsorption. Generally, it is accepted that values of $C > 2$ give a generic curve of the Type 2 isotherm, whereas higher values (~ 100) deviate from that and therefore signify a different adsorption behavior.

For further evaluation of the surface area, a typical BET plot must be constructed, whereby $1/W(1 - p/p_0)$ values are plotted versus different p/p_0 values. Therefore, Equation 5-14 is linear with

slope $s = \frac{C-1}{W_m C}$ and intercept $i = \frac{1}{W_m C}$ to obtain W_m and C values. To guarantee the linearity of the BET plot, the experiments must be carried out in a specifically determined pressure range, which is typically $p/p_0 \approx 0.05-0.3$, but not exclusively and depends on the material system. After W_m was determined, the total surface area can be calculated from

$$S = \frac{W_m N_A A}{M}, \quad \text{Equation 5-15}$$

where W_m is in grams, M is the adsorbate molecular weight, N_A is the Avogadro number, and A is the cross-sectional area of the adsorbate gas, nitrogen in most cases. The specific surface area (SSA) δ is the S value divided by the weight of the sample. The SSA can be further converted to the average particle size assuming a spherical particle shape using the following expression:

$$d_p = \frac{6000}{\rho \delta} \quad \text{Equation 5-16}$$

where d_p is the particle size in nm, ρ is the density of the sample. The BET theory is very convenient in everyday analysis, but some assumptions taken do not correspond to the situation occurring in real systems. For instance, the energetically homogeneous surface is not provided in all cases and the absence of the influence between the lateral interactions of the adsorbate molecules is not considered. The last point is the significance of the C parameter, which though helps in characterizing the shape of an isotherm, should be nevertheless approached with care as the E values cannot be extracted with 100% credibility [163, 164]. In the present work, a Quantachrome NovaWin 2200 instrument was used to perform BET measurements. All samples were degassed at 200°C overnight prior to analysis.

5.6 Thermogravimetric analysis (TGA)

Thermogravimetric analysis (TGA) allows tracking the mass change of a sample as it is subjected to heating at a constant rate. Thermal events such as decomposition, oxidation, phase transition etc. that occur during the heating can therefore be assigned based on the observed mass changes. A complementary technique that is routinely employed alongside TGA is differential scanning calorimetry (DSC) in which the difference in the amount of heat flow rate to the sample and to a reference sample is analyzed. As the sample of interest displays endothermic or exothermic features, more or less heat flows to the sample than to the reference material to maintain both at the same temperature, and temperature difference is recorded as a direct measure of the difference in the heat flow rates. Important is that the reference sample should have well defined heat capacity and demonstrate no changes over the measured temperature range. Additionally, spectroscopic techniques can be applied to analyze the evolving gaseous species. For instance, quadrupole mass spectrometry (QMS) is frequently used to scan a range of various mass-to-charge (m/z) ratios. The detected ions can be then assigned based on their m/z values.

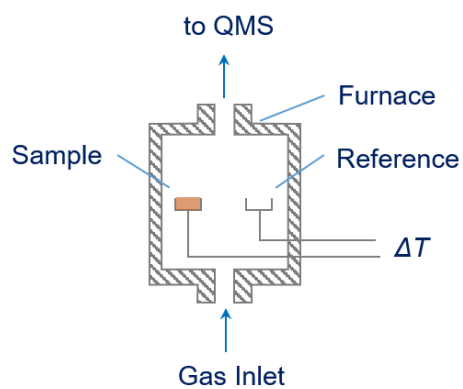


Figure 5-5. Schematics of a TGA/DSC apparatus.

TGA measurements can be performed in various atmospheres, e.g., in N_2 if inert atmosphere is desired. Powdered samples are typically pelletized to guarantee consistent DSC signals. In the present work, the measurements were performed on a STA-449 Jupiter from NETZSCH with a built-in QMS [165].

6 Experimental results

As discussed in Chapters 1 and 2, BaTiO₃ is a technologically important material whose synthesis via the SFS technique has been scarcely covered in the available literature. This fact makes the subject of investigating the applicability of the SFS towards consistent production of high-quality BaTiO₃ an attractive research task. In addition to pure BaTiO₃, a derivative titanate system such as (Ba,Sr)TiO₃ is of certain scientific interest since it can be potentially used as a catalyst in photocatalytic energy conversion such as hydrogen production in water splitting, where the nanoscale size range of the produced powders by SFS should be of benefit for attaining higher production rates due to their high surface areas. On the other hand, Ba(Ti,Zr)O₃ is another system that is a promising candidate for energy storage applications owing to its good dielectric characteristics and non-toxic nature, which could lead to a potential replacement of PbTiO₃-based capacitors, where nanoscale of the produced powders would allow for higher volumetric efficiencies of the final capacitors. Thus, the focus of this chapter is to explore the feasibility of the SFS technique for the production of BaTiO₃, Ba_xSr_{1-x}TiO₃, and BaTi_{1-x}Zr_xO₃ (further referred to as BTO, BSTO, and BTZ, respectively) perovskites. In order to perform a comprehensive study that correlates physiochemical properties of the produced materials with their performance in the respective applications, the following strategy was used: a preliminary study was first conducted for pure BTO powders to define synthesis and process parameters that guarantee a stable production of high-quality nanoparticles. The defined parameters were then transferred on the synthesis of other perovskite systems, namely BSTO and BTZ. At the same time, great emphasis is put on powder characterization that helps correlate physiochemical properties of the materials based on the chosen synthesis and process parameters. Thus, both synthesis and powder characterization are the focal points of the present work.

6.1 Synthesis of BaTiO₃ nanoparticles

6.1.1 Investigation of process parameters, solvents, and precursors.

One of the main difficulties in the SFS of BaTiO₃ and perovskite materials in general is the scarcity of information that describes the choice of synthesis conditions, precursors, and solvents. The main reason for that is that titanate perovskites are conventionally produced via solid state or wet chemistry methods [25, 29, 166, 167]. Therefore, one of the primary objectives of the present study is to survey precursor, solvent, and process parameter configurations (e.g., pressure in the reactor, gas and liquid flows). All of those are known to greatly affect properties of the final powders and therefore the right combination helps in obtaining high-quality powders [40, 153, 168]. In this study, for the term “high-quality” the following aspects were considered: (i) particles have to be in the nanometer range; (ii) preferably single-phase materials with the main phases being perovskite phases and no undesired secondary phases; (iii) limited amount of carbon contaminations that are typically present in the powders after combustion processes in the form of carbonates (e.g., BaCO₃) or other carbonaceous species, which is a common issue for almost all established synthesis methods of BaTiO₃. The presence of carbonate impurities negatively affects performance of the powders and should be minimized, and if possible, avoided at all.

First, prior to synthesis, an evaluation of the metal precursors and solvents on the market was done considering following points: (i) their availability; (ii) compatibility (solubility, melting/boiling points); (iii) cost. A list of typically used barium precursors includes barium nitrate (“BN”, Ba(NO₃)₂), barium carbonate (“BC”, BaCO₃), and barium acetate (“BA”, Ba(CH₃COOH)₂). BC was discarded from further consideration as it is soluble only in highly acidic environments (e.g., addition of HCl) and insoluble in

alcohols and water [169]. Moreover, in the reaction between BC and acetic acid, BA is produced, whereby CO₂ and water are released, which leads to the formation of large particles by precipitation [40, 143]. BN is an accessible and inexpensive barium precursor with extremely low solubility in water and complete insolubility in alcohol, and therefore is not suitable for SFS. BA on the other hand, is widely available and offers good solubility in water and carboxylic acids but is more expensive than BN and BC. It is important to mention that acetates are known to decompose to the undesired MeCO₃ by-products on heating, as is typically the case in solid state and sol-gel synthesis approaches [28, 170]. On the other hand, the use of metal acetate precursors in an SFS process was shown to result in small and homogeneous nanoparticles [51].

Titanium can be introduced into the synthesis in the form of titanium isopropoxide (TTIP, C₁₂H₂₈O₄Ti) and titanium tetrachloride (TiCl₄). The latter is corrosive and toxic, which is also prone to hydrolysis, and therefore was discarded. TTIP is the standard chemical for the flame synthesis of TiO₂ that is less toxic, but is also prone to hydrolysis, which could potentially lead to unwanted formation of TiO₂ during the SFS of BaTiO₃. TTIP and is also more expensive than TiCl₄[171], but an advantage of using TTIP is that it is miscible with alcohols [168, 172].

The choice of solvents was also carefully considered. Carboxylic acids and alcohols were previously used in the literature in the flame synthesis of binary oxides and perovskites. Their influence on the powder properties such as particle size, morphology, and phase composition has been extensively examined [38, 40, 52, 53, 143, 144]. Through a proper selection of carboxylic acids and alcohols many precursors can be dissolved in the required concentration range for SFS. A concept that is frequently used to estimate energetical contribution of a single solvent or a solvent mixture is the concept of the combustion enthalpy [38, 59, 60]. For instance, the use of high enthalpy solvents (e.g., xylene, 2-ethylhexanoic acid, etc.) is correlated with higher combustion temperatures, often increasing the crystallinity of the products but also leading to the formation of larger particles and increased agglomeration [173]. The combustion enthalpy has the unit [kJ/mol] and should be accounted for the volumetric flows of solvents that are fed into the reactor, and the values were therefore converted to [kJ/ml].

For the preliminary study on the flame synthesis of BaTiO₃ the following solvents were picked: Propionic acid (PA), iso-propanol (2-PrOH), and xylene (XE), because they satisfy the requirements defined above, namely availability, solubility, and low cost. The addition of xylene is justified by the fact that it has a much higher combustion enthalpy (−37,4 vs. −27 kJ/ml for xylene and ethanol, respectively) and thus provides higher flame temperatures, as shown by Bettini *et al.* [168] for the synthesis of TiO₂ nanoparticles. The use of carboxylic acids was found to help produce homogenous particles in the case of a LaCoO₃ perovskite [52, 53].

Teoh *et al.* summarized a criterion for the synthesis of homogeneous nanoparticles via SFS [35]. Briefly, the lack of the energy provided to the flame and the ratio values between the boiling temperature of solvents and melting temperature of precursors expressed in $T_{bp}/T_{mp} < 1$ result in varying particle sizes in micro- and nano-range. Essentially, high melting temperatures of the precursors without sufficient energy supply lead to the incomplete droplet evaporation without the precursor transiting into the gas-phase, thus favoring the droplet-to-particle conversion route and resulting in inhomogeneous (hollow or irregularly shaped) particles, which is common in conventional spray pyrolysis [56]. In contrast, increasing energy supply by adding high enthalpy solvents while keeping the T_{bp}/T_{mp} ratio above 1 was shown to produce homogeneous nanopowders through the preferred gas-to-particle conversion route as described in Chapter 4 and demonstrated by Jossen *et al.* [38]. In the present study, the precursor choice

for the synthesis of BTO is restricted, therefore the current selection is by no means optimal for an idealized SFS process, because the boiling point of TTIP (235°C) is much lower than the melting point of BA (450°C), which would result in inhomogeneous products according to the T_{bp}/T_{mp} ratio. This situation in some way circumvented by the use of the solvents with relatively high combustion enthalpy values (-20,37, -26,9, and -37,4 kJ/ml for PA, 2-PrOH, and XE, respectively), which should help in obtaining homogeneous particles. In addition, the difference between the boiling and melting points of both precursors presents difficulties for the synthesis of mixed metal oxides due to possible phase separation and dissimilar vaporization rates [169, 174]. The list of all components selected for this study is presented in Table 6-1.

The last parameter considered is the precursor concentration in the solution. Higher concentrations typically lead to higher particle collision probabilities, therefore resulting in larger and agglomerated particles, while lower concentration yield less material after the synthesis [36, 173, 175]. In this respect, experiments with varying concentrations were performed to investigate how metal concentration influences particle sizes of the as-produced BaTiO₃ powders.

Table 6-1. List of solvent and precursors selected for the preliminary study of BaTiO₃ powders with some of their properties.

No.	Name	Chemical formula	Boiling point / °C	Combustion enthalpy / (kJ/ml)
1.	Propionic acid	CH ₃ CH ₂ COOH	141.2	-20.37
2.	2-Propanol	C ₃ H ₈ O	82.5	-26.90
3.	Xylenes (mixture)	C ₈ H ₁₀	138.5	-37.4
4.	Barium acetate	Ba(CH ₃ COOH) ₂	450	-
5.	Titanium iso-propoxide	C ₁₂ H ₂₈ O ₄ Ti	235	-26.74

Thus, summarizing, the focus of the preliminary study regarding the synthesis of BaTiO₃ nanoparticles was to: (i) investigate the use of selected precursors and solvents; (ii) examine the influence of varying precursor concentrations. A list of experiments was devised accordingly, and the total precursor concentration used was varied between 0.2, 0.5, and 1M. Additionally, a single experiment was performed at a fixed precursor concentration of 0.5 M with an addition of xylene in proportion to PA and 2-PrOH to investigate the influence of adding a high-enthalpy component into the solution. The list of conducted experiments is presented in Table 6-2. The synthesis parameters i.e., the flows of the solutions and gases, and pressure in the reactor are listed in Table 6-3 and were held constant throughout all experiments. Since no synthesis parameters for BaTiO₃ are available in the literature, the selection was made based on the work by Hardt *et al.* regarding the SFS synthesis of TiO₂ nanoparticles, where the same reactor setup was used [151, 153]. The precursor feed flow was adjusted to 3 ml/min, and the dispersion gas flow was 4 ml/min. The ratio between CH₄ and O₂ was kept at 2:1 (2 and 1 slm for CH₄ and O₂, respectively) to avoid soot formation. The pressure inside the reactor was set at ~950 mbar, as the flame was found to burn stable at this value.

The solvent preparation procedure was executed as follows: BA (Sigma-Aldrich, 99%) and TTIP (Sigma-Aldrich, 97%) were used as metal precursors in 1:1 molar ratio with a total concentration according to the mixtures in Table 6-2. PA (Sigma-Aldrich, 99.5%), 2-PrOH (VWR, 99%) and XE (Roth, 98.5%) were added according to the proportions in Table 6-2. First, BA was completely dissolved in PA

under vigorous stirring at 60°C for 1 hour and then the solution was left to cool down to room temperature. After that, 2-PrOH or a mixture of it with XE was added followed by a subsequent addition of the prescribed amount of TTIP. The resulting solution was additionally stirred for an hour prior to synthesis. After the synthesis, the powders were collected from the filter and examined with respect to their physicochemical properties.

Table 6-2. List of performed experiments for the synthesis of BaTiO₃.

Sample name	Total precursor concentration / M	Solvent composition	Proportion
0.1M	0.2	Propionic acid / 2-Propanol	1:1
0.5M	0.5		
0.5MX	0.5	Propionic acid / 2-Propanol / xylene	1:0.7:0.3
1M	1	Propionic acid / 2-Propanol	1:1

Table 6-3. Process parameters during the synthesis of BaTiO₃

Liquid precursor flow / (ml/min)	CH ₄ pilot flame / slm	O ₂ pilot flame / slm	O ₂ dispersion / slm	Compressed air sheath / slm	Pressure / mbar
3	2	1	4	300	950

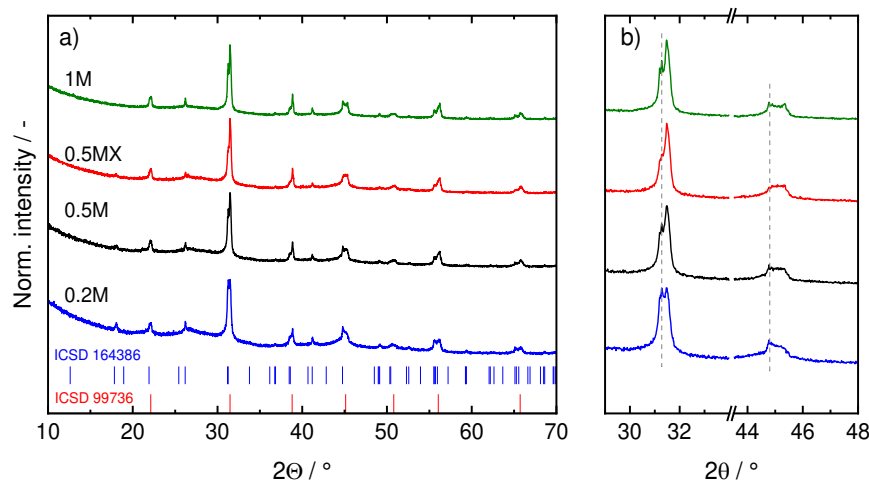


Figure 6-1. a) XRD patterns of as-synthesized BTO powders and b) details of the $2\theta = 29\text{--}34^\circ$ and $2\theta = 43\text{--}48^\circ$ region. Red tick marks indicate the expected positions for the cubic phase (ICSD 99736) and blue tick marks indicate the position of the hexagonal phase of BaTiO₃; dashed line in graph b) indicate the hexagonal phase (ICSD 164386).

First, a phase analysis via XRD was carried out. The patterns of as-synthesized BaTiO₃ powders presented in Figure 6-1 show peaks that can be attributed to the cubic phase (shown as red tick marks in Figure 6-1a) of BaTiO₃ with an additional contribution from a high-temperature hexagonal phase (shown as blue tick marks in Figure 6-1). However, it is not yet clear if the tetragonal phase of BaTiO₃ is also present in the samples, as it should be stable at room temperature according to the phase diagram in [176], since structural differences between the cubic and tetragonal phases are very negligible as was discussed in Chapter 2.2. Thus, both phases share practically the same reflection positions, therefore

complicating determination of the exact phase composition. A specific feature used to distinguish between these two phases is the characteristic broadening of the signal measured at 45° caused by the peak splitting in the case of the tetragonal phase [10, 29, 90, 177, 178]. This splitting can be directly observed for micrometer and sometimes for submicrometer-sized particles but is not clearly identifiable for the powders under study because of the interference with the hexagonal phase. The hexagonal phase is said to form above 1200°C and is usually observed due to thermal quenching [56, 177, 179]. Thermal quenching in our case is provided by the cooling cone (Figure 4-2), resulting in a steep temperature gradient on exiting the reactor zone.

Apart from the crystalline phases mentioned above, the diffraction patterns explicitly indicate the existence of some amorphous material, as suggested by a noticeable lump (halo in $24\text{-}30^\circ$ region) and the absence of a flat and defined background for all samples. Such contributions to XRD powder patterns typically symbolize the occurrence of non-crystalline particles or intermediate weakly crystalline phases that can transform to the final products under the application of heat [62, 169, 180].

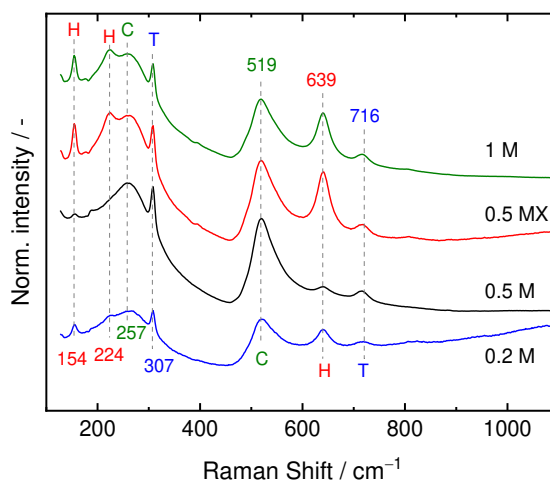


Figure 6-2. Raman spectra of as-synthesized BTO powders with dashed lines indicating positions of the most prominent bands; T: tetragonal phase (blue), C: cubic (green) phase, and H: hexagonal phase (red).

From the XRD patterns it cannot be ruled out that the BaTiO_3 samples also contain some portion of the tetragonal phase alongside cubic. In order to be able to distinguish the contributions from the cubic and tetragonal phases, the pristine powders were additionally investigated by Raman spectroscopy, which allows for a qualitative phase analysis than XRD, since Raman analysis is more sensitive towards the individual features of different phases. All spectra of pristine powders are shown in Figure 6-2. As-synthesized powders show principal symmetry bands related to cubic (257 and 519 cm^{-1}), tetragonal (307 and 716 cm^{-1}), and hexagonal phases (154 , 224 , and 639 cm^{-1}) [71, 131, 169, 177, 178, 181]. The Raman analysis therefore confirms the existence of the tetragonal phase in our as-synthesized samples. A band at 1059 cm^{-1} corresponding to the BaCO_3 impurity that is regularly present in BaTiO_3 samples wasn't found in any of the current samples, thus suggesting its absence in our powders [177].

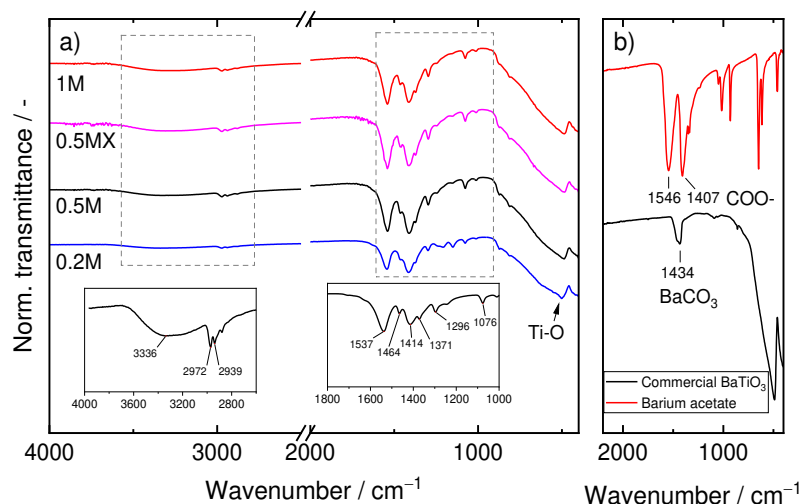


Figure 6-3. FTIR spectra of (a) as-synthesized BTO powders, (b) commercial BaTiO₃, and barium acetate. Two additional insets are shown in (a) with a more precise interpretation of the band positions.

FTIR analysis is routinely performed to provide information on the surface species. This analysis is particularly invaluable in the present case because organic residuals from combustion processes have a tendency to adsorb on the powder surface, therefore giving rise to specific features detectable via IR spectroscopy [28, 59, 181]. Thus, FTIR spectra of as-synthesized powders were acquired to provide a qualitative analysis of partially burned and unburned hydrocarbons.

ATR-FTIR spectra of the as-synthesized powders presented in Figure 6-3a show that the as-synthesized powders are contaminated with various organic groups with the most prominent of them being carboxylate and carbonyl groups [28]. Carboxylate species form a chemical bond with metals and therefore give rise to two characteristic $\nu_s(\text{COO}^-)$ symmetric and $\nu_{as}(\text{COO}^-)$ asymmetric stretching vibrations at 1414 and 1537 cm^{-1} in the bridging bidentate configuration with no characteristic for carboxylic acids C=O bond present that typically appears in the spectra as a feature around 1600 cm^{-1} , as described in Refs. [28, 59, 182-184] and additionally shown in the barium acetate spectrum (Figure 6-3b top). Additional weak intensity bands at 2972 and 2839 cm^{-1} were assigned to the symmetric and asymmetric stretching vibrations of aliphatic CH₃- and CH₂- groups ($\nu_s(\text{CH}_3/\text{CH}_2)$ and $\nu_{as}(\text{CH}_3/\text{CH}_2)$). The broad feature around 3000–3600 cm^{-1} is a characteristic feature for adsorbed hydroxyl groups. It is worth mentioning that hydroxyl groups can be also accommodated in the unit cell of perovskites as lattice defects and are also detectable by means of IR spectroscopy [185]. As stated previously, the existence of BaCO₃ impurity can be tentatively ruled out (Figure 6-3a), since no apparent bands corresponding to carbonates around 1460 and 860 cm^{-1} were found, in agreement with both XRD and Raman data [181]. To strengthen the statement regarding the absence of BaCO₃ in the as-synthesized samples, an additional FTIR spectrum of the commercially available BaTiO₃ powder (Sigma-Aldrich) synthesized by a wet chemistry method was recorded, which shows a distinctive carbonate feature at 1434 cm^{-1} (Figure 6-3b). In addition to the signals of the organic species, a band at ~ 500 cm^{-1} that represents the fundamental phonon Ti–O vibration frequency of the TiO₆ octahedra in BaTiO₃ is observed. An increase in intensity of this band is reported to be an indication of a higher sample crystallinity (Figure 6-3a) [28, 29].

To investigate thermal stability of the organic species observed and of the powders in general, simultaneous thermal analysis (STA) was employed. This technique combines thermogravimetric analysis

(TGA) and differential scanning calorimetry (DSC), and provides means of following weight loss progression accompanied by any thermal (exothermic/endothermic) events. Additional identification of the gaseous species released during the heating process is possible due to a built-in quadrupole mass spectrometer (QMS).

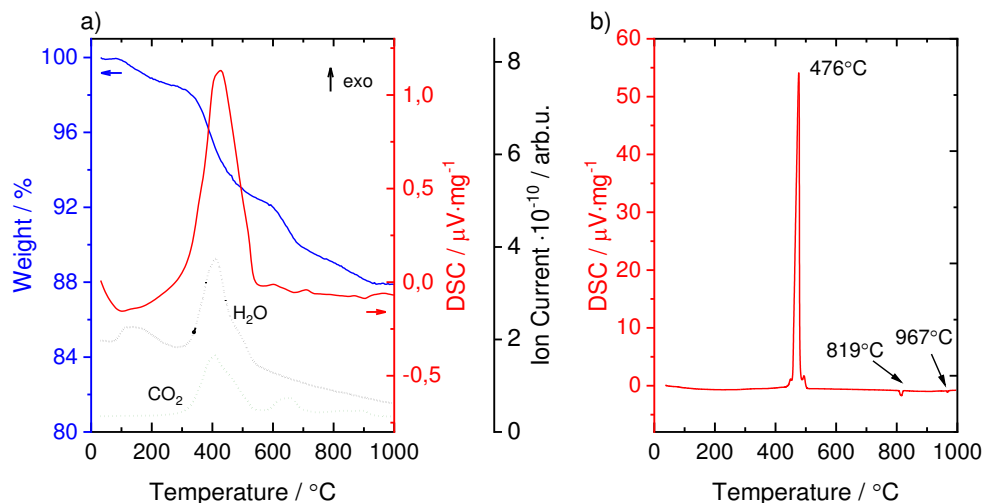


Figure 6-4. STA data of (a) as-synthesized powder synthesized from 0.2 M solution and (b) barium acetate precursor. Blue line: weight loss, red line: calorimetric data, dotted lines: mass spectra for H₂O and CO₂.

Figure 6-4a shows the STA data obtained only from 0.2 M sample, as it reflects all main features that were also observed during the analysis of the other powders. The sample demonstrates a total weight loss (blue line) of 12%, which on average constitutes around ~14% for all as-synthesized samples when heated in air up to 1000°C. Considering progression and shape of the TG curves, three regions can be distinguished within the measurement: The first one with a distinctive weight loss (~1.7%) occurring up to 300°C followed by a second step with a strong weight loss (~6.4%) up to 570°C, and the last one (~4.2%) starting from about 600°C. With the assistance of mass spectroscopy measured in parallel, the main species released during heating, OH ($m/z = 17$) and CO₂ ($m/z = 44$), were recorded. Up to ~250°C, the results suggest that physisorbed water is released, which is indicated by an endothermic peak over 100–200°C. Starting from 300°C, a simultaneous release of OH and CO₂ is spotted accompanied by a notable exothermic feature in the DSC signal over 400–500°C and marked by a dramatic weight loss, which continues up till 600°C. This exothermic event suggests a combustion reaction of the residual COO- groups [28, 186]. FTIR and TGA measurements performed on BaTiO₃ powders produced via sol-gel method showed that water can be present in the structure in form of lattice hydroxyl groups and is released on heating in the same temperature range (~400°C) as was observed in our case [169, 185, 187, 188]. Also, TG data and DSC signals match quite well with the values reported in the literature for sol-gel prepared BaTiO₃ synthesized using acetates as metal precursors, where a full conversion of the latter occurs only on application of heat [170]. This strengthens the argument that some COO- acetate groups bonded to barium probably did not completely convert to the final product during the synthesis, and therefore appear in the FTIR spectra in Figure 6-3 [28, 183, 184]. An additional faint weight loss continues after 700°C along with some weak exothermic signals indicating that the powder evolution is almost complete by 800°C.

To prove the assumption that barium acetate stays on the powder surface after synthesis, an additional STA measurement was carried out using BA (Figure 6-4b). As the DSC graph suggests, a sharp exothermic peak is seen over the 400–500°C range, which correlates well with the peak that was observed in the STA data of our BTO samples. On heating BA converts to BaCO₃, whose phase transitions are seen at 819 and 972 °C [189]. This confirms that some amount of the unreacted barium precursor indeed stays after the synthesis in as-produced powders.

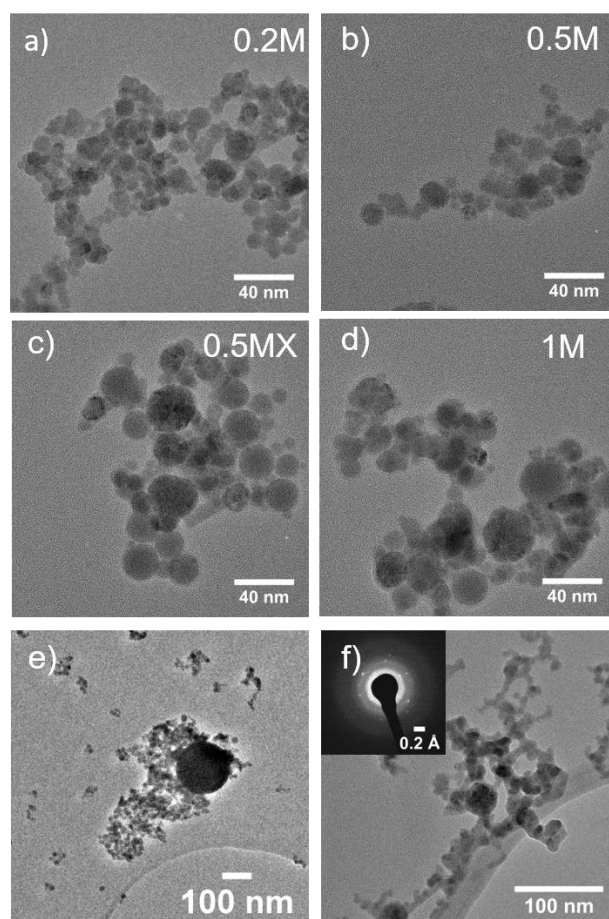


Figure 6-5. TEM images of as-synthesized BTO (a) 0.2 M, (b) 0.5 M, (c) 0.5 MX, and (d) 1M samples. Image (e) shows existence of some larger particles synthesized using same conditions as in Table 6-3, and (f) demonstrates the 0.2M sample with an electron diffraction inset.

Transmission electron microscopy (TEM) was used to analyze particle size and morphology of as-synthesized samples. The images in Figure 6-5 clearly demonstrate that produced particles are in the nanometer range with mostly spherical shape and consisting of agglomerates and aggregates. No faceted particles were noticed in any of the powders. Continued observation of the images shows that the sample with higher precursor concentration (1 M) and the one with the addition of xylene (0.5 MX) seemingly have larger particle sizes than the powders produced from lower concentrations or without xylene. Additionally, some larger particles were spotted during the observation (Figure 6-5e), whose appearance can be assigned to the use of alcohol in the solution, which can lead to precursor precipitation on the droplet surface, leading to large and inhomogeneous particles [38, 40, 144]. To investigate the matter further, particle-size distributions (PSDs) were determined by measuring particle diameters (over 100 particles counted) and fitting a log-normal particle size distribution (PSD) to the histograms.

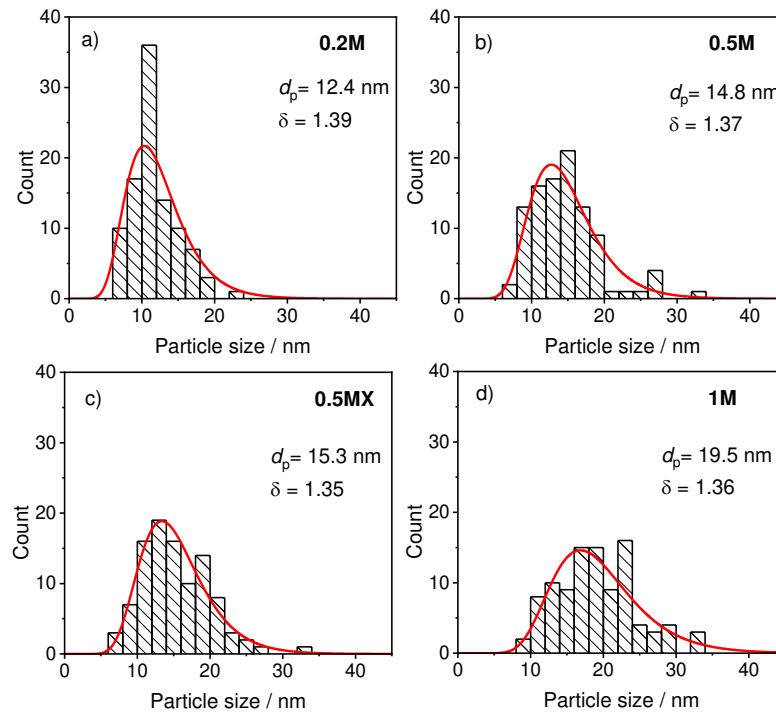


Figure 6-6. Calculated PSDs from (a) 0.2 M, (b) 0.5 M, (c) 0.5 MX, and (d) 1 M samples; d_p stands for the particle diameter in nm and δ is the geometric standard deviation.

PSDs presented in Figure 6-6 reveal that the as-produced powders have particle sizes between 12 and 20 nm and the count median diameter (CMD) increases with increasing precursor concentration. The addition of xylene also increases the particle size, which is attributed to the higher flame temperatures associated with higher combustion enthalpy and in agreement with the observations in literature [168].

In addition to TEM and XRD, the specific surface areas (SSA) of all as-synthesized powders were determined by BET measurements, from which particle sizes were calculated using Equation 5-16 given in Chapter 5.5. Additional investigations were done by performing Rietveld refinement, whereby one can extract crystallite sizes and phase ratios from XRD data. In order for a typical refinement to converge properly, only two and not three phases observed in Raman (Figure 6-2) were introduced: the cubic phase of BaTiO_3 was not included in the refinement procedure, as the refinements were unstable and provided relatively high R_{wp} values when three phases (tetragonal, hexagonal, and cubic) were introduced. Instead, only the tetragonal (ICSD card 99737) and hexagonal (ICSD card 164386) phases of BaTiO_3 were used, which resulted in more stable results and lower R_{wp} values. R_{wp} (weighted profile or goodness of fit, the smaller the R_{wp} value, the better) values in general describe the difference between the observed and calculated XRD patterns from Rietveld refinement (graphical outputs presented in Figure 6-7). The determined particle and crystallite sizes from all measurements were plotted in Figure 6-8. The extracted phase ratios from refinements and the SSA values are given in Table 6-4.

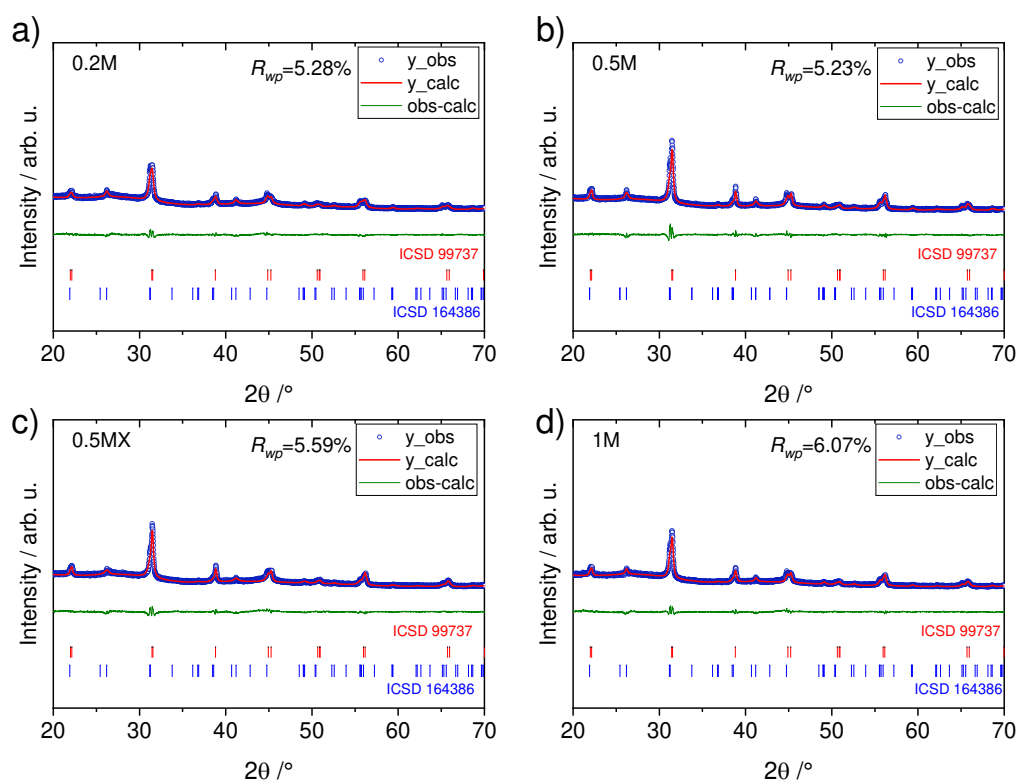


Figure 6-7. Graphical output from Rietveld refinements for as-synthesized (a) 0.2 M, (b) 0.5 M, (c) 0.5 MX, and (d) 1 M.

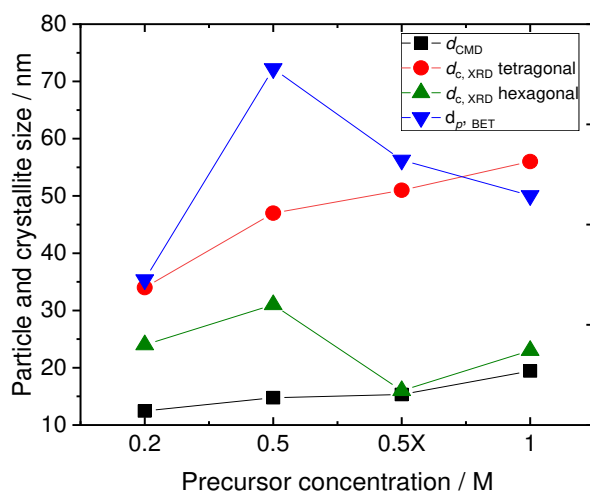


Figure 6-8. Comparison of the particle and crystallite sizes obtained from TEM, BET, and XRD versus precursor concentration. The xylene-containing 0.25 MX solution is plotted with a letter X to avoid confusion with the 0.25 M sample. Drawn lines between the data points serve to guide the eye.

Table 6-4. Phase ratios obtained from XRD and SSA values from BET of as-synthesized BaTiO₃ powders.

Sample	Phase		SSA / m ² /g
	Tetragonal / %	Hexagonal / %	
0.2 M	46.3	53.7	28.2
0.5 M	43.6	56.4	13.8
0.5 MX	48.3	51.7	17.7
1 M	52.5	47.5	19.9

As seen from Figure 6-8, the values acquired from XRD and TEM show that with increasing precursor concentration the average particle/crystallite size increases. The addition of xylene illustrates that increasing the combustion enthalpy of the solution leads to the expected increase in the particle size. Remarkable is the finding that both with increasing concentration and addition of xylene, the crystallite size corresponding to the hexagonal phase decreases while that of the tetragonal phase increases. The ratio between both phases stays practically unchanged around 50/50 with minor deviations and no identifiable trend. The particle sizes from BET are in general in good agreement with the XRD data. However, it should be mentioned that since BET is a surface-based technique that heavily depends on particle agglomeration, aggregation, and the amount of surface contaminations, a certain over- or underestimation of the particle sizes calculated from BET measurements can be expected, especially from moderately agglomerated SFS-produced, where large particles with high mass coexist with small particles as can be seen in Figure 6-5 [62]. A notably large discrepancy between the TEM and XRD values is probably due to polydispersity of the produced particles [39, 40]. Crystallite sizes from XRD are a mass-weighted property averaged over a large sample volume, whereas particle sizes calculated from TEM are based on counting statistics of a much smaller number of particles. As the TEM image suggests (Figure 6-4e), small primary particles coexist with some larger ones, therefore leading to overall larger average crystallite sizes in XRD.

In conclusion, the preliminary experiments demonstrated the feasibility of the flame-based synthesis of BaTiO₃ nanoparticles. Despite having challenges with the phase composition, the powder produced is in the nanometer range with the lowest particle size obtained from the 0.2 M concentration. The calculated phase ratios from the XRD data between the tetragonal and hexagonal phases of BaTiO₃ seem to be not connected to either concentration or solvent composition. The solvents selected for this study, i.e., PA and 2-PrOH are suitable for the synthesis of BaTiO₃ nanoparticles and will be used as a standard solution while keeping metal concentration at 0.2M. The process parameters in this preliminary study were also found adequate for the production of nanopowders. One issue that was identified is the existence of the organic rests that stay on the powder surface after the synthesis, which can lead to undesired carbonate formation over time and therefore performance deterioration of the final products [190].

6.1.2 Investigation of the influence of solvent composition

In the preceding section, the optimal synthesis parameters and precursor/solvent solution mixture was determined. In addition to the preliminary investigation, the list of selected solvents was expanded with the following objectives: (i) diminishing the amount of the undesired secondary hexagonal phase; (ii) controlling the amount of carbon contamination on the surface of the as-produced powders. Therefore, three new solvents were included: glacial acetic acid (AA, VWR, 99,8%), 2-ethylhexanoic acid (EHA, Sigma-Aldrich, 99%), and absolute ethanol (EtOH, VWR, 99,8%). AA is the simplest carboxylic acid with only two carbon atoms in its structure, and therefore has a lower combustion enthalpy and boiling

point than PA (118 and 141°C, -15,29 and -20,37 kJ/ml, respectively). 2-EHA is an oily liquid that consists of a long and branched carbon chain, showing high combustion enthalpy value of -26,95 kJ/ml and high boiling point of 223°C. An interesting fact about EHA is that it was shown to aid the production of fine and homogeneous particles because it promotes microexplosions during droplet evaporation as studied by Rosebrock *et al.* [143, 144]. Thus, it was decided to test its applicability to the synthesis of BaTiO₃ powders. Finally, EtOH (boiling point 78°C and combustion enthalpy -23,4 kJ/ml) was chosen instead of 2-PrOH to study the stability of TTIP in the solution, and to investigate if the lower enthalpy value of EtOH than that of 2-PrOH (-26,9 kJ/ml) has any influence on the synthesis. All solvent combinations are listed in Table 6-5 with the combustion enthalpy values calculated by the mixture rule, and the boiling points were calculated using the Antoine equation. All synthesis were performed with exactly the same process parameters except for the O₂ dispersion gas value, which was increased to 6 slm to aid the formation of smaller particles through the creation of finer spray droplets with higher dispersion gas values [37]. The metal concentration was kept at 0.2 M. The combustion enthalpy approach reflects differences between various solvents, thus allowing for a better comparison of diverse solvent combinations.

Table 6-5. List of solvent mixtures with corresponding calculated combustion enthalpy values and boiling points for the synthesis BaTiO₃.

Sample name	Solvent composition	Combustion enthalpy / kJ/ml	Boiling point / °C
AP	AA / 2-PrOH	-21.3	93
PP	PA / 2-PrOH	-23.7	97
AE	AA / EtOH	-19.6	92
PE	PA / EtOH	-22.0	95
AEH	AA / 2-EHA	-22.7	126
PEH	PA / 2-EHA	-25.2	138

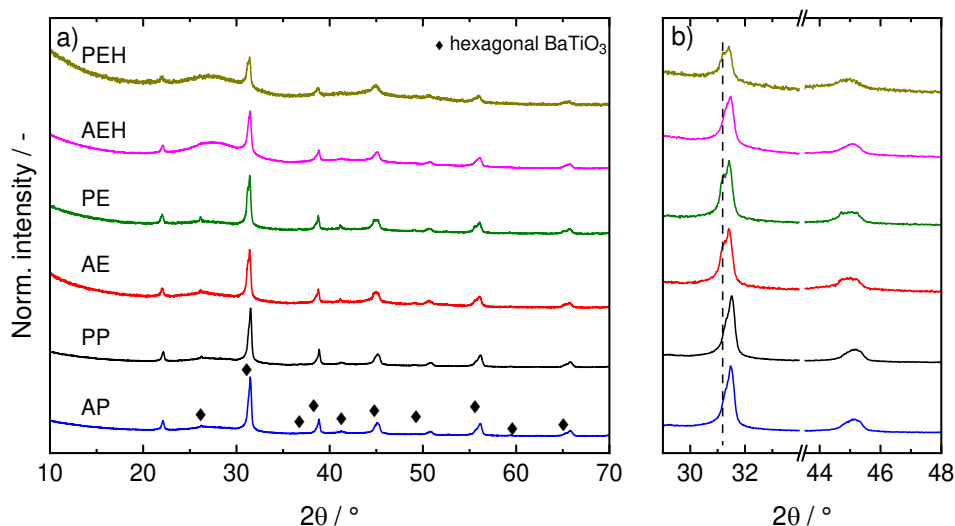


Figure 6-9. XRD patterns of as-synthesized BTO powders from various solvents (a) and details of the $2\theta = 29\text{--}34^\circ$ and $2\theta = 43\text{--}48^\circ$ region (b). ♦ and dashed line indicate the peak positions of the hexagonal phase of BaTiO₃.

As-produced powders were analyzed with XRD and the corresponding patterns are presented in Figure 6-9. It is directly evident from the graph that powders from the solutions containing EHA (AEH and PEH) are much less crystalline than the rest of the powders, which is manifested in a larger lump around $24\text{--}30^\circ$ and a visible decrease in the peak intensities of the diffraction maxima. There is no conclusive argument why the powders are less crystalline with the use of EHA, but it might be related to the higher viscosity and boiling point of the substance. On a closer inspection of the ethanol-based solutions (AE and PE), a slightly higher background ($24\text{--}30^\circ$) than in the PA-based solutions is noticeable. Common for all powders is the existence of the hexagonal phase, as displayed in the magnified portion of Figure 6-9, which suggests that the phase forms regardless of the solvent composition.

To elucidate the reason for the lower crystallinity and peak intensities in the EHA-based samples and to additionally obtain information on the state of organic contaminations, FTIR spectra were collected. For that reason, 2-PrOH-based powders (AP and PP) and one 2-EHA-based sample (AEH) were further investigated to allow for a comparison between the various carboxylic acids used during the solvent preparation. The powders from the EtOH solutions were also investigated but are not shown as the observed differences between them and the samples with 2-PrOH are virtually non-existent. FTIR spectra of the three selected powders are presented in Figure 6-10.

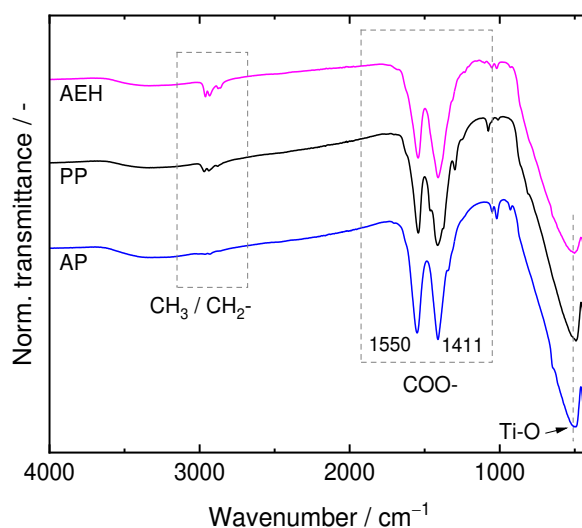


Figure 6-10. ATR-FTIR spectra of as-synthesized BTO powders produced from AP, PP, and AEH solutions. Dashed rectangles highlight main features of the spectra.

The spectra are dominated by the strong features belonging to the carboxylate COO^- group over $1400\text{--}1500\text{ cm}^{-1}$ range, in accordance with the previous FTIR measurements (Figure 6-3a). Moreover, a distinct difference between the samples is noticeable over $2900\text{--}2960\text{ cm}^{-1}$ (dashed rectangle on the left in Figure 6-10), where the AP sample produced from acetic acid and 2-PrOH shows only weak intensity bands of $\text{CH}_3/\text{CH}_2^-$ groups compared to the rest of the examined samples. Another clear difference between the samples is a lower intensity of the Ti-O band at 500 cm^{-1} in the EHA-based sample, which confirms its lower crystallinity observed in XRD.

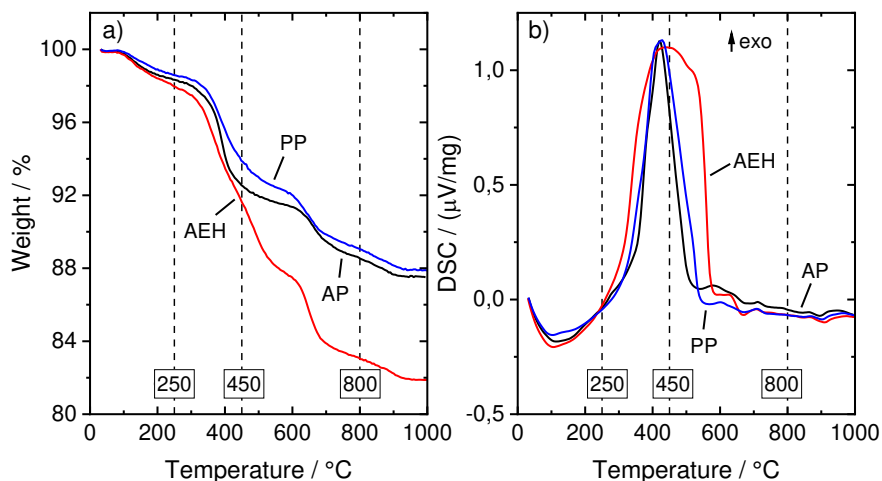


Figure 6-11. TGA (a) and DSC (b) data of as-synthesized AP, PP, and AEH samples in air heated at 20°C/min to 1000°C.

STA measurements (Figure 6-11) were performed to unravel the differences in the powders through the thermal evolution. The progression of both TGA and DSC signals is very similar to that observed previously (Figure 6-4). However, in the case of the EHA-based solution, the observed total weight loss is substantially higher (~12% for the PrOH-based powders and ~18% for the EHA sample, respectively). The exothermic feature of the COO- combustion at ~450°C is considerably broader than for the PrOH-based powders and is accompanied by a much steeper weight loss. This fact suggests that this sample has more unreacted species that contribute to the overall high weight loss triggered by heating.

Three distinctive regions can be extracted from the TGA data: A region of the initial weight loss around 250°C, a region of the intensive weight loss around 450°C, and the region with almost no weight loss above 800°C. Performing FTIR of the powders heated at these three temperatures might provide additional details on the evolution of the organic species, whereas XRD might hold information regarding possible phase transitions in general. It can potentially help understand the differences suggested earlier by XRD and TGA data. For this reason, the three powders (AP, PP, AEH) were annealed based on the STA results for three hours in O₂ atmosphere at three target temperatures (250, 450, and 800°C) with the collection of FTIR and XRD data afterwards (Figure 6-12).

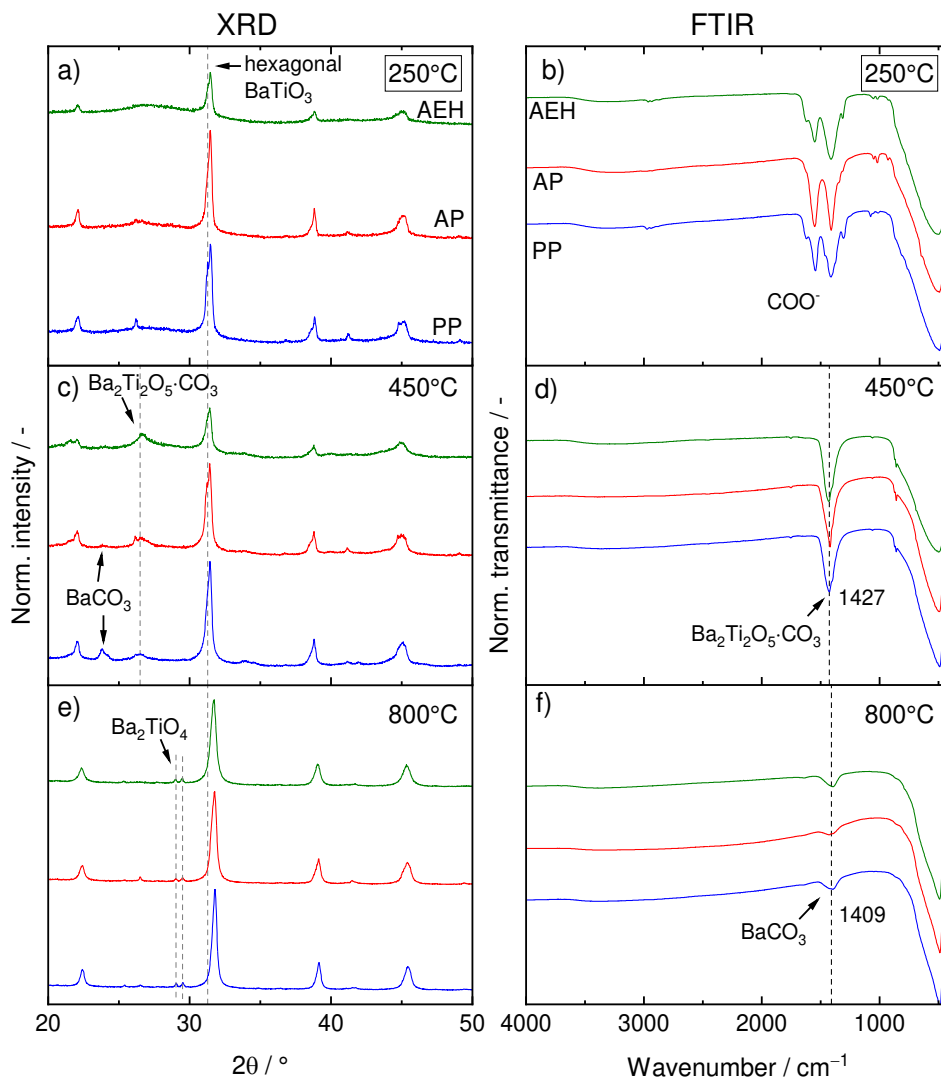


Figure 6-12. XRD (a, c, e) and FTIR (b, d, f) data of the powders from different solvents at 250, 450, and 800°C.

XRD patterns show that the powders heated at 250°C are almost identical to the as-synthesized ones with no changes observed. At 450°C, the formation of a new weakly crystalline phase with the main peak positioned at 26.6° along with traces that were assigned to the BaCO₃ contamination at ~24° is evidenced for all samples in XRD. The presence of the weakly crystalline phase is explicitly pronounced in the AEH sample. After consulting with literature, the unknown phase was identified as an intermediate oxycarbonate Ba₂Ti₂O₅·CO₃ phase [29, 169, 177]. On further heating at 800°C the oxycarbonate phase disappears, and two new signals appear around ~30°. These peaks belong to a polytitanate Ba₂TiO₄ phase (ICSD card 29389), which is known as a by-product of the oxycarbonate decomposition around 500–700°C in the Ba-rich environment [191]. The presented diffraction patterns also reveal a shift in the tetragonal/hexagonal phase ratio as denoted by a gradual decrease in the intensity of the left shoulder at 31°. IN summary, the XRD data suggest that heat treatment at temperatures as high as 800°C and above is a possible way to reduce the amount of the hexagonal phase and improve the crystallinity of BaTiO₃ powders.

FTIR measurements of the powders heated at 250°C shown in Figure 6-12b reveal that the spectra are almost identical to that of the as-synthesized samples, which is in line with the TGA measurements that

show minor losses due to water desorption in that temperature range. As the annealing temperature increases to 450°C, carboxylate peaks are no longer visible, and a new set of bands resembling those of BaCO₃ appears around 1419 and 858 cm⁻¹. However, on closer inspection, these bands were attributed to the bands belonging to a similar intermediate oxycarbonate Ba₂Ti₂O₅·CO₃ phase, as described in Refs. [28, 29, 169, 183]. This phase has been shown to form by the reaction between CO₃-containing species (e.g., barium carbonate), TiO₂, and BaTiO₃, and is commonly observed during the drying stage for sol-gel prepared BaTiO₃ powders [28, 169]. The emergence of the CO₃-like species in our FTIR data on heating at 450°C in O₂ atmosphere indicates the oxidation of the COO⁻ group (exothermic event over the 350–600°C range in TGA in Figure 6-11) and their subsequent conversion to carbonates. This is both in good agreement with the literature and present measurements (Figure 6-4) on the carbonate formation from precursor salts containing carboxylate COO⁻ groups [28]. On further heating to 800°C, the Ba₂Ti₂O₅·CO₃ intermediate phase decomposes and transforms into highly crystalline powders noticeable by the high intensity of the Ti–O band along with minor traces of BaCO₃ at 1409 cm⁻¹.

TEM images were additionally acquired for the PP powder to illustrate the difference in the particle size between pristine and calcined at 800°C powders (Figure 6-13). Provided TEM images show an expected increase in the particle size on heating and partial sintering of the particles.

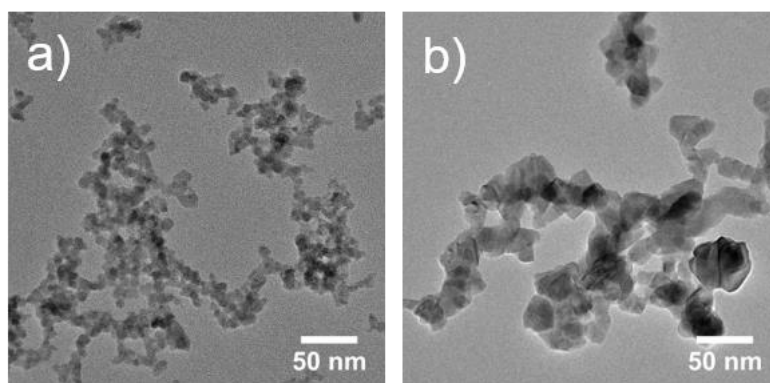


Figure 6-13. TEM images of (a) as-produced and (b) heat-treated at 800°C for three hours BaTiO₃ powders produced from PP (propionic acid/2-propanol) solution.

In conclusion, a variety solvent combinations and their effect on the synthesis of BaTiO₃ powders were examined. An interesting finding is that despite having comparable or slightly higher combustion enthalpy values, the powders produced from the EHA-based solutions are less crystalline than the powders from carboxylic acid/alcohol mixtures. The powders from the EHA solution show on average higher weight losses when heated to 800°C, which indicates a larger amount of organics as shown by TGA.

Regardless of the solvent composition, all powders demonstrate an exothermic reaction at 350–600°C in TGA, which indicates a strong oxidation reaction involving the COO⁻ groups from barium acetate to form the intermediate Ba₂Ti₂O₅·CO₃ oxycarbonate phase. The latter decomposes on further heating to BaCO₃, Ba₂TiO₄, and BaTiO₃. Heat-treatment allows to achieve a cleaner surface, higher crystallinity, reduced presence of the hexagonal phase while preserving the particle size in the nanometer range as shown by TEM (Figure 6-13), albeit with visibly increased agglomeration and particle size and some minor carbonate contamination. By using diverse solvents, the desired effect of decreasing carbon contaminations and possibly preventing formation of the hexagonal phase in the as-synthesized samples was not achieved. A possible improvement in this respect can be potentially accomplished by performing

a wide range substitutional doping of the initial BaTiO₃ perovskite structure by introducing new elements on either A- or B-site, such as Sr or Zr, respectively.

6.2 Synthesis of Ba_xSr_{1-x}TiO₃ nanoparticles

In the introductory part, energy sustainability was discussed in terms of hydrogen and oxygen production in photocatalytic processes such as the water-splitting reaction. In this respect, titanate perovskites have been closely examined in the literature in connection with their ability to produce hydrogen from water upon illumination with UV light. Among titanates, SrTiO₃ is by far the most studied and best performing photocatalyst. It is nevertheless of certain scientific interest to further examine the titanate perovskite structure and exploit its key advantages such as structural versatility in terms of substitutional doping and non-toxic nature. For example, in the case of SrTiO₃, the A site can be substituted by larger Ba atoms. However, the influence of this effort on the catalytic properties of Ba_xSr_{1-x}TiO₃ ceramics has not been studied in the literature to the best of my knowledge. Therefore, the focus of this chapter is to perform a wide-range substitution study of the initial SrTiO₃ structure with Ba via SFS. The synthesized powders are to be extensively characterized and then examined with respect to their photocatalytic performance in for photocatalytic water splitting.

In the preceding chapters, the practicality of performing sprayflame synthesis of BaTiO₃ nanoparticles was shown. Though the powder synthesis itself can be described as successful, the following challenges were recognized: (i) as-synthesized materials are not phase-pure as evidenced by the existence of the undesired hexagonal phase of BaTiO₃; (ii) contamination with organic moieties (mostly acetate groups) on the powder surface originating from the combustion processes. Therefore, a post-synthesis heat-treatment step at 800°C is needed to improve crystallinity, surface powder purity, and phase composition of the powders. It was shown that for powders synthesized with the initially proposed PA/2-PrOH as solvent, heating for 3 hours at 800°C transformed the as-synthesized material with carbonaceous contaminants to the final BaTiO₃ product and to secondary phases such as Ba₂TiO₄ or BaCO₃. However, the effect of these secondary phases on the photocatalytic activity has not been studied before. The powders stay in the nanometer range, as showed by the TEM image in Figure 6-13b.

Another open question that will be investigated is, whether substitution of the flame-produced BaTiO₃ nanopowders might be a way for steering the phase composition towards a decreasing fraction (ideally: completely suppressing) of the hexagonal phase in the as-synthesized samples. Additionally, considering the wide variety of the available phases for BaTiO₃ (cubic, tetragonal, hexagonal), an attempt at assigning the catalytic activity to one of the mentioned phases is of certain scientific interest. In the case of pure BaTiO₃, the tetragonal phase was shown to be favorable in photocatalytic reactions [22].

Table 6-6. List of the synthesized Ba_xSr_{1-x}TiO₃ compositions.

Sample name	Intended composition
BTO	BaTiO ₃
BSTO-20	Ba _{0.8} Sr _{0.2} TiO ₃
BSTO-40	Ba _{0.6} Sr _{0.4} TiO ₃
BSTO-50	Ba _{0.5} Sr _{0.5} TiO ₃
STO	SrTiO ₃

Table 6-7. Process parameters during the synthesis $\text{Ba}_x\text{Sr}_{1-x}\text{TiO}_3$ powders.

Precursor solution flow / (ml/min)	CH_4 , pilot flame / slm	O_2 , pilot flame / slm	O_2 dispersion-gas / slm	Compressed air sheath flow / slm	Pressure / mbar
3	2	1	6	300	950

The process parameters for the synthesis of $\text{Ba}_{1-x}\text{Sr}_x\text{TiO}_3$ powders were adopted from the previous synthesis of BaTiO_3 powders and are listed in Table 6-7. The solvents used were PA and 2-PrOH, mixed in 1:1 ratio. Strontium acetate (Sigma-Aldrich, 99%) was chosen as precursor, which has a melting point of 380°C . The total metal precursor concentration was 0.2 M. An overview of the synthesized compositions is given in Table 6-6. Compositions with varying Sr concentrations were chosen to investigate 1) the catalytic performance of BaTiO_3 and SrTiO_3 ; 2) if the intermediate compositions with Sr concentration $x = 0.2, 0.4, \text{ and } 0.5$ can improve the phase composition of the as-synthesized powders towards reducing the amount of the hexagonal phase. An additional question was to investigate if the hexagonal phase of BaTiO_3 detected in the as-synthesized samples has any impact on the catalytic activity of the powders.

6.2.1 Characterization of as-synthesized $\text{Ba}_x\text{Sr}_{1-x}\text{TiO}_3$ powders

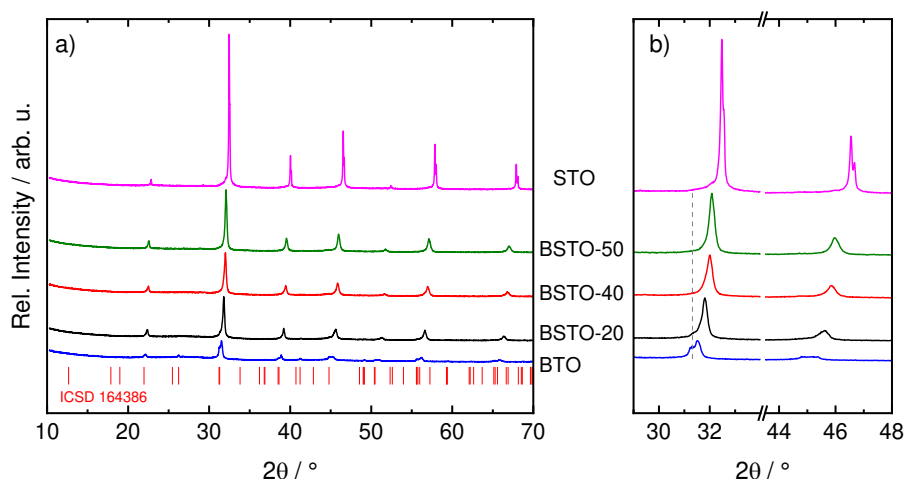


Figure 6-14. XRD patterns of (a) as-synthesized BSTO powders and details (b) of the $2\theta = 29\text{--}34^\circ$ and $2\theta = 43\text{--}48^\circ$ region. Red tick marks indicate the positions for the hexagonal phase of BaTiO_3 .

The phase composition of as-synthesized $\text{Ba}_{1-x}\text{Sr}_x\text{TiO}_3$ powders was controlled with XRD (Figure 6-14). The XRD patterns indicate cubic structure for all samples except for the BTO and BSTO-20 powders, both of which reveal additional peaks corresponding to the hexagonal phase of BaTiO_3 [62, 131]. This phase is formed above 1200°C and is observed due to thermal quenching downstream the reaction zone [56, 177, 179]. One can see a clear contribution at 31° from the hexagonal phase in the pure BTO powder and a minor one in BSTO-20 (Figure 6-14b). This case shows that the amount of the hexagonal phase in the pristine BaTiO_3 powder can be reduced by introducing moderate concentrations of Sr in the range of 20%. At Sr concentrations $x > 0.2$, no contributions from the hexagonal or any other phase than cubic were found. This is in accordance with the observations reported in literature that the smaller Sr atoms preferably stabilize the cubic crystal structure of BaTiO_3 [25, 86].

It is visible from Figure 6-14a that peak positions shift towards higher 2θ values with increasing strontium content which is explained by the smaller ionic radius of Sr^{2+} compared to Ba^{2+} (1.44 and 1.61 Å, respectively). The observed peak shifting towards higher angles also suggests that the cell unit is growing smaller, since cubic SrTiO_3 has an a parameter of ~ 3.90 Å as opposed to cubic BaTiO_3 with roughly ~ 4.01 Å. In addition, the pattern belonging to the STO sample demonstrates a significantly higher crystallinity than the rest of the samples as can be concluded from the high intensity of the reflections observed. Overall, crystallinity increases with increasing Sr amount in the samples. The smaller FWHM (full width at half maximum) values for SrTiO_3 suggest that the crystallite size is larger than in the rest of the samples.

In the case of BaTiO_3 , tetragonal and cubic phases can be both present at room temperature in the same material, as was discovered previously in pure BaTiO_3 samples by Raman spectroscopy (Figure 6-2). The tetragonal phase is recognizable by the characteristic peak splitting at 45° into the (002) and (200) reflections in XRD [62, 131, 192]. Despite the fact that a broadened signal is indeed observed, a precise phase analysis of the nanosized powder diffraction pattern is difficult, and additional measurement techniques (e.g., Raman spectroscopy) are mandatory in such cases for clarification [71].

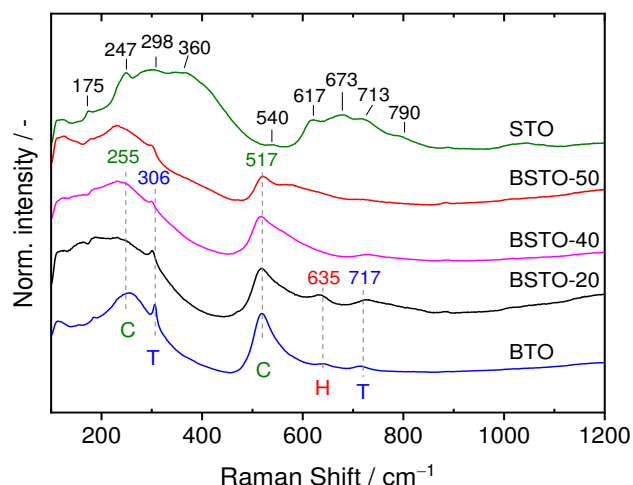


Figure 6-15. Raman spectra of as-synthesized BTO, BSTO-20, BSTO-40, BSTO-50, and STO powders. Dashed lines and tick marks indicate positions of the most prominent bands; T: tetragonal phase (blue), C: cubic (green) phase, and H: hexagonal phase (red).

As discussed above, from the XRD patterns it cannot be completely ruled out that the BTO sample also contains some tetragonal phase of BaTiO_3 . Therefore, all powders were analyzed by Raman spectroscopy that allows for a qualitative phase analysis and provides additional resolution towards structural features of individual phases (Figure 6-15). The BTO sample shows two main signals at ~ 255 and 517 cm^{-1} that can be assigned to the cubic phase of BaTiO_3 , which normally should not be visible according to symmetry restrictions [193]. However, the appearance of these bands is explained by the fact that the cubic phase shows some distortions or deviations across the whole material, which then manifest in some Raman-active modes [131].

The feature spotted at 635 cm^{-1} and identifiable only for BTO and BSTO-20 can be attributed to the hexagonal phase of BaTiO_3 , thus fully supporting the XRD data in Figure 6-15 and in accordance with literature [177]. A sharp peak at 306 cm^{-1} along with a broad signal at 717 cm^{-1} confirms the presence of the polar-active tetragonal phase in the BTO sample [131, 193]. Both peaks are also seen for higher

Sr concentrations (except for SrTiO₃) as a shoulder at 304 cm⁻¹ with decreasing intensity and shifting to lower wavenumbers, which indicates a decreasing ratio between the *c* and *a* cell constants of the tetragonal phase and thus marks the gradual stabilization of the cubic phase. The Raman spectra of SrTiO₃ show two broad characteristic bands at 200–500 and 550–800 cm⁻¹, which are related to the second-order scattering of the cubic phase in strontium titanate [166]. Even though the cubic symmetry forbids any first-order Raman activity, three additional peaks are clearly identifiable at 175, 540, and 790 cm⁻¹. Their appearance is ascribed in the literature to the local breaking of the cubic symmetry, which is caused by defects such as impurities and oxygen vacancies often occurring in perovskite materials [166]. Some additional contributions can be seen at 247, 298, 360, 617, 673, and 719 cm⁻¹, which is in good agreement with the measurements conducted by Rabuffetti *et al.* [166]. Despite the fact that all powders under study were prepared in a combustion process, it is important to stress that no indication of BaCO₃ impurities was found in any of the samples. BaCO₃ is generally represented by a series of peaks around 24–25° in the XRD pattern and by a band around 1060 cm⁻¹ in the Raman spectra [29, 62, 177, 192]. Both features are missing in the samples under investigation.

It is commonly observed that nanomaterials with high surface areas made by flame synthesis adsorb partially-burned combustion products [59]. IR spectroscopy is a reliable method to identify these species due to their characteristic spectral signatures. Surface contaminations are important to control, since they may negatively affect the materials properties and performance, especially in the field of catalysis where surface reactions play a major role in the overall catalytic activity.

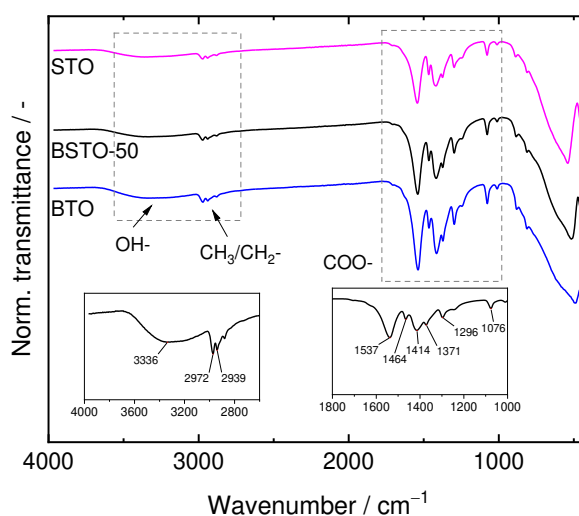


Figure 6-16. ATR-FTIR spectra of as-synthesized BTO, BSTO-50, and STO powders with a detailed inspection of the most prominent spectral features.

ATR-FTIR spectra of the three as-synthesized powders are presented in Figure 6-16, as they represent well the rest of the samples. The spectra show that the powders are contaminated with various organic groups with the most prominent of them being the carboxylate group (COO⁻, 1300–1600 cm⁻¹) and carbonyl groups (CO-, 1000–1300 cm⁻¹) as previously seen in Figure 6-3 [28]. The carboxylate species form a chemical bond with metals and therefore give rise to two characteristic $\nu_s(\text{COO}^-)$ symmetric and $\nu_{as}(\text{COO}^-)$ asymmetric stretching vibrations at 1414 and 1537 cm⁻¹ in the bridging bidentate configuration as described in [28, 59, 170, 182-184]. Additional bands of weak intensity assigned to the symmetric and asymmetric stretching vibrations of aliphatic CH₃- and CH₂- groups ($\nu_s(\text{CH}_3/\text{CH}_2)$ and $\nu_{as}(\text{CH}_3/\text{CH}_2)$) spotted at 2972 and 2939 cm⁻¹, respectively. The broad band around 3000–3600 cm⁻¹ is

a characteristic feature for adsorbed hydroxyl groups. As mentioned before, commonly observed BaCO_3 contamination originating from a reaction between barium and CO_2 can be tentatively ruled out, since no apparent bands corresponding to the carbonates around 1460 and 860 cm^{-1} were found, in agreement with both XRD and Raman data [181].

Particle size and morphology were characterized using TEM with the representative images of all as-synthesized powders shown in Figure 6-17. The particles are fairly agglomerated having a spherical particle shape as commonly observed for flame-produced powders [40, 62]. The average particle size was obtained from fitting a log-normal particle size distribution (PSD) to the histograms with the values presented in Figure 6-17. The calculated values demonstrate a tendency towards smaller particle sizes with increasing strontium content. However, some individual particles with larger than average particle sizes can be found in all samples, which might be indicative of a bimodal particle size distribution. This is clearly demonstrated in the case of STO, where some much larger than average particles were observed ($\sim 200\text{ nm}$) (Figure 6-17f), which also supports the conclusions drawn based on the high maxima intensity of this sample in XRD. The higher crystallinity of Sr-containing samples is also obvious from the clear high contrast in the selected-area electron diffraction (SAED) pattern (shown as insets) that are in contrast to the pristine BaTiO_3 and BSTO-20 samples, which show a much more diffuse diffraction pattern. These results are in accordance with XRD measurements.

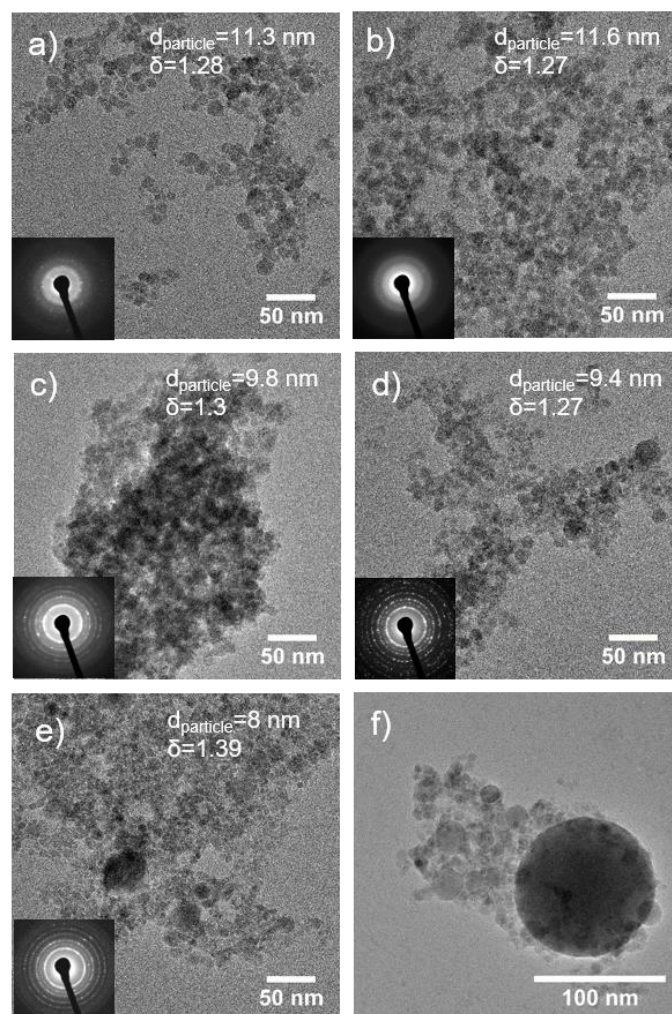


Figure 6-17. TEM images of as-synthesized BTO (a), BSTO-20 (b), BSTO-40 (c), BSTO-50 (d), and STO (e) samples with corresponding SAED patterns (shown as insets). An additional image of the STO sample (f) that shows large and small particles.

The materials were examined regarding the carbonaceous species detected in FTIR by a simultaneous thermal analysis (STA), which combines TGA and DSC measurements. STA allows tracking the weight loss and assigning it to the corresponding thermal processes. The measurements were carried out in synthetic air to potentially oxidize/burn adsorbed species.

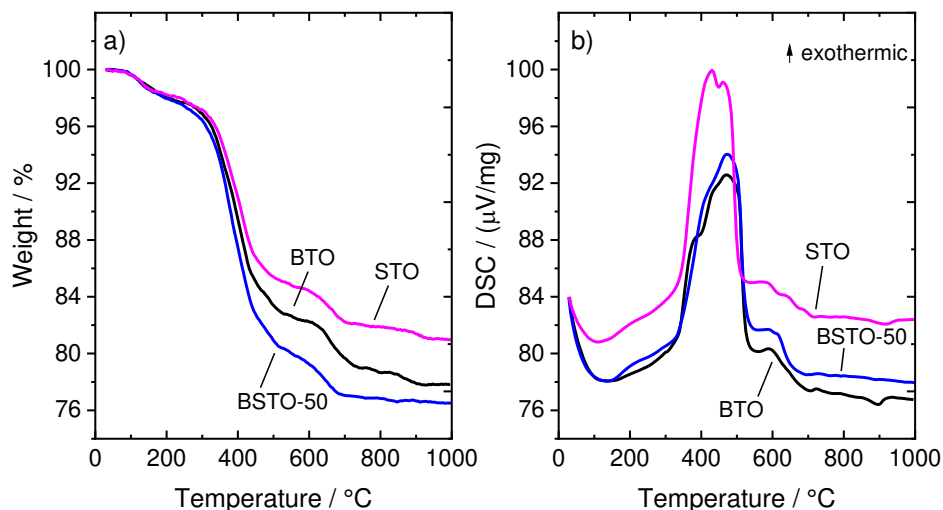


Figure 6-18. TGA (a) and DSC (b) data of as-synthesized BTO, BSTO, and STO samples in air heated at 20°C/min to 1000°C.

The TGA curves in Figure 6-18 for three powders (BTO, BSTO-50, and STO) show a similar pattern to what was observed previously across all samples with a total weight loss constituting between ~20 and 24%. After a minor weight loss around 100°C, all samples show a two-step process around 400 and 600°C. The corresponding DSC signals display an endothermic feature around 100°C, which is known to correspond to the removal of the physisorbed water. The measurements are dominated by a strong exothermal signal around 400°C and a shoulder at 600°C. These results can be attributed to the removal of acetate groups and concurrent formation of the intermediate oxycarbonate phase, as was previously observed in Figure 6-4 [28, 170, 183]. They combust on heating and then produce carbonates or participate in further reactions whereby secondary phases may form [28]. TG and DSC measurements show that the materials stabilize around 750°C indicating no further thermal events. Overall, the observed TG results essentially reproduce those obtained earlier for pure BaTiO₃ samples, again bringing to the attention the incomplete precursor conversion during the combustion process. A thorough investigation was conducted by Mos *et al.* [170] regarding the decomposition properties of strontium acetate in SrZrO₃ powders, showing that strontium acetate produces an exothermic feature around 400–600°C, which is in very good agreement with the present and previous observations. Thus, in order to clean the powder surface, a temperature of 800°C was chosen based on the TGA data obtained to calcine the as-synthesized materials.

6.2.2 Characterization of heat-treated Ba_xSr_{1-x}TiO₃ powders

Heat-treatment was applied for only 3 hours at 800°C under oxygen atmosphere to minimize the effect of temperature on particle size growth and at the same time to provide the desired cleaning effect for the surface. The annealed samples were then characterized using XRD, FTIR, Raman, and TEM. Only three powders were selected for further characterization: BTO, BSTO-50, and STO, as the photocatalytic performance of these samples was of prime interest than that of the remaining samples.

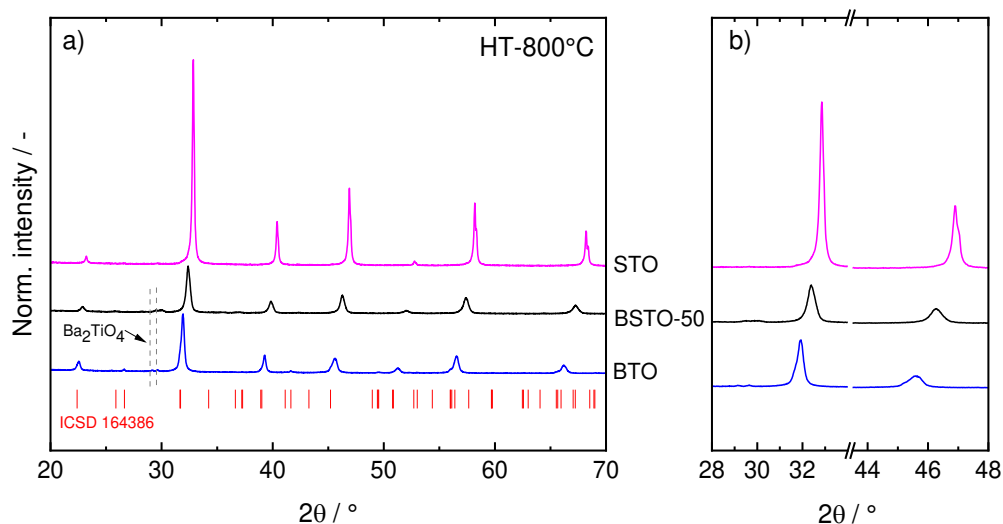


Figure 6-19. XRD diffraction patterns of heat-treated $\text{Ba}_{1-x}\text{Sr}_x\text{TiO}_3$ samples (a) with a magnified portion of the $2\theta = 26\text{--}34^\circ$ and $2\theta = 44\text{--}48^\circ$ region (b). Red ticks mark the positions of the hexagonal phase of BaTiO_3 .

The XRD patterns presented in Figure 6-19 reveal increased crystallinity of the heat-treated samples compared to the pristine ones indicated by the sharp and narrow diffraction signals. The amount of the hexagonal phase in the heat-treated samples decreased compared to the as-synthesized BTO powder, as can be seen by the decreased intensity of the peak at $\sim 31^\circ$. The characteristic peak splitting at $\sim 45^\circ$ expected for the tetragonal phase of BaTiO_3 is not readily visible after heat-treatment [192]. In addition, traces of the barium orthotitanate phase Ba_2TiO_4 could be identified in BTO and BSTO-50 based on the appearance of two new minor signals at 29.1 and 29.6° (Figure 6-19b) [194]. Beauger *et al.* proposed that the reaction between barium carbonate and barium titanate leads to the formation of the orthotitanate phase [191]. It is a distinct possibility that in the present case first the adsorbed carboxylate group converts either directly to carbonates or to the metastable $\text{Ba}_{2-x}\text{Sr}_x\text{TiO}_5\cdot\text{CO}_3$ phase on heating, and then reacts with $\text{Ba}_{1-x}\text{Sr}_x\text{TiO}_3$ to finally produce the metatitanate $\text{Ba}_{2-x}\text{Sr}_x\text{TiO}_4$ phase [169, 191, 195]. A faint shift towards higher 2θ angles was noticed for the BSTO sample (Figure 6-19), indicating that apparently a partial substitution of the Ba_2TiO_4 phase with strontium took place. The emergence of Ba_2TiO_4 is identical to the case described previously for pure BTO samples in Chapter 6.1.

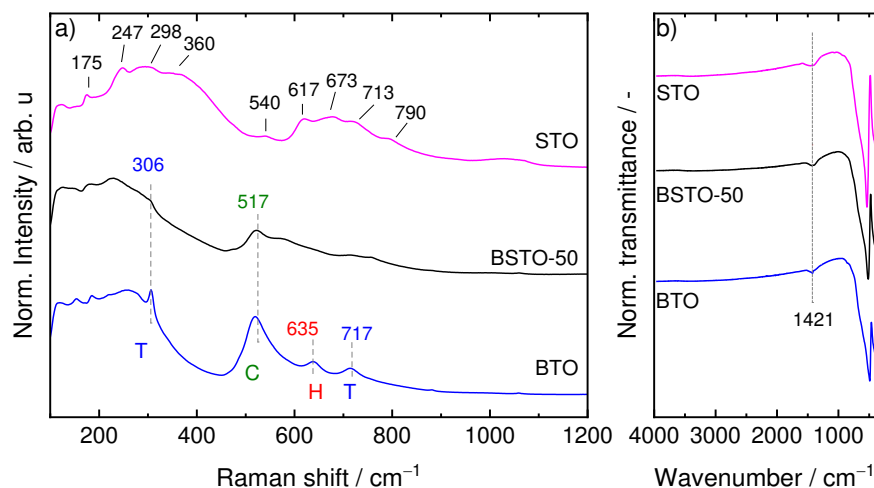


Figure 6-20. Raman (a) and FTIR (b) spectra of heat-treated at 800°C BTO, BSTO and STO samples. Dashed lines indicate positions of the most prominent bands; T: tetragonal phase (blue), C: cubic (green) phase, and H: hexagonal phase (red).

Additional analysis of the phase composition was done by Raman measurements with three representative samples shown in Figure 6-20a. The hexagonal phase feature is still present at 638 cm^{-1} in the Raman spectrum of the heat-treated BTO sample, thus confirming the XRD results (Figure 6-19b). The Raman spectra of the heat-treated samples are identical to those of the as-synthesized ones (Figure 6-15) and show the presence of the tetragonal phase as suggested by the bands at 306 and 717 cm^{-1} . Significant changes can be seen in the FTIR spectra of the heat-treated samples, namely that they are practically free from any carbonaceous species after calcination at 800°C (Figure 6-20b). Only an insignificant carbonate contamination is visible as a low-intensity band around 1421 cm^{-1} . Interestingly, no carbonate contaminations were found in the XRD patterns of the heat-treated powders, therefore suggesting that that carbonates are present only on the surface of the powders and not as a crystalline phase.

The particle morphology and size of the annealed materials were analyzed by TEM. It is clear from the images in Figure 6-21 that the initial spherical shape of the as-synthesized particles gradually evolves into a more faceted morphology. The powders are more agglomerated and show signs of sintering and densification processes. This is an expected result, since powders with high surface areas and small particle sizes have a natural propensity for much faster sintering rates plus the contribution of surface defects on high-surface particles, and therefore an expected increase in the particle size upon heat-treating [196]. However, despite the three-hour calcination, this increase is not dramatic, as the powders still stay in the nanometer range. Count median diameter of primary particles was calculated from the PSDs of the heat-treated samples (Figure 6-21), showing that the size increase is roughly twofold compared to the as-synthesized samples (Figure 6-17).

In addition to TEM, the XRD data of both as-synthesized and heat-treated samples were analyzed by Rietveld refinements to extract the crystallite size values for the main phases. For the heat-treated BTO sample, the tetragonal and hexagonal phases (ICSD 99737 and ICSD 164386, respectively) were introduced to ensure stability of the refinements and provide a better match between the observed and calculated profiles, as was described in Chapter 6.1.1. For BSTO-50 and STO only the cubic phase was introduced, since it is the only expected phase for these materials. Refinement outputs for all samples are presented in Figure 6-22.

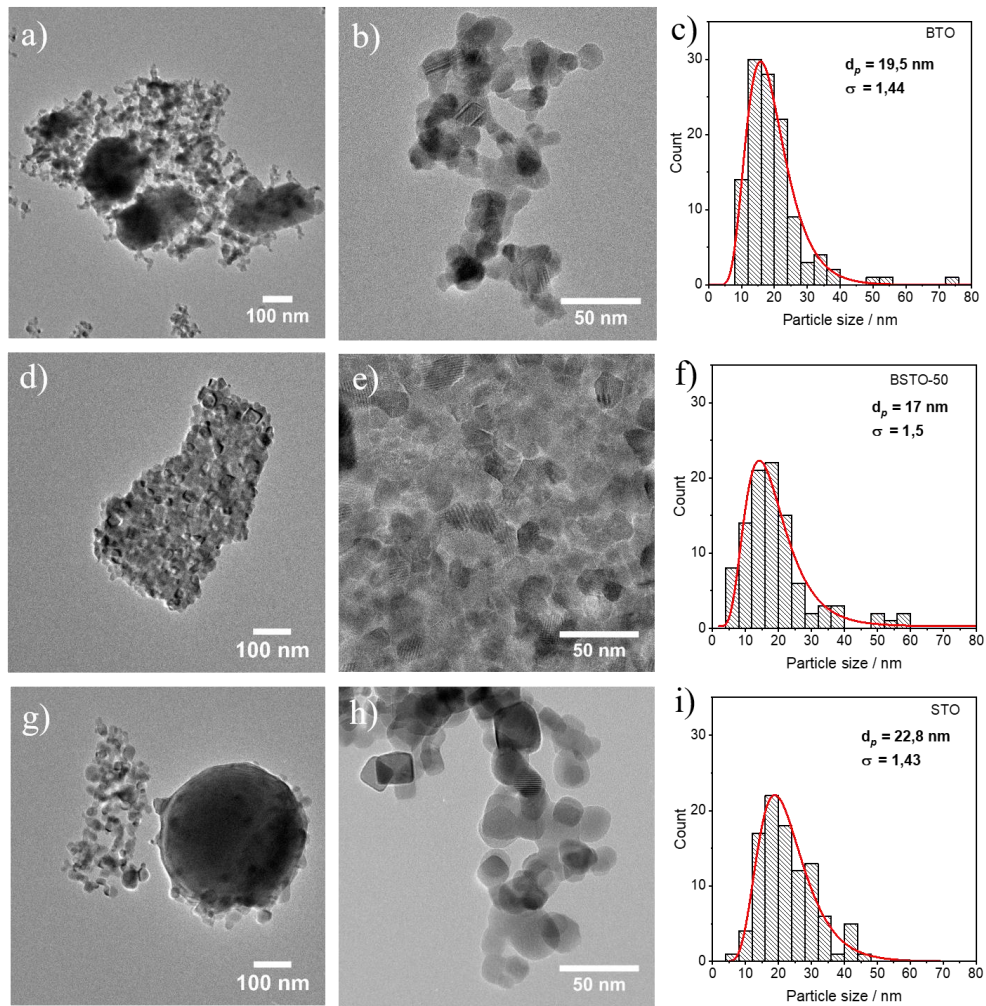


Figure 6-21. TEM images of heat-treated BTO (a, b), BSTO-50 (d, e) and STO (g, h) samples with corresponding PSD patterns (c, f, and i).

The particle sizes obtained from the PSDs from TEM of the as-synthesized powders are 11.2, 9.3, 8.3 nm for BTO, BSTO-50, and STO respectively. The value slightly decreases with increasing Sr concentration towards pure SrTiO₃ composition. This is expected as the cell unit of SrTiO₃ is smaller than that of BaTiO₃ because of the smaller ionic radius of Sr, therefore the expected decrease in the particle size, as was shown by Dunne *et al.* [25]. The calculated values from XRD are ~35, 32, and 80 nm (for BTO, BSTO-50, and STO, respectively) contradict the sizes from TEM. Such inconsistency would point at the existence of large particles alongside small ones, which is typically indicative of bimodal size distribution and can be expected in an SFS process, as was discussed in Chapter 6.1.1 [40, 51].

Table 6-8. Phase ratios obtained from XRD and SSA values from BET of as-synthesized (AS) and heat-treated (HT) BTO, BSTO-50, and STO powders.

Sample	XRD crystallite size / nm		TEM particle size / nm	
	AS	HT	AS	HT
BTO	33	49	11.2	19.5
BSTO-50	32	38	9.3	17
STO	80	100	8.3	22.8

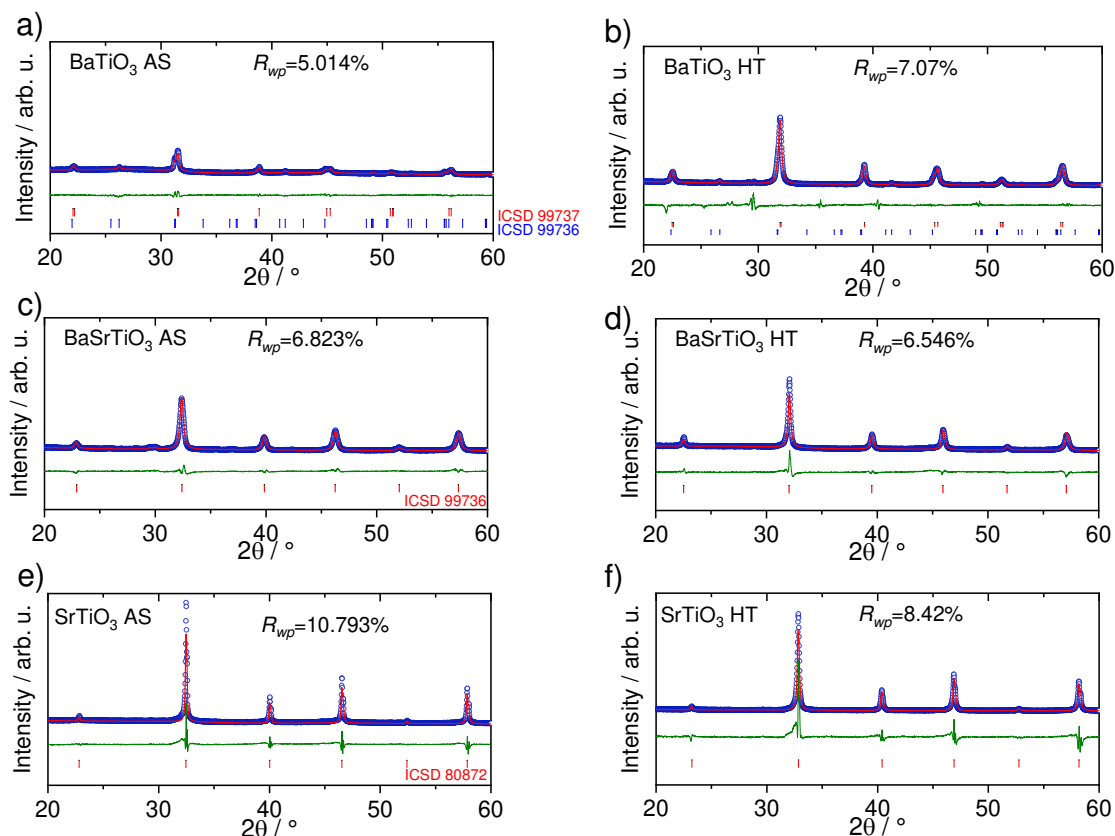


Figure 6-22. Graphical output from Rietveld refinements for as-synthesized (a) BTO, (c) BSTO-50, (e) STO, and heat-treated (b) BTO, (d) BSTO-50, (f) STO.

Briefly, the use of alcohols as solvents can lead to the formation of submicron particles due to the precursor precipitation on the droplet surface promoted by low boiling point of the used solvents, which therefore leads to the particle formation via the undesired droplet-to-particle conversion route [38, 144]. This claim is especially well-presented in the case of the STO sample demonstrated by the TEM image in Figure 6-17f, which shows that primary particles with the sizes around 10 nm can co-exist with much larger particles (~200 nm). A larger crystallite size for STO is therefore expected, which correlates with the initially high crystallinity of the sample observed in XRD (Figure 6-14).

After heat-treatment, the particle size did not increase substantially, as suggested by both XRD and TEM. The extracted values from XRD are 49, 38, and 100 nm for BTO, BSTO-50, and STO samples, respectively. They are in agreement with the acquired XRD patterns, indicating that the heat-treated BTO sample demonstrates a larger crystallite size compared to the BSTO-50 sample inferred from the higher peak intensity of the former (Figure 6-14). The calcined STO sample again shows the highest

crystallite size value among all samples, indicated by the high reflection intensity in XRD. TEM images show increased agglomeration and the average particle size increased upon heating, and small particles coexist with some much larger ones (Figure 6-21).

The applicability of BET measurements to assess the SSA of the flame-synthesized samples was questionable after the powders showed a substantial weight loss upon heating (20–24% depending on the sample) due to elimination of organic moieties from the surface. The existence of various adsorbates influences the density of the powders, which is needed for proper surface area and particle-size calculations, which therefore can lead to biased BET results. The SSA measurements were performed on a test basis on the as-synthesized BTO and heat-treated powders at 400 and 800°C for 3 hours. An additional heat-treatment step at 400°C should help to account for the exothermic feature and weight loss observed in TGA at the mentioned temperature (Figure 6-18). The density value was chosen 6.02 g/cm³, which corresponds to the bulk density of BaTiO₃. The samples were outgassed overnight at 200°C prior to analysis. The measured SSA values were 29.9, 6.7, and 4.1 m²/g and the corresponding calculated particle sizes using Equation 5-16 are 33, 144, and 243 nm for the as-synthesized, heat-treated powders (400 and 800°C), respectively. The values for heat-treated powders are in contrast with those obtained from XRD and TEM. Moreover, repeated BET measurements of the as-synthesized powders tended to yield inconsistent SSA values. Thus, BET measurements were not considered further in this study.

In conclusion, the feasibility of producing a wide range of Sr-substituted BaTiO₃ nanoparticles via an SFS process was demonstrated. The as-synthesized BaTiO₃ sample was shown to have the tetragonal and hexagonal phases. With a Sr concentration of 20%, the phase composition of the pristine powders showed much less amount of the hexagonal phase, and further increasing Sr concentration resulted in the complete absence of the hexagonal phase and stabilization of the cubic phase towards pure SrTiO₃. The crystallinity of the powders also benefited from the introduction of Sr, which increased with increasing Sr concentration. Primary particle sizes of the pristine powders shown by TEM are around 10 nm, and they co-exist with some much larger ones in the sub-micrometer range. The larger particles provide a major contribution to the high intensity reflections in XRD patterns, therefore suggesting a bimodal particle size distribution in the samples. This fact shows that the SFS process primarily leads to the formation not only of small nanoparticles, but also of some significantly larger ones. One particular issue that was observed in the present and previous experiments is the surface contamination with carbonaceous moieties. For this reason, a subsequent heat-treatment (800°C, 3 hours in oxygen) was applied to the powders to clean the surface. This resulted on one hand in a cleaner surface and on the other hand in an expected particle size increase. The increase in the particle size was accompanied by powder agglomeration and sintering as was illustrated by TEM images. Crystallite values extracted from XRD patterns of the heat-treated samples additionally confirmed particle growth.

6.3 Photocatalytic water splitting of $\text{Ba}_{1-x}\text{Sr}_x\text{TiO}_3$ nanoparticles

Photocatalytic performance of $\text{Ba}_{1-x}\text{Sr}_x\text{TiO}_3$ (BST) powders was examined regarding hydrogen production in water splitting reaction under UV light. An outline of the setup that was used for the measurements is first provided, and the results are then discussed.

6.3.1 Photocatalytic reactor setup

Photocatalytic hydrogen generation was investigated in an inner irradiation type photoreactor described by Grewe *et al.* [197, 198]. The setup is shown in Figure 6-23. The tests were conducted as follows: 50 mg of the photocatalysts were dispersed and sonicated in a mixture of methanol (Sigma-Aldrich, >99.8 %) and distilled water (10 vol.% of methanol in 200 ml). Methanol was used as a sacrificial agent to enhance the hydrogen production rate as described in Chapter 3. For photocatalytic tests, the dispersions were illuminated with a 150 W medium-pressure mercury lamp (TQ 150) while continuously stirred (850 rpm). The reaction chamber was constantly purged with an argon flow of 50 ml/min to carry the reaction products (H_2 , O_2 , and CO_2) directly into the X-STREAM gas analyzer from Emerson for their quantitative analysis. The temperature of the reactor was held constant at 20°C throughout the experiment. Six BST powders were tested in total: Three as-synthesized samples with $x = 0, 0.5$, and 1, as well as their heat-treated at 800°C analogues. The heat-treated powders were examined to see if the surface-cleaning effect provided by calcination affects the measured catalytic activity. On the contrary, the observed particle sizes increase on heating, which leads to fewer surface sites and therefore to a decrease in catalytic activity.

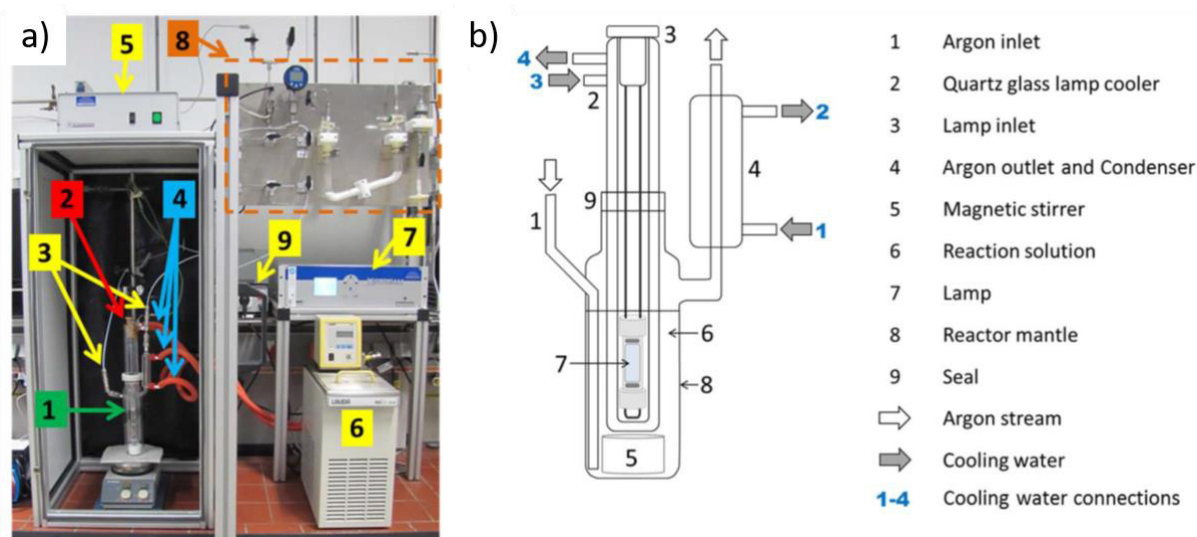


Figure 6-23. Overview of the photocatalytic setup for water splitting: a) the reactor is placed in a casing, which is kept closed during the operation of the photoreactor. The UV-light photoreactor (1) equipped with an inner irradiation lamp (2), gas connections (3) and connections for cooling water (4). Power supply for the UV-lamp (5), cryostat (6) used for providing cooling water, gas analyzer (7), which is connected to the control panel (8). The control panel is located above the gas analyzer, and the thermo-switch (9) is located between the gas analyzer and the casing; b) detailed schematics of the quartz-glass reactor (Courtesy of AG Tüysüz, Max-Planck-Institut für Kohlenforschung).

6.3.2 Photocatalytic tests and discussion

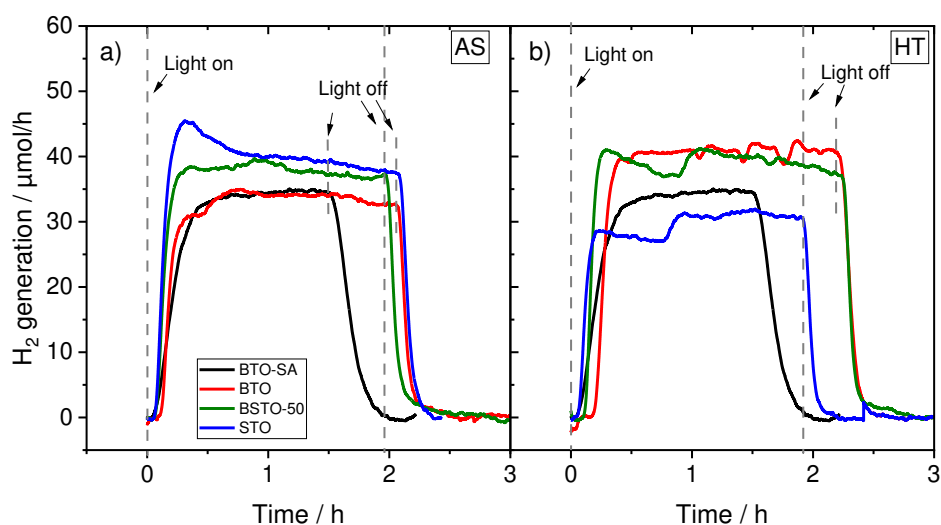


Figure 6-24. Results of catalytic tests of (a) as-synthesized (AS) and (b) heat-treated (HT) $\text{Ba}_{1-x}\text{Sr}_x\text{TiO}_3$ powders. Commercial BaTiO_3 (BTO-SA) is shown for comparison.

The photocatalytic performance of the as-synthesized and calcined samples was tested and compared with a commercially available BaTiO_3 powder synthesized by a sol-gel method (Sigma-Aldrich, SSA value $11,1 \text{ m}^2/\text{g}$, the equivalent BET particle size $\sim 100 \text{ nm}$, TEM image in Figure. Appendix 1, further referred to as BTO-SA). H_2 evolution was measured using methanol as a sacrificial agent as described above.

Hydrogen evolution of the pristine samples starts immediately after illuminating them with UV light (Figure 6-24a). Surprisingly, all three materials show similar activity per mass and – more surprisingly – even the surface contamination with carbonaceous species as identified from FT-IR and STA measurements does not seem to affect the photocatalysis results. In comparison to the commercial BTO-SA powder, the activities are similar or slightly higher and may be related to the lower particle sizes of the as-synthesized powders. However, the variations in hydrogen evolution are marginal and most probably are within the uncertainties of the measurement setup and do not allow for a conclusive comparison between the factors that might influence the measured catalytic activity. It is also difficult to draw conclusions regarding the effect of the hexagonal phase of BaTiO_3 on catalytic activity, but seemingly its presence has no negative impact on the performance.

The results of hydrogen evolution of the heat-treated samples are given in Figure 6-24b. The direct comparison of both, pristine and annealed materials does not show any significant change in activity. It can be discussed whether surface contamination and reduced specific surface suggested by higher particle sizes and agglomeration/sintering might compensate each other. The results suggest that the photocatalytic activity of $\text{Ba}_{1-x}\text{Sr}_x\text{TiO}_3$ nanoparticles in the size regime investigated here is rather limited by surface contamination for the as-synthesized samples and the increase of the particle size in the case of the heat-treated powders. It is an unexpected result that calcined powders practically do not lose their catalytic activity after heating. The present results are in contrast with the measurements conducted by Alammar *et al.*, who showed that heat-treating SrTiO_3 at 700°C resulted in a more than twofold decrease in the catalytic activity compared to the as-synthesized powders [19].

Despite the observed similarity in the results, the SFS-produced $\text{Ba}_{1-x}\text{Sr}_x\text{TiO}_3$ powders were shown to be catalytically active in the water splitting reaction. Heat-treatment of the as-synthesized provides a cleaning effect for the surface and leads to a substantial particle size increase but does not necessarily result in reduced catalytic activity.

6.4 Synthesis of $\text{BaTi}_{1-x}\text{Zr}_x\text{O}_3$ nanoparticles

Zr-substituted BaTiO_3 (further referred to as BTZ) is of potential interest for energy storage applications, particularly in capacitors, as was discussed in Chapter 3.2.3. A trend that is constantly exploited at present is the active miniaturization of the energy storage components by using ceramics with nanoscale dimensionality, which would allow for higher volumetric efficiencies and therefore better energy storage characteristics than capacitors based on micrometer and sub-micrometer particles [15, 137, 199]. The goal of the current chapter is to investigate the synthesis of BTZ nanoparticles using the SFS technique towards capacitive energy storage applications. The present study offers a new angle of view on the synthesis of nanocrystalline BTZ ceramics using a spray combustion method, which has not been reported on previously in the literature.

For the synthesis of BTZ powders all process parameters were adapted from the previous studies, the metal precursor concentration remained unchanged and was set at 0.2 M. A suitable Zr precursor was picked – zirconium propoxide (ZIP, $\text{Zr}(\text{OCH}_2\text{CH}_2\text{CH}_3)_4$, Alfa-Aesar, boiling point 207°C) because it is similar in handling to TTIP. The compositional range of $\text{BaTi}_{1-x}\text{Zr}_x\text{O}_3$ powders was selected in such a manner to be able to track any potential phase changes associated with changes in the ferroelectric characteristics, which occur over the 0–20 mol% Zr concentration range, as discussed in chapter 2.4. Process parameters are presented in Table 6-9 and the composition of the synthesized materials is shown in Table 6-10.

Table 6-9. Process parameters during the synthesis $\text{BaTi}_{1-x}\text{Zr}_x\text{O}_3$ powders.

Precursor solution flow / (ml/min)	CH_4 , pilot flame / slm	O_2 , pilot flame / slm	O_2 dispersion gas / slm	Compressed air sheath / slm	Pressure / mbar
3	2	1	6	300	950

Table 6-10. List of the synthesized $\text{BaTi}_{1-x}\text{Zr}_x\text{O}_3$ compositions.

Sample	Intended composition
BTO	BaTiO_3
BTZ-05	$\text{BaTi}_{0.95}\text{Zr}_{0.05}\text{O}_3$
BTZ-10	$\text{BaTi}_{0.90}\text{Zr}_{0.10}\text{O}_3$
BTZ-15	$\text{BaTi}_{0.85}\text{Zr}_{0.15}\text{O}_3$
BTZ-20	$\text{BaTi}_{0.80}\text{Zr}_{0.20}\text{O}_3$

The as-synthesized powders were collected from the filters and characterized in a similar fashion as described in the preceding chapters. Detailed description of the dielectric setup and the test results are given in Chapter 6.5.

6.4.1 Characterization of as-synthesized $\text{BaTi}_{1-x}\text{Zr}_x\text{O}_3$ powders.

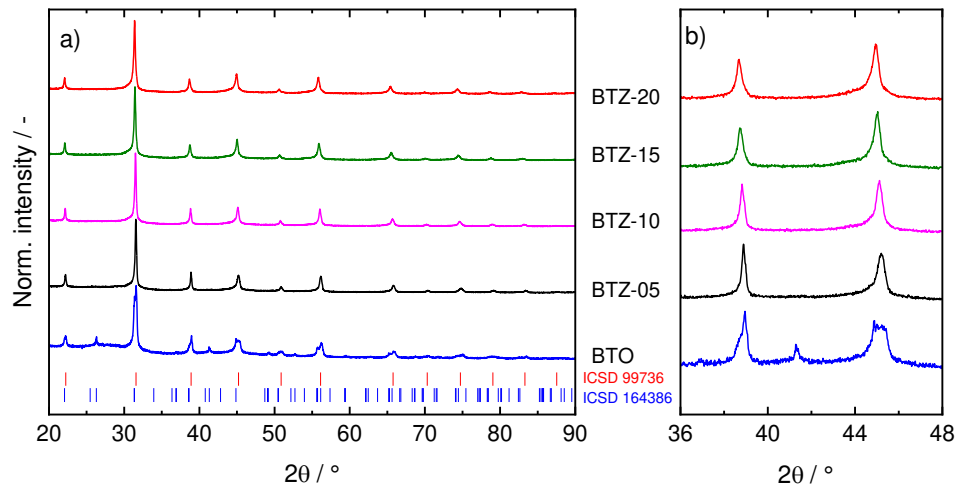


Figure 6-25. XRD patterns of (a) as-synthesized BTZ powders and details (b) of the $2\theta = 36\text{--}48^\circ$ region; tick marks indicate the peak positions of the cubic (red) and hexagonal (blue) phases of BaTiO_3 [152].

The phase composition of as-synthesized BTZ powders was studied using XRD, and the respective patterns are presented in Figure 6-25. For the pure BaTiO_3 sample the observed reflections indicate the existence of the cubic phase with a minor amount of the hexagonal phase (shown as blue tick marks in Figure 6-25). The latter is said to form above 1200°C and is usually observed due to thermal quenching [56, 177, 179]. Thermal quenching in our case is provided by the cooling cone (Figure 4-2), resulting in a steep temperature gradient on exiting the reactor zone. It cannot be inferred from the graph if the tetragonal phase of BaTiO_3 is also present in the sample, which is usually noticeable by the characteristic peak splitting of the (002) and (200) signals at 45° [89].

On introducing 5 mol% of Zr no contributions of the hexagonal phase could be detected. Consulting the phase diagram for BTZ powders for various Zr concentrations provided in [89, 200], at room temperature one should expect an orthorhombic phase at $x = 0.05$ and a rhombohedral phase at $x = 0.1\text{--}0.15$, respectively [89]. At $x = 0.2$ the phase composition is said to be dominated by a cubic crystal system, though in some cases a rhombohedral phase alongside cubic was suggested [95, 201, 202]. The differences between the orthorhombic and rhombohedral phases in XRD are minimal, which results in marginally different diffraction patterns, and therefore ambiguous phase analysis based on XRD data, since the phases cannot be resolved well. However, on closer inspection intensity variations of some signals relative to each other can be observed (e.g., at ~ 39 and 45°), which indicate a phase transition from one crystal structure to another [89, 201-203]. Common for all substituted samples with Zr is a shift towards smaller 2θ angles, which is caused by the expansion of the unit cell owing to the fact that Zr atoms have a larger ionic radius (0.72 \AA) than Ti atoms (0.605 \AA) [89, 142]. It should be pointed out that no peaks related to BaCO_3 (typically at $2\theta \sim 25\text{--}26^\circ$ [25, 90]) were found in the as-synthesized samples.

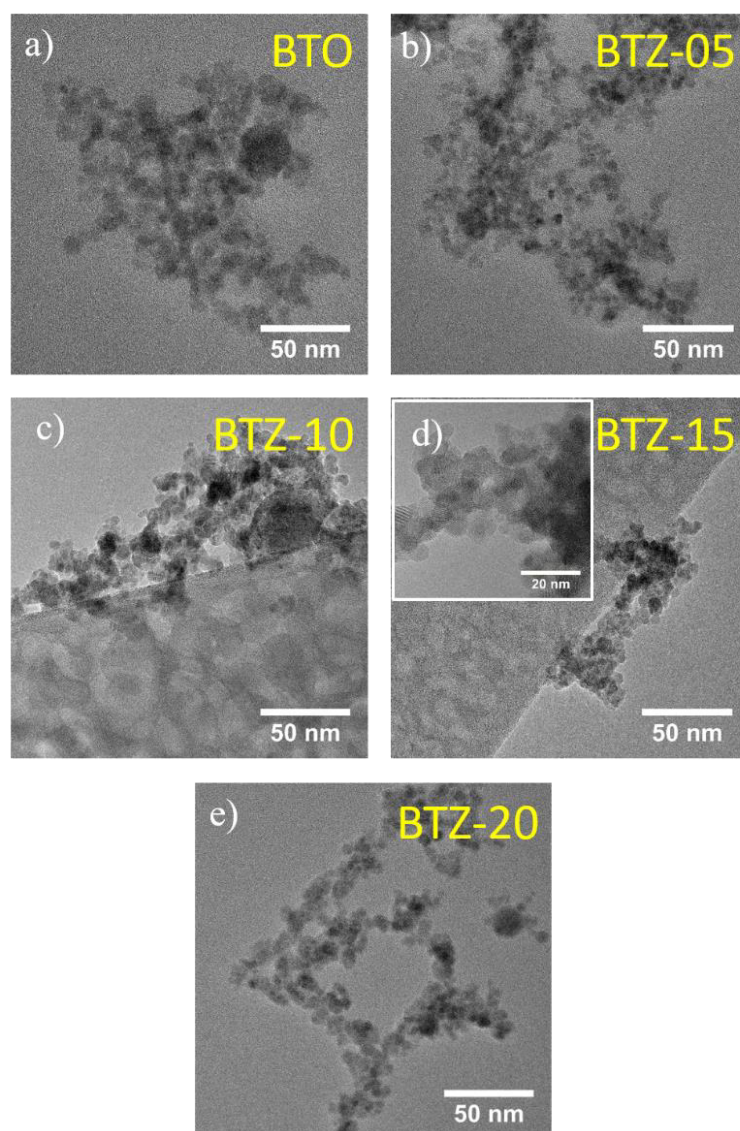


Figure 6-26. TEM images of as-synthesized $\text{BaTi}_{1-x}\text{Zr}_x\text{O}_3$ powders: BTO (a), BTZ-05 (b), BTZ-10 (c), BTZ-15 (d), and BTZ-20 (e) [152].

Particle size and morphology of the as-synthesized powders were examined by TEM. From the images in Figure 6-26 it is evident that the pristine powders predominantly consist of small mostly spherical and fairly agglomerated particles with sizes on average around 10 nm, though larger particles are also common to the samples, as can be clearly seen in Figure 6-26a for the BTO sample. The small particle sizes confirmed by TEM are favorable for further powder compaction and sintering in order to produce dense materials.

Additional FTIR and TGA measurements were performed to study the surface and stability of the as-synthesized powders, as flame-prepared powders tend to have adsorbed organics on the surface [51, 59]. The FTIR spectra of the as-synthesized powders (Figure 6-27) show that the powders are contaminated with various organic groups with the most prominent of them being carboxylate and carbonyl groups [28]. Carboxylate species form a chemical bond with metals and therefore give rise to two characteristic $\nu_s(\text{COO}^-)$ symmetric and $\nu_{as}(\text{COO}^-)$ asymmetric stretching vibrations at 1414 and 1537 cm^{-1} in the bridging bidentate configuration, as described in Refs. [28, 59, 182-184] and observed in the present study. Adsorbed hydroxyl groups were spotted over the $3000\text{--}3600\text{ cm}^{-1}$ range, which is expected, since

water is one of the major reaction products of methane combustion. Overall, the FTIR measurements repeat the previous observations made for BaTiO_3 and $\text{Ba}_{1-x}\text{Sr}_x\text{TiO}_3$ (Figure 6-10 and Figure 6-16).

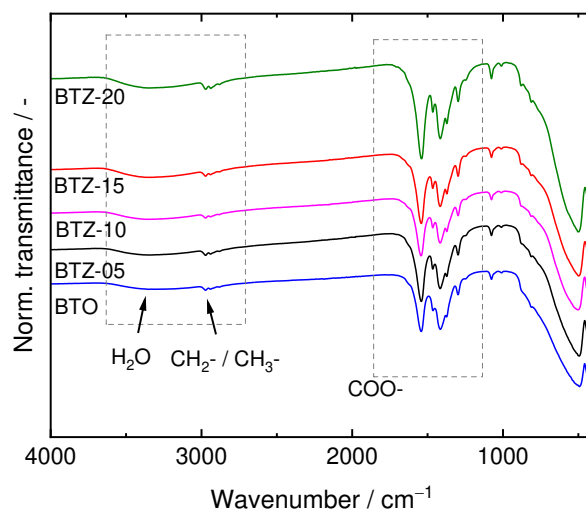


Figure 6-27. ATR-FTIR spectra of as-synthesized BTO, BTZ-05, BTZ-10, BTZ-15, and BTZ-20 powders.

The TGA data in Figure 6-28 show that all samples on average sustain a weight loss of 12–14% on heating to 1000°C , the largest portion of which was attributed to the removal of CO_2 and H_2O of the residual organics accompanied by the formation of an intermediate oxycarbonate $\text{Ba}_2\text{Ti}_2\text{O}_3\text{CO}_3$ phase over $400\text{--}600^\circ\text{C}$, which is consistent with the observations in literature [29, 170, 186] and previous observations made in this work (e.g., Figure 6-18 and Figure 6-4). Above 800°C no significant weight loss or thermal events were noticed.

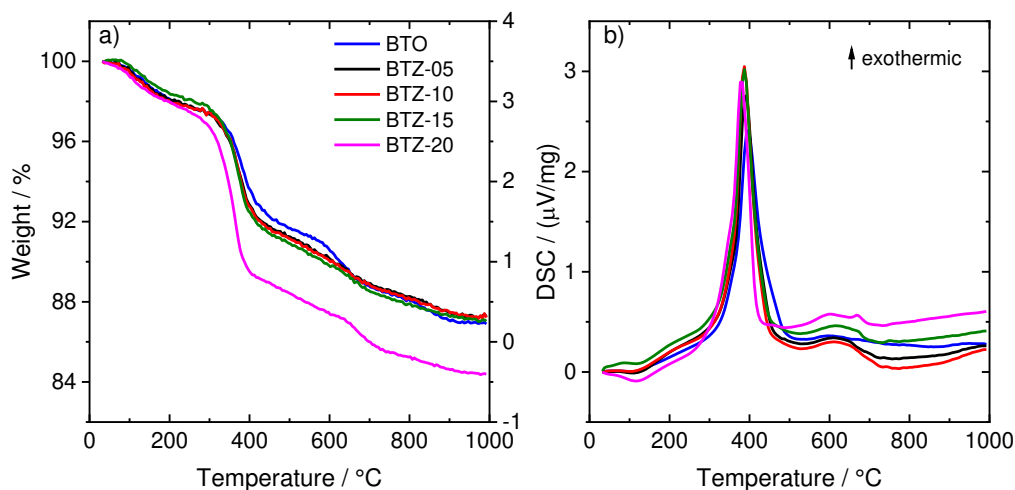


Figure 6-28. TGA (a) and DSC (b) data of as-synthesized BTO, BTZ-05, BTZ-10, BTZ-15, and BTZ-20 samples in air heat-treated at $20^\circ\text{C}/\text{min}$ to 1000°C .

6.4.2 Powder compaction and sintering

After initial powder characterization, the as-synthesized powders were subjected to compaction and calcination. Prior to compacting, the powders were pre-heated at 800°C for 1 h according to TGA to reduce the amount of organic contaminations discovered in FTIR in the samples (Figure 6-27). After that, the

pre-heated powders were mixed with a binder agent (PVA solution, 4%). To increase viscosity of the prepared slurry, it was left in a furnace at 100°C for 30 min. Then the dried slurries were put into a stainless steel die with a diameter of 13 mm and pressed at an applied force of 90 kN for 30 minutes. The as-prepared pellets (~0.6–0.7 mm thick) were then collected and sintered at 1100°C for three hours in oxygen in a Carbolite E3216 furnace. The selected sintering temperature and time regime were chosen to avoid significant particle size growth as is the case when higher temperatures (typically 1200–1500°C) and prolonged calcination times are used [202, 204]. After calcination, the density of the sintered pellets was measured using a pycnometer, as described in [141]. The prepared pellets were examined by XRD and Raman to check the phase composition after calcination. In addition, uncompacted as-synthesized powders were separately heated at 1100°C for 3 h to allow for TEM and FTIR measurements to study particle surface and size growth. Prior to dielectric tests, the pellets were sputtered with gold and additionally examined in SEM to study the surface morphology.

6.4.3 Characterization of sintered $\text{BaTi}_{1-x}\text{Zr}_x\text{O}_3$ pellets.

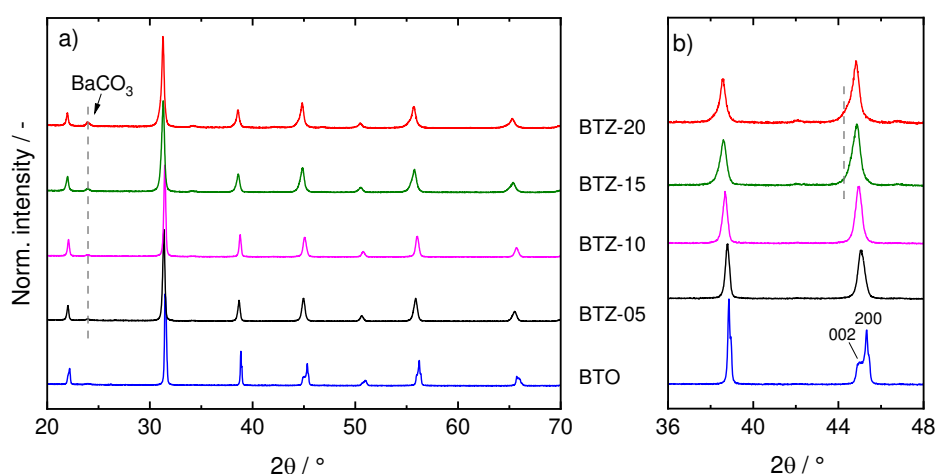


Figure 6-29. XRD patterns of (a) sintered BTZ pellets and details (b) of the $2\theta = 36\text{--}48^\circ$ range; dashed line in the right graph shows an additional contribution to the left of the main peaks in BTZ-15 and BTZ-20 [152].

XRD patterns of the sintered pellets are presented Figure 6-29. The pure BaTiO_3 sample shows no contributions that can be attributed to the hexagonal phase, whereas other samples demonstrate no transformations compared to the as-synthesized powders. The BTO sample also shows the characteristic peak splitting at 45° , which marks the development of the tetragonal phase upon calcination [10, 134]. Common to all samples is the increased crystallinity witnessed by sharper peaks and much flatter background.

For $x = 0.05, 0.1, 0.15,$ and 0.2 the situation is analogous to that of the as-synthesized powders with the distortion of the parent cubic phase present being virtually indistinct. However, on closer inspection of the reflections at $\sim 38^\circ$ and 45° (Figure 6-29b) a slight perceptible difference in the reflection intensities can be observed. In BTZ-05 the intensity of the former is slightly higher than that of the latter with no visible peak splitting at 45° , which marks the development of the orthorhombic phase in this sample [94, 201]. The situation changes for $x = 0.1, 0.15,$ and 0.2 , where now the reflection at 38° has a lower intensity than the one at 45° . This barely perceptible change marks a phase transition from the orthorhombic to the rhombohedral phase [94]. However, Deluca *et al.* observed that at $x = 0.15$ the rhombohedral phase coexists with a small amount of cubic phase [202]. For both $x = 0.15$ and 0.2 the recorded

reflections appear broader (marked with a dashed line in Figure 6-29b) with some asymmetry compared to the samples with lower Zr concentrations, which might indicate the coexistence of the cubic and rhombohedral phases as discussed by Buscaglia *et al.* [95]. In addition, on closer inspection a peak at 24° is visible, which signifies the presence of a small amount of BaCO_3 in the pellets.

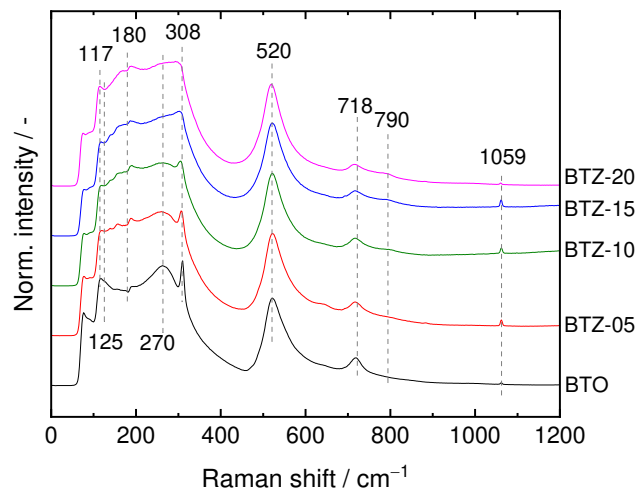


Figure 6-30. Raman spectra of BTZ pellets sintered at 1100°C . Dashed lines indicate band positions of the most prominent features [152].

Raman analysis was employed to complement the picture rendered by XRD with the recorded spectra presented in Figure 6-30. Raman analysis on BTZ powders is often used to unveil small changes in structure that XRD cannot resolve [91, 94, 95, 142, 201, 202].

The pure BTO sample shows prominent features corresponding to the tetragonal phase (bands are at 308 and 718 cm^{-1}). The band at 520 cm^{-1} corresponds to Ti–O vibrations of the TiO_6 octahedra [95, 141]. A band at 180 cm^{-1} common to all displayed spectra is the anti-resonance feature observed for low-symmetry ferroelectric phases of BaTiO_3 [94, 95, 201]. With the introduction of Zr, the spectra reveal some significant changes, with the most prominent being the appearance of the feature at 125 cm^{-1} , which was attributed to the replacement of Ti atoms by Zr and is said to appear when two chemically different BO_6 octahedra types are present [95, 201]. Concurrently, the peak at 117 cm^{-1} related to Zr–O motion in BTZ ceramics emerges and its intensity increases with increasing Zr concentration [95]. Both features (117 and 125 cm^{-1}) at $x = 0.05$ suggest the orthorhombic phase in this sample. The distinctive tetragonal bands of pure BaTiO_3 at 308 and 718 cm^{-1} decrease in intensity while a broad band at $\sim 790\text{ cm}^{-1}$ arises with increasing Zr concentration, thus directly indicating incorporation of Zr into the BaTiO_3 lattice [95]. The intensity of the broad band at 270 cm^{-1} in the pure BTO sample weakens upon increasing Zr content, also indicating a phase transition towards the orthorhombic phase at $x = 0.05$ [94, 95, 202]. As mentioned earlier, according to literature [95] the dominant phase in BTZ-10 should be orthorhombic. Indeed, the Raman spectra of BTZ-05 and BTZ-10 are virtually identical. At $x = 0.15$ and 0.2 the feature at 308 cm^{-1} disappears completely, while that at 790 cm^{-1} becomes more prominent, which could be attributed to higher Zr incorporation into the BaTiO_3 lattice [95]. Furthermore, for BTZ-15 and BTZ-20 the mentioned features at 117 and 125 cm^{-1} become even more pronounced, therefore indicating the likely dominance of the rhombohedral crystal structure. In addition, a band at 1059 cm^{-1} is noticed for all samples regardless of the Zr concentration, which is indicative of carbonates and in agreement with XRD (Figure 6-29) and FTIR data (Figure 6-27) [177].

Rietveld refinement with the fundamental instrument approach was performed to extract crystallite sizes from the XRD data of the pellets, and the calculated sizes are plotted against Zr concentration (Figure 6-32). It should be mentioned that the refinement procedure is complicated for the current set of samples, as the problem is twofold: i) for some Zr concentrations no reliable structural information is available from the ICSD database; ii) the existence of multiple phases according to XRD (e.g., BTZ-15 and BTZ-20) can sometimes produce unstable or inconsistent results. Thus, for some compositions, data for more than one phase is presented (Figure 6-32), where an additional phase was introduced for a better XRD pattern description. The cubic phase of BaTiO_3 was fitted using ICSD 99736 entry, for the tetragonal phase ICSD 99737 was used, while the hexagonal phase was represented by ICSD 164386. The orthorhombic phase of BTZ was described by ICSD 291454, while no reliable structural information for the rhombohedral phase of BTZ was found. A structure similar to BTZ $\text{BaSn}_{0.1}\text{Ti}_{0.9}\text{O}_3$ (ICSD 244195) was taken as a starting point for the refinement in this case. Graphical outputs of Rietveld refinement are presented in Figure 6-31 with the results summarized in Table 6-11. Moreover, the theoretical density was estimated from the refinement results based on the phases introduced. The obtained values were then used to calculate relative density values for each sample. These results are also summarized in Table 6-11.

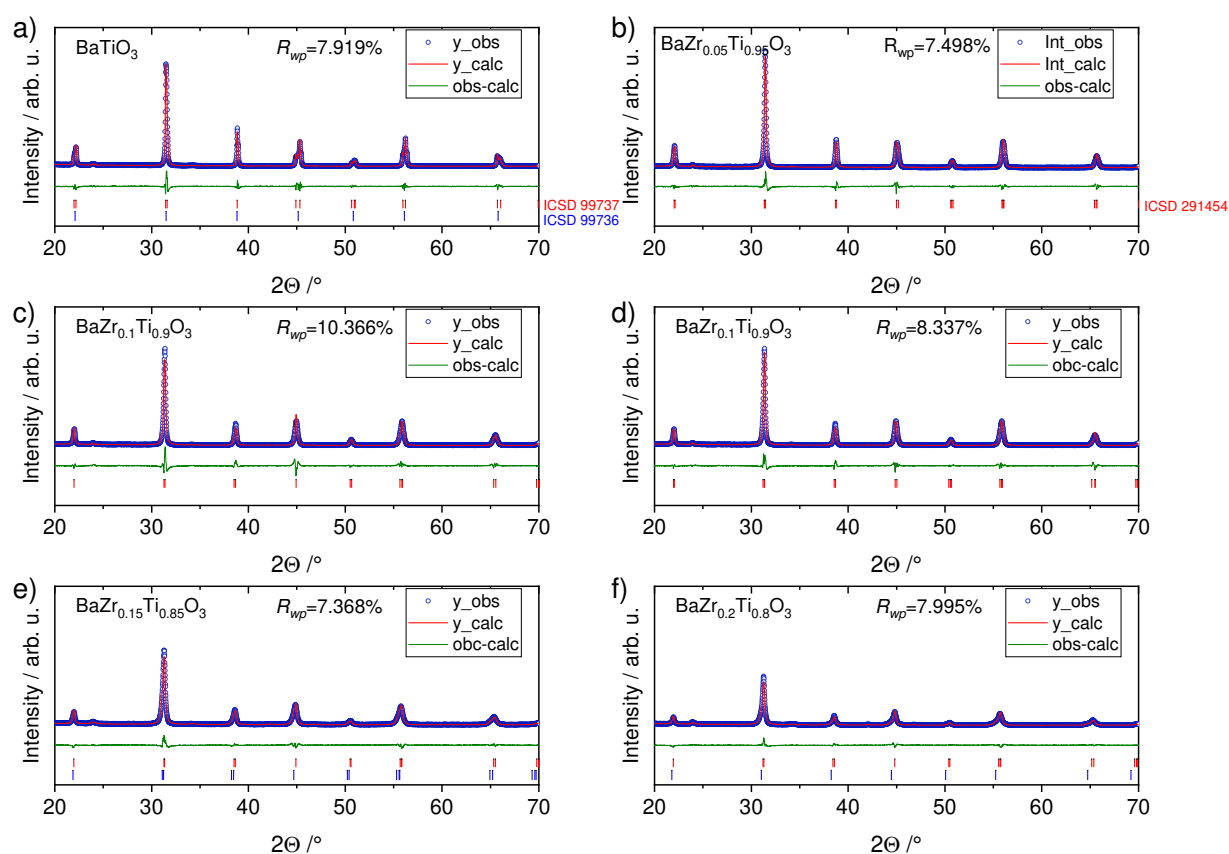


Figure 6-31. Result from Rietveld refinements for (a) BTO, (b) BTZ-05, (c, d) BTZ-10, (e) BTZ-15, and (f) BTZ-20 pellets.

To complement the picture from XRD, TEM analysis of the uncompressed powders separately heat-treated at 1100°C was carried out to visually demonstrate the particle size change after heating for all Zr concentrations. The corresponding TEM images are plotted together with the corresponding XRD values in Figure 6-32.

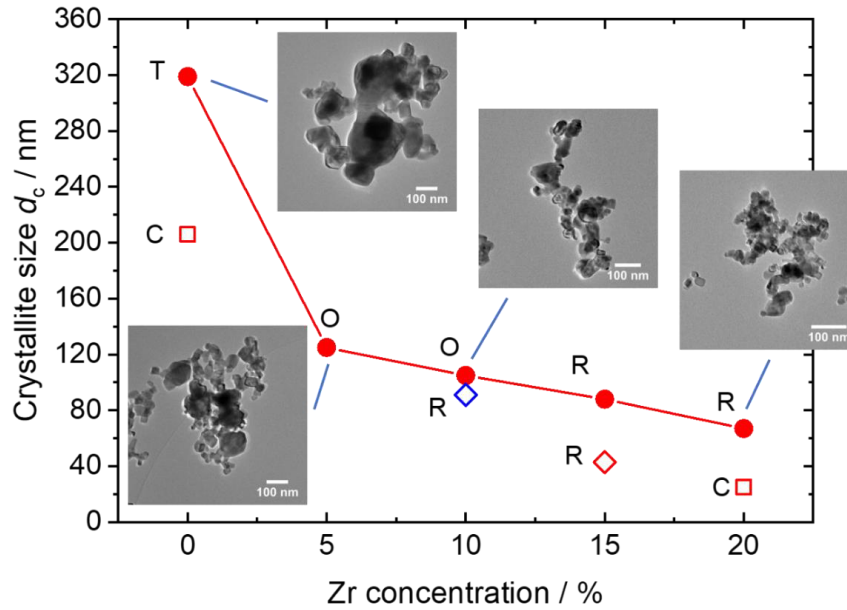


Figure 6-32. Comparison of particle (shown as TEM insets) and crystallite sizes versus Zr concentration obtained from TEM and XRD data for the $\text{BaTi}_{1-x}\text{Zr}_x\text{O}_3$ powders heat-treated at 1100°C and sintered pellets, respectively. Line between data points serve as guide-to-eye. The following abbreviations were used: T: tetragonal, C: cubic, O: orthorhombic, R: rhombohedral [152].

It can be seen from Figure 6-32 that according to the Rietveld-refined XRD data, smaller crystallite sizes are observed after calcination with increasing the Zr concentration. This fact is additionally supported by TEM (shown as insets in Figure 6-32) of the heat-treated powders, which demonstrate a noticeable particle size decrease for increasing Zr concentration. A similar case showing decreasing particle sizes with increasing Zr concentration was described by Philippot *et al.* for the hydrothermal synthesis of BTZ nanoparticles [31, 205]. The authors showed that increasing Zr content favors nucleation and thus impedes the overall crystal growth. Ihlefeld *et al.* [206] observed a similar trend in BTZ thin films deposited on copper – the observed grain sizes decreased with increasing Zr concentration. The authors attributed the effect to the increased nucleation rate of BTZ crystals, which therefore limits the final grain size. These observations correlate well with the present findings from both TEM and XRD. The calculated relative density values are on average $\sim 70\%$, which is not high but expected considering a very moderate sintering regime of 1100°C for three hours, which is significantly lower than typical temperature values in conventional sintering such as $1200\text{--}1500^\circ\text{C}$ [134, 199, 207]. Arguably, increasing temperatures while maintaining the same time schedule will lead to better densification and therefore higher relative densities. Morphology of sintered pellets was investigated using a Philips XL-20 scanning electron microscope (SEM), and the respective images are presented in Figure 6-33.

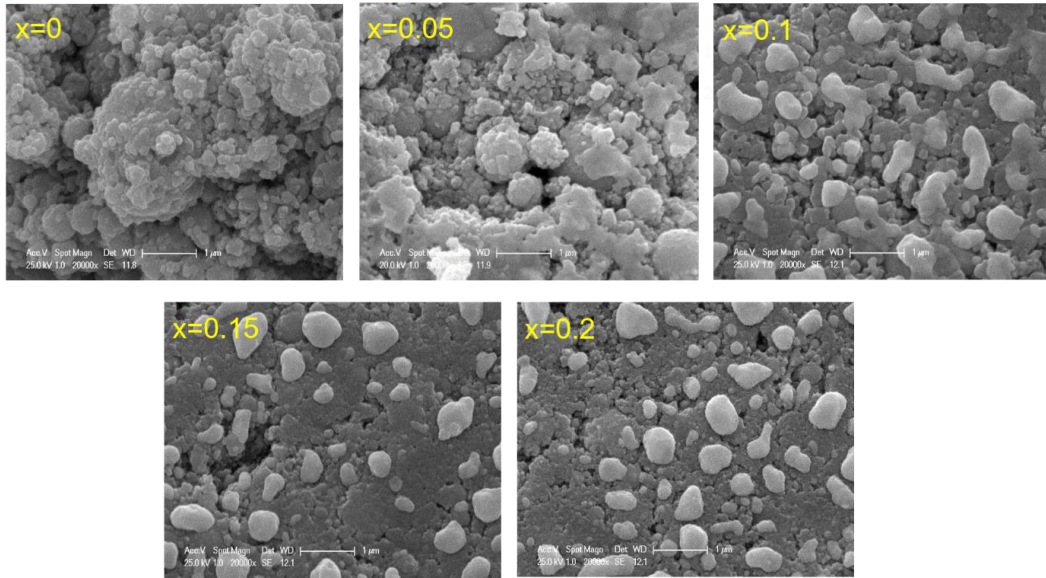


Figure 6-33. SEM images of sintered BTZ pellets. The scale bar in all images is 1 μm [152].

The images clearly indicate the presence of agglomerates and sintered particles of various sizes with small pores penetrating the entirety of the samples. The average grain size ranges from just a few tens of nanometers to 2 μm .

Table 6-11. Crystallite sizes, phase ratios, calculated relative density values, and goodness of fit (R_{wp}) values from the Rietveld fits of the calcined BTZ pellets. T, C, O, R stand for tetragonal, cubic, orthorhombic, and rhombohedral crystal systems, respectively.

Sample	Zr concentration x	Phases refined	Phase ratio	$d_{\text{crystallite}} / \text{nm}$	Relative density / %	$R_{wp} / \%$
BTO	0	T / C	68 / 32	319 / 206	76	7.78
BTZ-05	0.05	O	-	125	72	7.49
BTZ-10	0.1	R	-	91	72	10.37
		O	-	105	73	8.37
BTZ-15	0.15	R / R	51 / 49	88 / 43	69	7.37
BTZ-20	0.2	R / C	77 / 23	67 / 25	77	7.99

6.5 Dielectric measurements of $\text{BaTi}_{1-x}\text{Zr}_x\text{O}_3$ pellets

The temperature dependences of the dielectric constant were measured by an impedance analyzer (Solartron 1260) equipped with a dielectric interface 1296 over the 1 Hz–1 MHz frequency range and with an applied voltage of 100 mV. Gold electrodes were deposited on both sides of the sintered pellets. The temperature was controlled using a LakeShore 340 temperature controller. The impedance analyzer generates an AC signal with various frequencies that interacts with the sample to obtain complex impedance spectra, from which permittivity values can be derived [208]. The measurements setup is shown in Figure 6-34 and the results of dielectric measurements for BTO, BTZ-5, and BTZ-10 are presented in Figure 6-35, and for BTZ-15 and BTZ-20 in Figure 6-36.

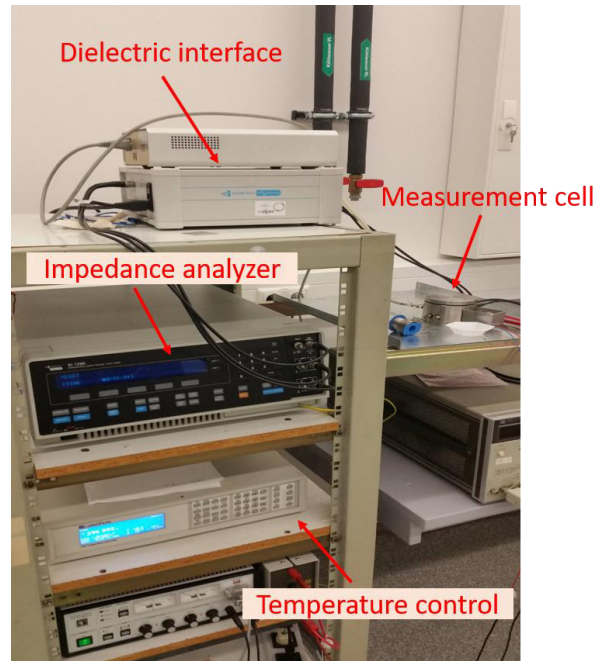


Figure 6-34. Overview of the setup for dielectric measurements on pellets with temperature control (Courtesy of AG Lupascu, Universität Duisburg-Essen).

For the pure BTO sample (Figure 6-35a) a typical behavior for BaTiO_3 is observed with a very distinct maximum at 395 K, which marks a phase transition from the ferroelectric tetragonal to the paraelectric cubic phase. A step-like anomaly seen around 300 K denotes the phase transition from the tetragonal to the orthorhombic structure. Both observed transition temperatures correlate well with the extensive literature on dielectric studies of BaTiO_3 [10, 131-134, 192]. The observed permittivity values are quite high for the sample ($\epsilon_{\text{max}} \approx 2000$) considering the nanoscale nature of the material as suggested by XRD and TEM. Loss tangent ($\tan \delta$) values (Figure 6-35b) are low in general but increase slightly with decreasing frequency, which is a sign of interfacial space charge polarization in the material (Maxwell-Wagner relaxation), whereby charge carriers are blocked at inner dielectric boundary layers, therefore leading to charge separation and an additional contribution to the overall polarization. This phenomenon emerges in materials with compositional inhomogeneities (defects, porosities, oxygen vacancies) and in fine-grained ceramics [133, 202].

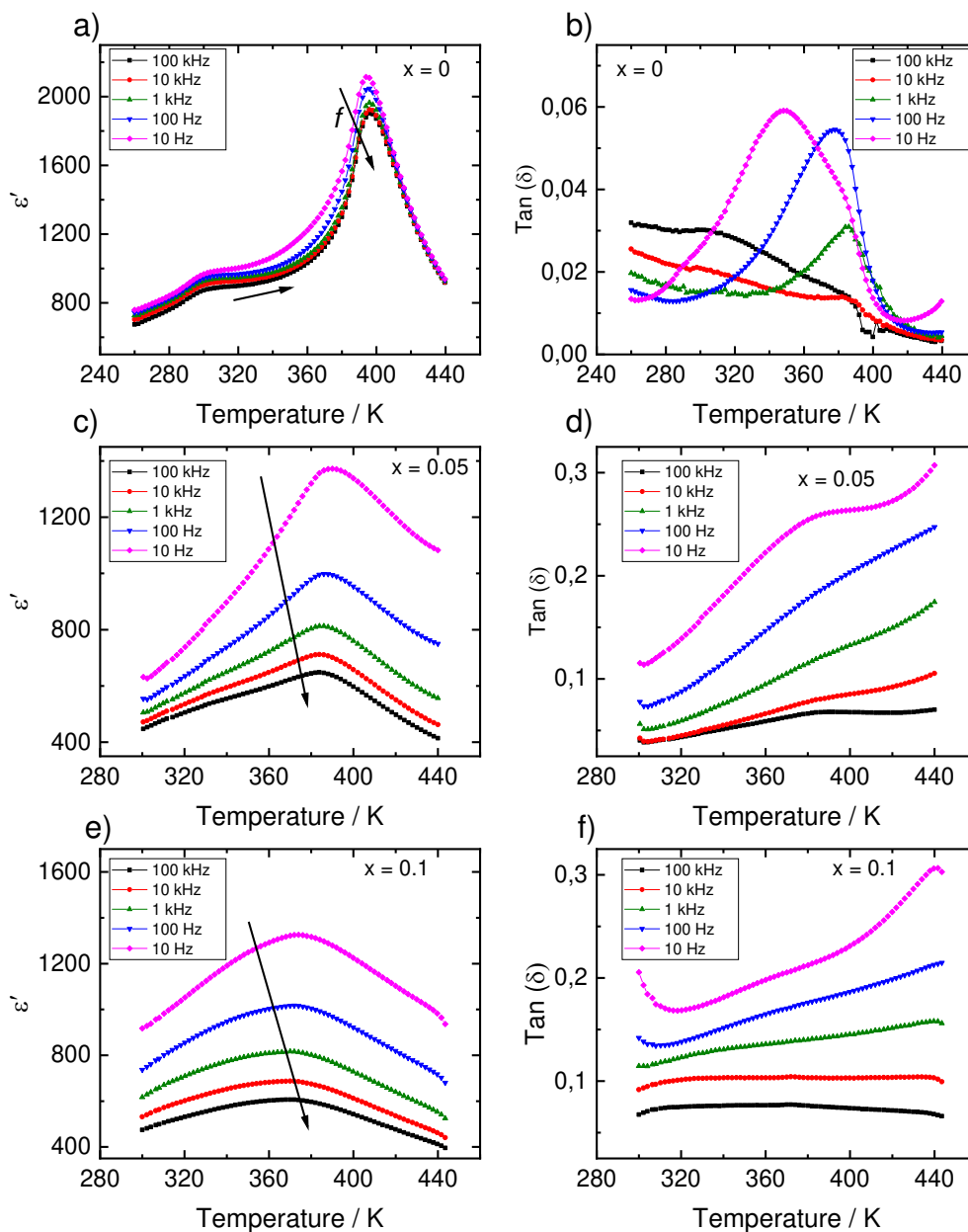


Figure 6-35. Temperature dependence of the dielectric permittivity (ϵ') and losses ($\tan \delta$) of the sintered $\text{BaTi}_{1-x}\text{Zr}_x\text{O}_3$ pellets: (a, b) $x = 0$; (c, d) $x = 0.05$; (e, f) $x = 0.1$. Adapted from [152].

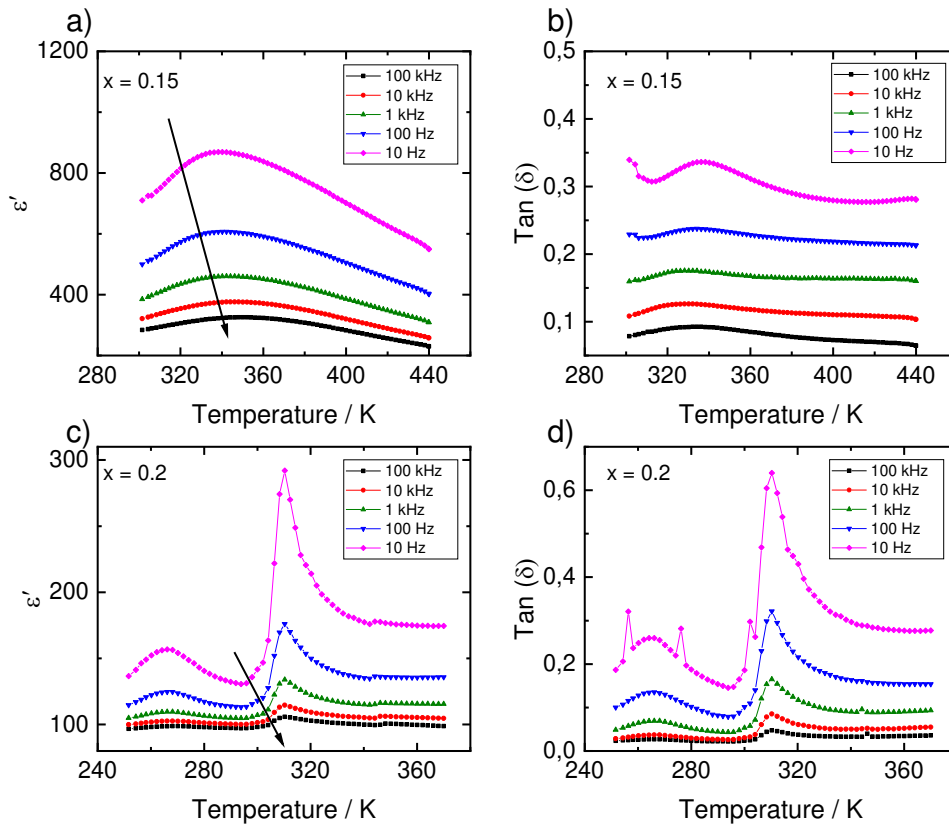


Figure 6-36. Temperature dependence of the dielectric permittivity (ϵ') and losses ($\tan \delta$) of the sintered $\text{BaTi}_{1-x}\text{Zr}_x\text{O}_3$ pellets: (a, b) $x = 0.15$; (c, d) $x = 0.2$. Adapted from [152].

On introducing and gradually increasing the Zr concentration, the dielectric maxima become less pronounced and broader, which is indicative of a diffuse phase transition and is in agreement with Ref. [202]. The maxima shift towards lower temperatures and the maximum permittivity values can be seen at 390, 370, 340 and 310 K for $x = 0.05, 0.1, 0.15,$ and $0.2,$ respectively (Figure 6-35c, e and Figure 6-36a, c). These data agree very well with the measurements by Miao *et al.* [94]. The common picture for all analyzed BTZ samples is that the observed permittivity values decline in general when compared to the pristine BaTiO_3 sample. The most important contribution to this is most probably caused by the decreasing grain sizes as shown by XRD and TEM, which is consistent with typical behavior of ferroelectrics on decreasing grain sizes [10, 133, 209, 210]. However, Ihlefeld *et al.* [206] showed that in thin BTZ films with the amount of Zr varying between 5 and 25 mol% the measured permittivity values were independent of the Zr concentration. The observed decline was attributed solely to grain size effects with the BTZ ceramics demonstrating smaller grain sizes and therefore lower permittivity values. However, it should be kept in mind that introduction of Zr disturbs the long-range ferroelectric order, which negatively affects the dielectric performance and can certainly be another contribution to the decreasing permittivity values in the current study. Moreover, in our Zr-containing samples the maxima become less pronounced and are accompanied by a strong frequency dispersion. Permittivity and loss tangent ($\tan \delta$) values increase dramatically with decreasing frequency (Figure 6-35 and Figure 6-36), which again indicates strong charge polarization effects. This might indeed be the case, since the samples demonstrated poor relative density values ($\sim 70\%$) and have crystallite size values on the order of 100 nm for the Zr concentrations $x \geq 0.05$. Besides, a possibility of defects such as oxygen vacancies should be also taken into account, as it might also contribute to the observed relaxation phenomena [133, 202,

204]. Arguably, repetitive annealing of the pellets at higher temperatures and longer times might lead to the disappearance of the strong frequency dispersion, as shown by Ciomaga *et al.* [204].

Interestingly, the BTZ-20 sample shows two distinct permittivity maxima (Figure 6-36c, d) at 310 and 260 K, which indicates the presence of two different phases of BTZ in this sample, as was also suggested by the XRD measurement (Figure 6-29). The position of the dielectric maximum suggests the presence of a BTZ phase with a higher Zr concentration towards $x = 0.25\text{--}0.3$ [94]. Relaxor behavior was not observed in any of the samples, as is expected considering the range of the investigated Zr concentrations, which is typically at $x > 0.25$ [92]. An overview graph of temperature dependences of the dielectric permittivity for all BTZ compositions at a fixed frequency of 100 kHz is shown in Figure 6-37 for a better representation of the performance of each individual sample across all Zr concentrations.

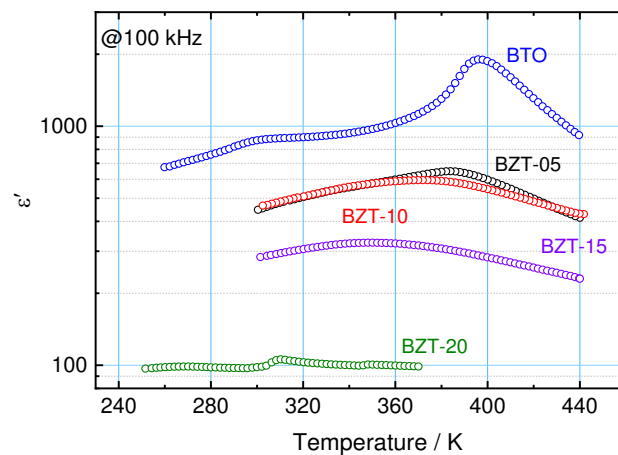


Figure 6-37. Dielectric permittivity (ϵ') versus temperature for all synthesized BTZ compositions at 100 kHz (observe the log scale) [152].

Overall, a successful synthesis of $\text{BaTi}_{1-x}\text{Zr}_x\text{O}_3$ powders via SFS with $x = 0\text{--}0.2$ was shown. The as-synthesized powders are characterized by small particle sizes as shown by TEM images. In the pure BaTiO_3 sample an additional hexagonal secondary phase was observed, which disappears on introducing Zr. For pellets sintered at 1100°C the crystallite size was found to decrease with increasing Zr concentration. At $x = 0$, the phase composition is a mixture of the tetragonal/cubic phases and at $x = 0.05$, only the orthorhombic phase is present. Compositions with higher Zr concentrations show coexistence of orthorhombic and rhombohedral phases. According to the dielectric measurements, the Curie temperature shifts towards lower temperatures with increasing Zr concentration. Moreover, a constant decrease in the dielectric permittivity values was observed, which was attributed to the decreasing crystallite/particle size. A strong frequency dispersion at lower frequencies observed for the Zr-containing samples was attributed to the Maxwell-Wagner relaxation that typically emerges in fine nanograined ceramics with structural inhomogeneities such as increased porosity. This is an adverse factor for promising energy storage densities. Debatably, higher sintering temperatures and longer annealing times should help to amend the issue. Overall, the present study proves that SFS can be used to produce fine nanopowders for dielectric applications.

7 Conclusions

In this thesis, the applicability of spray-flame synthesis (SFS) towards the production of BaTiO₃ nanopowders and their derivatives was investigated, which has not been done before in the existing literature. BaTiO₃-based perovskites such as Ba_xSr_{1-x}TiO₃ (BST) for catalytic and BaTi_{1-x}Zr_xO₃ (BTZ) for dielectric applications represent a series of technologically important materials, which are being increasingly explored in the course of the energy conversion and storage topic, where nanomaterials with outstanding performance characteristics are favored. New synthesis approaches for producing high-quality nanoscale powders additionally urged the need for a comprehensive research on the flame synthesis of such important materials as BaTiO₃ perovskites and related structures. Therefore, one of the main goals of the present work was to study the influence of solvents, precursors, and synthesis parameters for the SFS on the phase composition and morphology of BaTiO₃ nanopowders using a spray-flame reactor setup.

In preliminary experiments, a fixed solution composition (propionic acid/iso-propanol) was chosen while varying the precursor concentration (0.2–1 M) at constant process parameters. Additionally, an experiment with the addition to the mixture solution of a high-enthalpy solvent (xylene) was conducted to investigate whether this had any effect on the properties of the produced materials. As a result, in all experiments nanoscale powders were produced as investigated and confirmed by XRD, TEM, and BET measurements. An increase in the precursor concentration resulted in larger particle sizes, and the addition of xylene at a fixed precursor concentration also led to a measurable particle size increase. However, a few challenges were identified such as the emergence of the secondary hexagonal phase of BaTiO₃ and the abundant surface coverage with carbonaceous species, specifically barium acetate, as was shown by FTIR measurements.

Based on these results, a follow-up study regarding the extended solvent composition range including ethanol, acetic acid, and 2-ethylhexanoic acid was conducted to decrease the amount of the hexagonal phase and carbon contaminations. The conducted solvent study showed that the introduction of ethanol and acetic acid did not result in any significant changes and essentially reproduced the experiments with the initially proposed solvent composition (propionic acid / isopropanol). In contrast, the addition of 2-ethylhexanoic acid led to much more amorphous powders that showed a dramatic weight-loss on heating in STA experiments, which suggested a higher amount of carbonaceous species in these samples, acetates in particular. This fact requires additional investigations of the solvents. A post synthesis heat-treatment step at 800°C for three hours was applied to improve phase composition of the powders and their crystallinity and to possibly decrease and remove surface contamination with incompletely oxidized carbonaceous compounds. The heat-treated powders showed improvements in all the above-mentioned points while still staying in the nanometer range, as was shown by TEM.

One of the additional goals of the present work was to explore possibilities of a substitutional doping of BaTiO₃ during the SFS process. The Ba-site was substituted by Sr²⁺ and the Ti-site was substituted by Zr⁴⁺ atoms. This compositional modification should also provide a solution towards reducing the amount of the hexagonal phase in the as-synthesized powders. The powders were afterwards examined regarding their performance in hydrogen production in water splitting reaction (BST) and capacitive energy storage (BTZ). In the case of BST powders, with a Sr concentration of 20% a much less amount of the hexagonal phase was detected. By further increasing Sr concentration a complete absence of the hexagonal phase, and stabilization of the cubic phase towards pure SrTiO₃ was observed. The crystallinity of the powders increased concurrently with increasing Sr concentration. As-synthesized BST powders were

found to exhibit particle sizes around 10 nm (TEM) with some larger particles in the sub-micrometer range, which suggest a bimodal particle size distribution in these samples. After subsequent heat-treatment, an expected particle size increase was observed accompanied by powder agglomeration and sintering as was illustrated by TEM measurements. The catalytic performance of the as-synthesized and annealed at 800°C powders was then examined, and the results showed that both powder types show very similar catalytic activity. Most probably, the smaller particle size with a higher amount of carbonaceous moieties in the case of the as-synthesized powders is counterbalanced with the cleaner surface and larger particle sizes observed for the heat-treated powders.

Substitution of the Ti-site of BaTiO₃ with Zr was successfully performed and was shown to result in the powders composition without the hexagonal phase of BaTiO₃. With increasing Zr concentration a number of different phases was observed in the as-synthesized powders depending on the amount of Zr introduced. The as-synthesized powders are characterized by small particle sizes as was shown by TEM. In order to test the dielectric performance of the powders, pellets were pressed from the as-synthesized powders and then sintered at 1100°C for 3 h to avoid significant particle growth. Subsequent XRD and TEM measurements showed that the observed crystallite/particle size decreases with increasing Zr concentration, which is in accordance with the available literature on the synthesis of BTZ powders. Dielectric measurements on the sintered pellets showed a constant decrease in the dielectric permittivity values, which was largely attributed to the decreased crystallite/particle size. Additionally, the dielectric performance of the pellets revealed a strong frequency dispersion at lower frequencies observed only for the Zr-containing samples. This was attributed to the Maxwell-Wagner relaxation that typically emerges in fine nanograined ceramics with structural inhomogeneities such as increased porosity, which results in lower expected energy storage densities. Nevertheless, the dielectric performance for lower Zr concentrations ($x < 0.1$) was found to be promising and in line with the observation in the literature regarding the BTZ nanoceramics. Prolonged sintering times and higher temperatures should result in much denser ceramics with a better dielectric performance.

Overall, the SFS method was successfully demonstrated to be applicable to the synthesis of BaTiO₃ nanopowders and its derivatives. Further studies are needed to potentially optimize the choice of precursors, solvents, and synthesis parameters.

Appendix

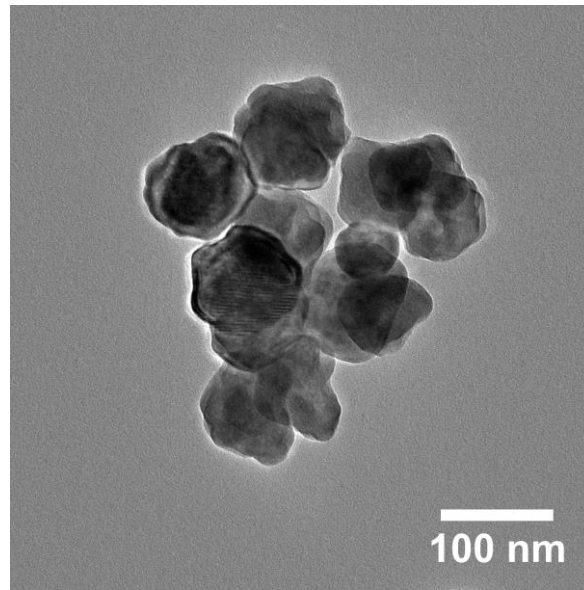


Figure. Appendix 1. TEM image of commercial BaTiO₃ powder (BTO-SA).

Literature

1. Feynman, R.P., *There's plenty of room at the bottom: An invitation to enter a new field of physics*, in *Handbook of Nanoscience, Engineering, and Technology, Third Edition*. 2012, CRC Press. 26-35.
2. Roco, M.C., *The long view of nanotechnology development: the National Nanotechnology Initiative at 10 years*. 2011, Springer.
3. Bhushan, B., *Springer handbook of nanotechnology*. 2017, Springer.
4. Chu, S., Y. Cui, and N. Liu, *The path towards sustainable energy*. *Nature Materials*, 2017. **16**(1): 16.
5. Suntivich, J., K.J. May, H.A. Gasteiger, J.B. Goodenough, and Y. Shao-Horn, *A perovskite oxide optimized for oxygen evolution catalysis from molecular orbital principles*. *Science*, 2011. **334**(6061): 1383-1385.
6. Green, M.A., A. Ho-Baillie, and H.J. Snaith, *The emergence of perovskite solar cells*. *Nature Photonics*, 2014. **8**(7).
7. Yao, Z., Z. Song, H. Hao, Z. Yu, M. Cao, S. Zhang, M.T. Lanagan, and H. Liu, *Homogeneous/Inhomogeneous-Structured Dielectrics and their Energy-Storage Performances*. *Advanced Materials*, 2017. **29**(20): 1601727.
8. Tilley, R.J., *Perovskites: structure-property relationships*. first ed. 2016, John Wiley & Sons.
9. Correa-Baena, J.-P., M. Saliba, T. Buonassisi, M. Grätzel, A. Abate, W. Tress, and A. Hagfeldt, *Promises and challenges of perovskite solar cells*. *Science*, 2017. **358**(6364): 739-744.
10. Arlt, G., D. Hennings, and G. de With, *Dielectric properties of fine-grained barium titanate ceramics*. *Journal of Applied Physics*, 1985. **58**(4): 1619-1625.
11. Ortega, N., A. Kumar, J.F. Scott, D.B. Chrisey, M. Tomazawa, S. Kumari, D.G. Diestra, and R.S. Katiyar, *Relaxor-ferroelectric superlattices: high energy density capacitors*. *Journal of Physics: Condensed Matter*, 2012. **24**(44): 445901.
12. Liang, Z., M. Liu, C. Ma, L. Shen, L. Lu, and C.-L. Jia, *High-performance BaZr_{0.35}Ti_{0.65}O₃ thin film capacitors with ultrahigh energy storage density and excellent thermal stability*. *Journal of Materials Chemistry A*, 2018. **6**(26): 12291-12297.
13. Sun, Z., C. Ma, X. Wang, M. Liu, L. Lu, M. Wu, X. Lou, H. Wang, and C.L. Jia, *Large Energy Density, Excellent Thermal Stability, and High Cycling Endurance of Lead-Free BaZr_{0.2}Ti_{0.8}O₃ Film Capacitors*. *ACS Applied Materials & Interfaces*, 2017. **9**(20): 17096-17101.
14. Instan, A.A., S.P. Pavunny, M.K. Bhattarai, and R.S. Katiyar, *Ultrahigh capacitive energy storage in highly oriented Ba(Zr_xTi_{1-x})O₃ thin films prepared by pulsed laser deposition*. *Applied Physics Letters*, 2017. **111**(14): 142903.
15. Ihlefeld, J.F., D.T. Harris, R. Keech, J.L. Jones, J.-P. Maria, and S. Trolier-McKinstry, *Scaling Effects in Perovskite Ferroelectrics: Fundamental Limits and Process-Structure-Property Relations*. *Journal of the American Ceramic Society*, 2016. **99**(8): 2537-2557.
16. Li, Y. and G.A. Somorjai, *Nanoscale advances in catalysis and energy applications*. *Nano Letters*, 2010. **10**(7): 2289-2295.
17. Tan, H., Z. Zhao, W.-b. Zhu, E.N. Coker, B. Li, M. Zheng, W. Yu, H. Fan, and Z. Sun, *Oxygen vacancy enhanced photocatalytic activity of perovskite SrTiO₃*. *ACS Applied Materials & Interfaces*, 2014. **6**(21): 19184-19190.
18. Grabowska, E., *Selected perovskite oxides: characterization, preparation and photocatalytic properties—a review*. *Applied Catalysis B: Environmental*, 2016. **186**: 97-126.

19. Alammari, T., I. Hamm, M. Wark, and A.-V. Mudring, *Low-temperature route to metal titanate perovskite nanoparticles for photocatalytic applications*. Applied Catalysis B: Environmental, 2015. **178**: 20-28.
20. Zeng, S., P. Kar, U.K. Thakur, and K. Shankar, *A review on photocatalytic CO₂ reduction using perovskite oxide nanomaterials*. Nanotechnology, 2018. **29**(5): 052001.
21. Kiss, B., T.D. Manning, D. Hesp, C. Didier, A. Taylor, D.M. Pickup, A.V. Chadwick, H.E. Allison, V.R. Dhanak, and J.B. Claridge, *Nano-structured rhodium doped SrTiO₃-Visible light activated photocatalyst for water decontamination*. Applied Catalysis B: Environmental, 2017. **206**: 547-555.
22. Cui, Y., J. Briscoe, and S. Dunn, *Effect of Ferroelectricity on Solar-Light-Driven Photocatalytic Activity of BaTiO₃: Influence on the Carrier Separation and Stern Layer Formation*. Chemistry of Materials, 2013. **25**(21): 4215-4223.
23. Li, L., X. Liu, Y. Zhang, P.A. Salvador, and G.S. Rohrer, *Heterostructured (Ba,Sr)TiO₃/TiO₂ core/shell photocatalysts: Influence of processing and structure on hydrogen production*. International Journal of Hydrogen Energy, 2013. **38**(17): 6948-6959.
24. Li, L., P.A. Salvador, and G.S. Rohrer, *Photocatalysts with internal electric fields*. Nanoscale, 2014. **6**(1): 24-42.
25. Dunne, P.W., C.L. Starkey, A.S. Munn, S.V. Tang, O. Luebben, I. Shvets, A.G. Ryder, Y. Casamayou-Boucau, L. Morrison, and E.H. Lester, *Bench-and pilot-scale continuous-flow hydrothermal production of barium strontium titanate nanopowders*. Chemical Engineering Journal, 2016. **289**: 433-441.
26. Buscaglia, M.T., M. Bassoli, V. Buscaglia, and R. Alessio, *Solid-State Synthesis of Ultrafine BaTiO₃ Powders from Nanocrystalline BaCO₃ and TiO₂*. Journal of the American Ceramic Society, 2005. **88**(9): 2374-2379.
27. Leite, E., D.T. Balogha, V.R. Mastelaro, S. Ferreira, and E. Marega Jr, *Insights on the mechanism of solid state reaction between TiO₂ and BaCO₃ to produce BaTiO₃ powders: The role of calcination, milling, and mixing solvent*. Ceramics International, 2019.
28. Boland, S.W., S.C. Pillai, W.-D. Yang, and S.M. Haile, *Preparation of (Pb,Ba)TiO₃ powders and highly oriented thin films by a sol-gel process*. Journal of Materials Research, 2004. **19**(05): 1492-1498.
29. Frey, M.H. and D.A. Payne, *Synthesis and processing of barium titanate ceramics from alkoxide solutions and monolithic gels*. Chemistry of Materials, 1995. **7**(1): 123-129.
30. Philippot, G., C. Elissalde, M. Maglione, and C. Aymonier, *Supercritical fluid technology: A reliable process for high quality BaTiO₃ based nanomaterials*. Advanced Powder Technology, 2014. **25**(5): 1415-1429.
31. Philippot, G., M. Albino, U.-C. Chung, M. Josse, C. Elissalde, M. Maglione, and C. Aymonier, *Continuous BaTi_{1-y}ZryO₃ (0 ≤ y ≤ 1) nanocrystals synthesis in supercritical fluids for nanostructured lead-free ferroelectric ceramics*. Materials & Design, 2015. **86**: 354-360.
32. Rabuffetti, F.A. and R.L. Brutchey, *Complex perovskite oxide nanocrystals: low-temperature synthesis and crystal structure*. Dalton Transactions, 2014. **43**(39): 14499-14513.
33. Kodas, T.T. and M.J. Hampden-Smith, *Aerosol processing of materials*. 1999, Wiley-Vch.
34. Lorke, A., M. Winterer, R. Schmechel, and C. Schulz, *Nanoparticles from the gasphase: Formation, structure, properties*. 2012, Springer Science & Business Media.
35. Teoh, W.Y., R. Amal, and L. Mädler, *Flame spray pyrolysis: an enabling technology for nanoparticles design and fabrication*. Nanoscale, 2010. **2**(8): 1324-1347.
36. Pratsinis, S.E., *Flame aerosol synthesis of ceramic powders*. Progress in Energy and Combustion Science, 1998. **24**(3): 197-219.

37. Mädler, L., H. Kammler, R. Mueller, and S. Pratsinis, *Controlled synthesis of nanostructured particles by flame spray pyrolysis*. Journal of Aerosol Science, 2002. **33**(2): 369-389.
38. Jossen, R., S. Pratsinis, W. Stark, and L. Mädler, *Criteria for Flame-Spray Synthesis of Hollow, Shell-Like, or Inhomogeneous Oxides*. Journal of the American Ceramic Society, 2005. **88**(6): 1388-1393.
39. Mädler, L., W. Stark, and S. Pratsinis, *Flame-made ceria nanoparticles*. Journal of Materials Research, 2002. **17**(06): 1356-1362.
40. Strobel, R. and S.E. Pratsinis, *Effect of solvent composition on oxide morphology during flame spray pyrolysis of metal nitrates*. Physical Chemistry Chemical Physics, 2011. **13**(20): 9246-52.
41. Li, S., Y. Ren, P. Biswas, and D.T. Stephen, *Flame aerosol synthesis of nanostructured materials and functional devices: Processing, modeling, and diagnostics*. Progress in Energy and Combustion Science, 2016. **55**: 1-59.
42. Heel, A., P. Holtappels, and T. Graule, *On the synthesis and performance of flame-made nanoscale $La_{0.6}Sr_{0.4}CoO_{3-\delta}$ and its influence on the application as an intermediate temperature solid oxide fuel cell cathode*. Journal of Power Sources, 2010. **195**(19): 6709-6718.
43. Liu, G., J. Li, K. Yang, W. Tang, H. Liu, J. Yang, R. Yue, and Y. Chen, *Effects of cerium incorporation on the catalytic oxidation of benzene over flame-made perovskite $La_{1-x}Ce_xMnO_3$ catalysts*. Particuology, 2015. **19**: 60-68.
44. Heel, A., P. Holtappels, P. Hug, and T. Graule, *Flame Spray Synthesis of Nanoscale $La_{0.6}Sr_{0.4}Co_{0.2}Fe_{0.8}O_{3-\delta}$ and $Ba_{0.5}Sr_{0.5}Co_{0.8}Fe_{0.2}O_{3-\delta}$ as Cathode Materials for Intermediate Temperature Solid Oxide Fuel Cells*. Fuel Cells, 2010. **10**(3): 419-432.
45. Ulrich, G.D., *Theory of particle formation and growth in oxide synthesis flames*. Combustion Science and Technology, 1971. **4**(1): 47-57.
46. Ulrich, G.D. and J.W. Riehl, *Aggregation and growth of submicron oxide particles in flames*. Journal of Colloid and Interface Science, 1982. **87**(1): 257-265.
47. Horlyck, J., C. Lawrey, E.C. Lovell, R. Amal, and J. Scott, *Elucidating the impact of Ni and Co loading on the selectivity of bimetallic NiCo catalysts for dry reforming of methane*. Chemical Engineering Journal, 2018. **352**: 572-580.
48. Hamid, N., S. Wennig, S. Hardt, A. Heinzl, C. Schulz, and H. Wiggers, *High-capacity cathodes for lithium-ion batteries from nanostructured $LiFePO_4$ synthesized by highly-flexible and scalable flame spray pyrolysis*. Journal of Power Sources, 2012. **216**: 76-83.
49. Meierhofer, F., H. Li, M. Gockeln, R. Kun, T. Grieb, A. Rosenauer, U. Fritsching, J. Kiefer, J. Birkenstock, and L. Mädler, *Screening Precursor-Solvent Combinations for $Li_4Ti_5O_{12}$ Energy Storage Material Using Flame Spray Pyrolysis*. ACS Applied Materials & Interfaces, 2017. **9**(43): 37760-37777.
50. Simmance, K., D. Thompsett, W. Wang, and B. Thiebaut, *Evaluation of perovskite catalysts prepared by flame spray pyrolysis for three-way catalyst activity under simulated gasoline exhaust feeds*. Catalysis Today, 2019. **320**: 40-50.
51. Angel, S., J. Neises, M. Dreyer, K.F. Ortega, M. Behrens, Y. Wang, H. Arandiyán, C. Schulz, and H. Wiggers, *Spray-flame synthesis of $La(Fe,Co)O_3$ nano-perovskites from metal nitrates*. AIChE Journal.
52. Chiarello, G., I. Rossetti, L. Forni, P. Lopinto, and G. Migliavacca, *Solvent nature effect in preparation of perovskites by flame-pyrolysis: 1. Carboxylic acids*. Applied Catalysis B: Environmental, 2007. **72**(3): 218-226.
53. Chiarello, G., I. Rossetti, L. Forni, P. Lopinto, and G. Migliavacca, *Solvent nature effect in preparation of perovskites by flame pyrolysis: 2. Alcohols and alcohols+ propionic acid mixtures*. Applied Catalysis B: Environmental, 2007. **72**(3): 227-232.

54. Chiarello, G.L., J.-D. Grunwaldt, D. Ferri, F. Krumeich, C. Oliva, L. Forni, and A. Baiker, *Flame-synthesized LaCoO₃-supported Pd: 1. Structure, thermal stability and reducibility*. *Journal of Catalysis*, 2007. **252**(2): 127-136.
55. Chiarello, G.L., I. Rossetti, and L. Forni, *Flame-spray pyrolysis preparation of perovskites for methane catalytic combustion*. *Journal of catalysis*, 2005. **236**(2): 251-261.
56. Brewster, J.H. and T.T. Kodas, *Generation of unagglomerated, Dense, BaTiO₃ particles by flame-spray pyrolysis*. *AIChE Journal*, 1997. **43**(S11): 2665-2669.
57. Messing, G.L., S.C. Zhang, and G.V. Jayanthi, *Ceramic powder synthesis by spray pyrolysis*. *Journal of the American Ceramic Society*, 1993. **76**(11): 2707-2726.
58. Itoh, Y., I.W. Lenggoro, S.E. Pratsinis, and K. Okuyama, *Agglomerate-free BaTiO₃ particles by salt-assisted spray pyrolysis*. *Journal of Materials Research*, 2002. **17**(12): 3222-3229.
59. Purwanto, A., W.-N. Wang, I.W. Lenggoro, and K. Okuyama, *Formation of BaTiO₃ nanoparticles from an aqueous precursor by flame-assisted spray pyrolysis*. *Journal of the European Ceramic Society*, 2007. **27**(16): 4489-4497.
60. Terashi, Y., A. Purwanto, W.-N. Wang, F. Iskandar, and K. Okuyama, *Role of urea addition in the preparation of tetragonal BaTiO₃ nanoparticles using flame-assisted spray pyrolysis*. *Journal of the European Ceramic Society*, 2008. **28**(13): 2573-2580.
61. Choi, D.H., A. Baker, M. Lanagan, S. Trolier-McKinstry, and C. Randall, *Structural and Dielectric Properties in (1-x) BaTiO_{3-x}Bi(Mg_{1/2}Ti_{1/2})O₃ Ceramics (0.1 ≤ x ≤ 0.5) and Potential for High-Voltage Multilayer Capacitors*. *Journal of the American Ceramic Society*, 2013. **96**(7): 2197-2202.
62. Schädli, G.N., R. Büchel, and S.E. Pratsinis, *Nanogenerator power output: influence of particle size and crystallinity of BaTiO₃*. *Nanotechnology*, 2017. **28**(27): 275705.
63. Ullmann, H. and N. Trofimenko, *Estimation of effective ionic radii in highly defective perovskite-type oxides from experimental data*. *Journal of alloys and compounds*, 2001. **316**(1-2): 153-158.
64. Stølen, S., E. Bakken, and C.E. Mohn, *Oxygen-deficient perovskites: linking structure, energetics and ion transport*. *Physical Chemistry Chemical Physics*, 2006. **8**(4): 429-447.
65. Öpik, U. and M.H.L. Pryce, *Studies of the Jahn-Teller effect. I. A survey of the static problem*. *Proceedings of the Royal Society of London. Series A. Mathematical and Physical Sciences*, 1957. **238**(1215): 425-447.
66. Jahn, H.A. and E. Teller, *Stability of polyatomic molecules in degenerate electronic states — Orbital degeneracy*. *Proceedings of the Royal Society of London. Series A-Mathematical and Physical Sciences*, 1937. **161**(905): 220-235.
67. Polinger, V. and I. Bersuker. *Pseudo Jahn-Teller effect in permittivity of ferroelectric perovskites*. in *Journal of Physics: Conference Series*. 2017. IOP Publishing.
68. Kwon, S., W. Hackenberger, E. Alberta, E. Furman, and M. Lanagan, *Nonlinear dielectric ceramics and their applications to capacitors and tunable dielectrics*. *IEEE Electrical Insulation Magazine*, 2011. **27**(2): 43-55.
69. Kunz, M. and I.D. Brown, *Out-of-center distortions around octahedrally coordinated d⁰ transition metals*. *Journal of Solid State Chemistry*, 1995. **115**(2): 395-406.
70. Castillo, N.C., A. Heel, T. Graule, and C. Pulgarin, *Flame-assisted synthesis of nanoscale, amorphous and crystalline, spherical BiVO₄ with visible-light photocatalytic activity*. *Applied Catalysis B: Environmental*, 2010. **95**(3): 335-347.
71. Smith, M.B., K. Page, T. Siegrist, P.L. Redmond, E.C. Walter, R. Seshadri, L.E. Brus, and M.L. Steigerwald, *Crystal structure and the paraelectric-to-ferroelectric phase transition of nanoscale BaTiO₃*. *Journal of the American Chemical Society*, 2008. **130**(22): 6955-6963.

72. Chen, Y.-C., S.-M. Tsao, C.-S. Lin, S.-C. Wang, and Y.-H. Chien, *Microwave dielectric properties of 0.95MgTiO₃-0.05 CaTiO₃ for application in dielectric resonator antenna*. Journal of Alloys and Compounds, 2009. **471**(1-2): 347-351.
73. Jo, H.J., J.S. Kim, and E.S. Kim, *Microwave dielectric properties of MgTiO₃-based ceramics*. Ceramics International, 2015. **41**: S530-S536.
74. Pal, N., M. Paul, and A. Bhaumik, *New mesoporous perovskite ZnTiO₃ and its excellent catalytic activity in liquid phase organic transformations*. Applied Catalysis A: General, 2011. **393**(1-2): 153-160.
75. Surendar, T., S. Kumar, and V. Shanker, *Influence of La-doping on phase transformation and photocatalytic properties of ZnTiO₃ nanoparticles synthesized via modified sol-gel method*. Physical Chemistry Chemical Physics, 2014. **16**(2): 728-735.
76. Yan, Y., H. Yang, X. Zhao, R. Li, and X. Wang, *Enhanced photocatalytic activity of surface disorder-engineered CaTiO₃*. Materials Research Bulletin, 2018. **105**: 286-290.
77. Huang, L., Z. Jia, I. Kymissis, and S. O'Brien, *High K Capacitors and OFET Gate Dielectrics from Self-Assembled BaTiO₃ and (Ba,Sr)TiO₃ Nanocrystals in the Superparaelectric Limit*. Advanced Functional Materials, 2010. **20**(4): 554-560.
78. Sindhu, M., N. Ahlawat, S. Sanghi, R. Kumari, and A. Agarwal, *Crystal structure refinement and investigation of electrically heterogeneous microstructure of single phased Sr substituted BaTiO₃ ceramics*. Journal of Alloys and Compounds, 2013. **575**: 109-114.
79. Gao, Y., V.V. Shvartsman, D. Gautam, M. Winterer, and D.C. Lupascu, *Nanocrystalline barium strontium titanate ceramics synthesized via the "organosol" route and spark plasma sintering*. Journal of the American Ceramic Society, 2014. **97**(7): 2139-2146.
80. Liu, J., G. Chen, Z. Li, and Z. Zhang, *Electronic structure and visible light photocatalysis water splitting property of chromium-doped SrTiO₃*. Journal of Solid State Chemistry, 2006. **179**(12): 3704-3708.
81. Kudo, A. and Y. Miseki, *Heterogeneous photocatalyst materials for water splitting*. Chemical Society Reviews, 2009. **38**(1): 253-278.
82. Townsend, T.K., N.D. Browning, and F.E. Osterloh, *Nanoscale strontium titanate photocatalysts for overall water splitting*. ACS Nano, 2012. **6**(8): 7420-7426.
83. Kuang, Q. and S. Yang, *Template synthesis of single-crystal-like porous SrTiO₃ nanocube assemblies and their enhanced photocatalytic hydrogen evolution*. ACS applied materials & interfaces, 2013. **5**(9): 3683-3690.
84. Iwashina, K. and A. Kudo, *Rh-doped SrTiO₃ photocatalyst electrode showing cathodic photocurrent for water splitting under visible-light irradiation*. Journal of the American Chemical Society, 2011. **133**(34): 13272-13275.
85. Basmajian, J. and R. DeVries, *Phase equilibria in the system BaTiO₃-SrTiO₃*. Journal of the American Ceramic Society, 1957. **40**(11): 373-376.
86. Philippot, G., K.M. Jensen, M. Christensen, C. Elissalde, M. Maglione, B.B. Iversen, and C. Aymonier, *Coupling in situ synchrotron radiation with ex situ spectroscopy characterizations to study the formation of Ba_{1-x}Sr_xTiO₃ nanoparticles in supercritical fluids*. The Journal of Supercritical Fluids, 2014. **87**: 111-117.
87. Shin, S.S., E.J. Yeom, W.S. Yang, S. Hur, M.G. Kim, J. Im, J. Seo, J.H. Noh, and S.I. Seok, *Colloidally prepared La-doped BaSnO₃ electrodes for efficient, photostable perovskite solar cells*. Science, 2017. **356**(6334): 167-171.
88. Yang, X., X. Han, T. He, and Y. Du, *Enhanced Stability of BaCoO_{3-δ} Using Doping Process as a Cathode Material for IT-SOFCs*. ECS Transactions, 2017. **78**(1): 543-550.
89. Dong, L., D.S. Stone, and R.S. Lakes, *Enhanced dielectric and piezoelectric properties of x BaZrO₃-(1-x) BaTiO₃ ceramics*. Journal of Applied Physics, 2012. **111**(8): 084107.

90. Guo, H., J. Guo, A. Baker, and C.A. Randall, *Hydrothermal-Assisted Cold Sintering Process: A New Guidance for Low-Temperature Ceramic Sintering*. ACS Applied Materials & Interfaces, 2016. **8**(32): 20909-20915.
91. Karan, N., R. Katiyar, T. Maiti, R. Guo, and A. Bhalla, *Raman spectral studies of Zr⁴⁺-rich BaZr_xTi_{1-x}O₃ (0.5 ≤ x ≤ 1.00) phase diagram*. Journal of Raman Spectroscopy: An International Journal for Original Work in all Aspects of Raman Spectroscopy, Including Higher Order Processes, and also Brillouin and Rayleigh Scattering, 2009. **40**(4): 370-375.
92. Shvartsman, V.V., D.C. Lupascu, and D.J. Green, *Lead-Free Relaxor Ferroelectrics*. Journal of the American Ceramic Society, 2012. **95**(1): 1-26.
93. Maiti, T., R. Guo, and A. Bhalla, *Structure-property phase diagram of BaZr_xTi_{1-x}O₃ system*. Journal of the American Ceramic Society, 2008. **91**(6): 1769-1780.
94. Miao, S., J. Pokorny, U. Pasha, O. Thakur, D. Sinclair, and I. Reaney, *Polar order and diffuse scatter in Ba (Ti_{1-x}Zr_x)O₃ ceramics*. Journal of Applied Physics, 2009. **106**(11): 114111.
95. Buscaglia, V., S. Tripathi, V. Petkov, M. Dapiaggi, M. Deluca, A. Gajović, and Y. Ren, *Average and local atomic-scale structure in BaZr_xTi_{1-x}O₃ (x= 0.10, 0.20, 0.40) ceramics by high-energy x-ray diffraction and Raman spectroscopy*. Journal of Physics: Condensed Matter, 2014. **26**(6): 065901.
96. Fang, Z. and H. Wang, *Densification and grain growth during sintering of nanosized particles*. International Materials Reviews, 2008. **53**(6): 326-352.
97. Maglia, F., I.G. Tredici, and U. Anselmi-Tamburini, *Densification and properties of bulk nanocrystalline functional ceramics with grain size below 50 nm*. Journal of the European Ceramic Society, 2013. **33**(6): 1045-1066.
98. German, R., *Sintering: from empirical observations to scientific principles*. 2014, Butterworth-Heinemann.
99. Braslavsky, S.E., A.M. Braun, A.E. Cassano, A.V. Emeline, M.I. Litter, L. Palmisano, V.N. Parmon, and N. Serpone, *Glossary of terms used in photocatalysis and radiation catalysis (IUPAC Recommendations 2011)*. Pure and Applied Chemistry, 2011. **83**(4): 931-1014.
100. McCullagh, C., J.M. Robertson, D.W. Bahnemann, and P.K. Robertson, *The application of TiO₂ photocatalysis for disinfection of water contaminated with pathogenic micro-organisms: a review*. Research on Chemical Intermediates, 2007. **33**(3-5): 359-375.
101. Roy, S.C., O.K. Varghese, M. Paulose, and C.A. Grimes, *Toward solar fuels: photocatalytic conversion of carbon dioxide to hydrocarbons*. ACS Nano, 2010. **4**(3): 1259-1278.
102. Linsebigler, A.L., G. Lu, and J.T. Yates Jr, *Photocatalysis on TiO₂ surfaces: principles, mechanisms, and selected results*. Chemical Reviews, 1995. **95**(3): 735-758.
103. Schneider, J., M. Matsuoka, M. Takeuchi, J. Zhang, Y. Horiuchi, M. Anpo, and D.W. Bahnemann, *Understanding TiO₂ photocatalysis: mechanisms and materials*. Chemical Reviews, 2014. **114**(19): 9919-9986.
104. Strunk, J., *Requirements for efficient metal oxide photocatalysts for CO₂ reduction*, in *Metal Oxides in Energy Technologies*. 2018, Elsevier. 275-301.
105. Kisch, H., *Semiconductor photocatalysis: principles and applications*. 2014, John Wiley & Sons.
106. Van de Krol, R. and M. Grätzel, *Photoelectrochemical hydrogen production*. Vol. 90. 2012, Springer.
107. Suen, N.-T., S.-F. Hung, Q. Quan, N. Zhang, Y.-J. Xu, and H.M. Chen, *Electrocatalysis for the oxygen evolution reaction: recent development and future perspectives*. Chemical Society Reviews, 2017. **46**(2): 337-365.

108. Schneider, J. and D.W. Bahnemann, *Undesired role of sacrificial reagents in photocatalysis*. The Journal of Physical Chemistry Letters, 2013. **4**(20): 3479-3483.
109. Ahmad, H., S. Kamarudin, L. Minggu, and M. Kassim, *Hydrogen from photo-catalytic water splitting process: A review*. Renewable and Sustainable Energy Reviews, 2015. **43**: 599-610.
110. Kato, H. and A. Kudo, *Visible-light-response and photocatalytic activities of TiO₂ and SrTiO₃ photocatalysts codoped with antimony and chromium*. The Journal of Physical Chemistry B, 2002. **106**(19): 5029-5034.
111. Weber, M.F. and M. Dignam, *Splitting water with semiconducting photoelectrodes—Efficiency considerations*. International Journal of Hydrogen Energy, 1986. **11**(4): 225-232.
112. Dodd, A., A. McKinley, M. Saunders, and T. Tsuzuki, *Effect of particle size on the photocatalytic activity of nanoparticulate zinc oxide*. Journal of Nanoparticle Research, 2006. **8**(1): 43.
113. Bi, Y., S. Ouyang, N. Umezawa, J. Cao, and J. Ye, *Facet effect of single-crystalline Ag₃PO₄ sub-microcrystals on photocatalytic properties*. Journal of the American Chemical Society, 2011. **133**(17): 6490-6492.
114. Kimijima, T., K. Kanie, M. Nakaya, and A. Muramatsu, *Solvothermal synthesis of SrTiO₃ nanoparticles precisely controlled in surface crystal planes and their photocatalytic activity*. Applied Catalysis B: Environmental, 2014. **144**: 462-467.
115. Zou, F., Z. Jiang, X. Qin, Y. Zhao, L. Jiang, J. Zhi, T. Xiao, and P.P. Edwards, *Template-free synthesis of mesoporous N-doped SrTiO₃ perovskite with high visible-light-driven photocatalytic activity*. Chemical Communications, 2012. **48**(68): 8514-8516.
116. Burbure, N.V., P.A. Salvador, and G.S. Rohrer, *Photochemical reactivity of titania films on BaTiO₃ substrates: origin of spatial selectivity*. Chemistry of Materials, 2010. **22**(21): 5823-5830.
117. Burbure, N.V., P.A. Salvador, and G.S. Rohrer, *Influence of dipolar fields on the photochemical reactivity of thin titania films on BaTiO₃ substrates*. Journal of the American Ceramic Society, 2006. **89**(9): 2943-2945.
118. Inoue, Y., M. Okamura, and K. Sato, *A thin-film semiconducting titanium dioxide combined with ferroelectrics for photoassisted water decomposition*. The Journal of Physical Chemistry, 1985. **89**(24): 5184-5187.
119. Inoue, Y., K. Sato, K. Sato, and H. Miyama, *Photoassisted water decomposition by ferroelectric lead zirconate titanate ceramics with anomalous photovoltaic effects*. The Journal of Physical Chemistry, 1986. **90**(13): 2809-2810.
120. Inoue, Y., K. Sato, and S. Suzuki, *Polarization effects upon adsorptive and catalytic properties. 2. Surface electrical conductivity of nickel (II) oxide deposited on lithium niobate (LiNbO₃) and its changes upon gas adsorption*. The Journal of Physical Chemistry, 1985. **89**(13): 2827-2831.
121. Inoue, Y., I. Yoshioka, and K. Sato, *Polarization effects upon adsorptive and catalytic properties. 1. Carbon monoxide oxidation over palladium deposited on lithium niobate (LiNbO₃) ferroelectrics*. The Journal of Physical Chemistry, 1984. **88**(6): 1148-1151.
122. Liu, Y., L. Xie, Y. Li, R. Yang, J. Qu, Y. Li, and X. Li, *Synthesis and high photocatalytic hydrogen production of SrTiO₃ nanoparticles from water splitting under UV irradiation*. Journal of Power Sources, 2008. **183**(2): 701-707.
123. Da Silva, L.F., W. Avansi, J. Andrés, C. Ribeiro, M.L. Moreira, E. Longo, and V.R. Mastelaro, *Long-range and short-range structures of cube-like shape SrTiO₃ powders: microwave-assisted hydrothermal synthesis and photocatalytic activity*. Physical Chemistry Chemical Physics, 2013. **15**(29): 12386-12393.
124. Xiao, H., S. Xie, Y. Chen, and R. Huang, *An optimized transformerless photovoltaic grid-connected inverter*. IEEE Transactions on Industrial Electronics, 2010. **58**(5): 1887-1895.

125. Hao, X., *A review on the dielectric materials for high energy-storage application*. Journal of Advanced Dielectrics, 2013. **3**(01): 1330001.
126. Thakur, V.K. and R.K. Gupta, *Recent progress on ferroelectric polymer-based nanocomposites for high energy density capacitors: synthesis, dielectric properties, and future aspects*. Chemical Reviews, 2016. **116**(7): 4260-4317.
127. Dougherty, J.P., *Cardiac defibrillator with high energy storage antiferroelectric capacitor*. 1996, Google Patents.
128. Pan, M.-J. and C.A. Randall, *A brief introduction to ceramic capacitors*. IEEE Electrical Insulation Magazine, 2010. **26**(3).
129. Hammond, P., *Electromagnetism for Engineers: An Introductory Course*. 2013, Elsevier Science.
130. Serway, R.A. and C. Vuille, *College physics*. 2014, Cengage Learning.
131. Buscaglia, V., M.T. Buscaglia, M. Viviani, L. Mitoseriu, P. Nanni, V. Trefiletti, P. Piaggio, I. Gregora, T. Ostapchuk, J. Pokorný, and J. Petzelt, *Grain size and grain boundary-related effects on the properties of nanocrystalline barium titanate ceramics*. Journal of the European Ceramic Society, 2006. **26**(14): 2889-2898.
132. Tan, Y., J. Zhang, Y. Wu, C. Wang, V. Koval, B. Shi, H. Ye, R. McKinnon, G. Viola, and H. Yan, *Unfolding grain size effects in barium titanate ferroelectric ceramics*. Scientific Reports, 2015. **5**: 9953.
133. Curecheriu, L., S.B. Balmus, M.T. Buscaglia, V. Buscaglia, A. Ianculescu, and L. Mitoseriu, *Grain size-dependent properties of dense nanocrystalline barium titanate ceramics*. Journal of the American Ceramic Society, 2012. **95**(12): 3912-3921.
134. Gong, H., X. Wang, S. Zhang, H. Wen, and L. Li, *Grain size effect on electrical and reliability characteristics of modified fine-grained BaTiO₃ ceramics for MLCCs*. Journal of the European Ceramic Society, 2014. **34**(7): 1733-1739.
135. Yoon, S., J. Dornseiffer, Y. Xiong, D. Grüner, Z. Shen, S. Iwaya, C. Pithan, and R. Waser, *Spark plasma sintering of nanocrystalline BaTiO₃-powders: consolidation behavior and dielectric characteristics*. Journal of the European Ceramic Society, 2011. **31**(9): 1723-1731.
136. Winterer, M., *Nanocrystalline ceramics: synthesis and structure*. Vol. 53. 2013, Springer Science & Business Media.
137. Ghayour, H. and M. Abdellahi, *A brief review of the effect of grain size variation on the electrical properties of BaTiO₃-based ceramics*. Powder Technology, 2016. **292**: 84-93.
138. Damjanovic, D., *Hysteresis in piezoelectric and ferroelectric materials*. The Science of Hysteresis, 2006. **3**: 337-465.
139. Correia, T.M., M. McMillen, M.K. Rokosz, P.M. Weaver, J.M. Gregg, G. Viola, and M.G. Cain, *A lead-free and high-energy density ceramic for energy storage applications*. Journal of the American Ceramic Society, 2013. **96**(9): 2699-2702.
140. Shen, Z., X. Wang, B. Luo, and L. Li, *BaTiO₃-BiYbO₃ perovskite materials for energy storage applications*. Journal of Materials Chemistry A, 2015. **3**(35): 18146-18153.
141. Puli, V.S., A. Kumar, D.B. Chrisey, M. Tomozawa, J. Scott, and R.S. Katiyar, *Barium zirconate-titanate/barium calcium-titanate ceramics via sol-gel process: novel high-energy-density capacitors*. Journal of Physics D: Applied Physics, 2011. **44**(39): 395403.
142. Rabuffetti, F.A. and R.L. Brutchey, *Local structural distortion of BaZr_xTi_{1-x}O₃ nanocrystals synthesized at room temperature*. Chemical Communications, 2012. **48**(10): 1437-1439.
143. Rosebrock, C.D., N. Riefler, T. Wriedt, L. Mädler, and S.D. Tse, *Disruptive burning of precursor/solvent droplets in flame-spray synthesis of nanoparticles*. AIChE Journal, 2013. **59**(12): 4553-4566.

144. Rosebrock, C.D., T. Wriedt, L. Mädler, and K. Wegner, *The role of microexplosions in flame spray synthesis for homogeneous nanopowders from low-cost metal precursors*. *AIChE Journal*, 2016. **62**(2): 381-391.
145. Friedlander, S.K., *Smoke, dust, and haze: fundamentals of aerosol dynamics*. *Topics in chemical engineering*. 2000, Oxford University Press, New York.
146. Edelstein, A.S. and R. Cammaratra, *Nanomaterials: synthesis, properties and applications*. 1998, CRC press.
147. Smoluchowski M, *Drei Vorträge über Diffusion, Brownsche Molekularbewegung und Koagulation von Kolloidteilchen*. *Physikalische Zeitschrift*, 1916(17): 557–571, 585–599.
148. Eggersdorfer, M.L. and S.E. Pratsinis, *Agglomerates and aggregates of nanoparticles made in the gas phase*. *Advanced Powder Technology*, 2014. **25**(1): 71-90.
149. Matsoukas, T. and S.K. Friedlander, *Dynamics of aerosol agglomerate formation*. *Journal of Colloid and Interface Science*, 1991. **146**(2): 495-506.
150. Tsantilis, S. and S.E. Pratsinis, *Soft-and hard-agglomerate aerosols made at high temperatures*. *Langmuir*, 2004. **20**(14): 5933-5939.
151. Hardt, S., *Dissertation: "Entwicklung eines Sprayflammenreaktors zur Synthese oxidischer Nanopartikel bei variablem Druck"*. 2015. 124.
152. Tarasov, A., V. Shvartsman, S. Shoja, D. Lewin, D. Lupascu, and H. Wiggers, *Spray-flame synthesis of BaTi_{1-x}ZrxO₃ nanoparticles for energy storage applications*. *Ceramics International*, 2020. **46**(9): 13915-13924.
153. Hardt, S., I. Wlokas, C. Schulz, and H. Wiggers, *Impact of Ambient Pressure on Titania Nanoparticle Formation During Spray-Flame Synthesis*. *Journal of nanoscience and nanotechnology*, 2015. **15**(12): 9449-9456.
154. Cullity, B., *Element of X-ray Diffraction* 1978, Addison-Wesley Reading.
155. Kaduk, J.A. and J. Reid, *Typical values of Rietveld instrument profile coefficients*. *Powder Diffraction*, 2011. **26**(1): 88-93.
156. Toby, B.H. and R.B. Von Dreele, *GSAS-II: the genesis of a modern open-source all purpose crystallography software package*. *Journal of Applied Crystallography*, 2013. **46**(2): 544-549.
157. Suryanarayana, C. and M.G. Norton, *X-ray diffraction: a practical approach*. 2013, Springer Science & Business Media.
158. Kohl, H. and L. Reimer, *Transmission electron microscopy: physics of image formation*. 2008, Springer.
159. Larkin, P., *Infrared and Raman spectroscopy: principles and spectral interpretation*. 2017, Elsevier.
160. Gouadec, G. and P. Colomban, *Raman Spectroscopy of nanomaterials: How spectra relate to disorder, particle size and mechanical properties*. *Progress in crystal growth and characterization of materials*, 2007. **53**(1): 1-56.
161. Stuart, B., *Infrared spectroscopy: fundamentals and applications*. 2004.
162. Günzler, H. and H.-U. Gremlich, *IR-Spektroskopie: Eine Einführung*. 2012, John Wiley & Sons.
163. Schüth, F., K.S.W. Sing, and J. Weitkamp, *Handbook of porous solids*. 2002, Wiley-Vch.
164. Lowell, S., J.E. Shields, M.A. Thomas, and M. Thommes, *Characterization of porous solids and powders: surface area, pore size and density*. Vol. 16. 2012, Springer Science & Business Media.
165. Brown, M. and P. Gallagher, *Handbook of Thermal Analysis and Calorimetry, Volume 1: Principles and Practice*. 1998, Elsevier, Amsterdam.

166. Rabuffetti, F.A., H.-S. Kim, J.A. Enterkin, Y. Wang, C.H. Lanier, L.D. Marks, K.R. Poeppelmeier, and P.C. Stair, *Synthesis-dependent first-order Raman scattering in SrTiO₃ nanocubes at room temperature*. Chemistry of Materials, 2008. **20**(17): 5628-5635.
167. Awan, I.T., A.H. Pinto, I. Nogueira, V. Bezzon, E. Leite, D.T. Balogh, V.R. Mastelaro, S. Ferreira, and E. Marega Jr, *Insights on the mechanism of solid state reaction between TiO₂ and BaCO₃ to produce BaTiO₃ powders: The role of calcination, milling, and mixing solvent*. Ceramics International, 2020. **46**(3): 2987-3001.
168. Bettini, L.G., M.V. Dozzi, F. Della Foglia, G.L. Chiarello, E. Selli, C. Lenardi, P. Piseri, and P. Milani, *Mixed-phase nanocrystalline TiO₂ photocatalysts produced by flame spray pyrolysis*. Applied Catalysis B: Environmental, 2015. **178**: 226-232.
169. Kumar, S., G.L. Messing, and W.B. White, *Metal organic resin derived barium titanate: I, Formation of barium titanium oxycarbonate intermediate*. Journal of the American Ceramic Society, 1993. **76**(3): 617-624.
170. Mos, R., M. Nasui, T. Petrisor Jr, A. Mesaros, L. Ciontea, and T. Petrisor, *The thermal decomposition of metal-organic precursors for epitaxial growth of SrZrO₃ thin films*. Journal of Analytical and Applied Pyrolysis, 2015. **115**: 255-261.
171. Li, H., C. Rosebrock, N. Riefler, T. Wriedt, and L. Mädler, *Experimental investigation on microexplosion of single isolated burning droplets containing titanium tetraisopropoxide for nanoparticle production*. Proceedings of the Combustion Institute, 2017. **36**(1): 1011-1018.
172. Chiarello, G.L., E. Selli, and L. Forni, *Photocatalytic hydrogen production over flame spray pyrolysis-synthesised TiO₂ and Au/TiO₂*. Applied Catalysis B: Environmental, 2008. **84**(1): 332-339.
173. Pratsinis, S.E., W. Zhu, and S. Vemury, *The role of gas mixing in flame synthesis of titania powders*. Powder Technology, 1996. **86**(1): 87-93.
174. Kodas, T.T. and M.J. Hampden-Smith, *Aerosol processing of materials*. Vol. 33. 1999, Wiley-Vch New York.
175. Torabmostaedi, H., T. Zhang, P. Foot, S. Dembele, and C. Fernandez, *Process control for the synthesis of ZrO₂ nanoparticles using FSP at high production rate*. Powder technology, 2013. **246**: 419-433.
176. Buscaglia, V., M. Buscaglia, M. Viviani, L. Mitoseriu, P. Nanni, V. Trefiletti, P. Piaggio, I. Gregora, T. Ostapchuk, and J. Pokorný, *Grain size and grain boundary-related effects on the properties of nanocrystalline barium titanate ceramics*. Journal of the European Ceramic Society, 2006. **26**(14): 2889-2898.
177. Arima, M., M. Kakihana, Y. Nakamura, M. Yashima, and M. Yoshimura, *Polymerized Complex Route to Barium Titanate Powders Using Barium-Titanium Mixed-Metal Citric Acid Complex*. Journal of the American Ceramic Society, 1996. **79**(11): 2847-2856.
178. Yashima, M., T. Hoshina, D. Ishimura, S. Kobayashi, W. Nakamura, T. Tsurumi, and S. Wada, *Size effect on the crystal structure of barium titanate nanoparticles*. Journal of Applied Physics, 2005. **98**(1): 014313.
179. Burbank, R. and H.T. Evans, *The crystal structure of hexagonal barium titanate*. Acta Crystallographica, 1948. **1**(6): 330-336.
180. Ctibor, P., H. Ageorges, V. Stengl, N. Murafa, I. Pis, T. Zahoranova, V. Nehasil, and Z. Pala, *Structure and properties of plasma sprayed BaTiO₃ coatings: Spray parameters versus structure and photocatalytic activity*. Ceramics International, 2011. **37**(7): 2561-2567.
181. Busca, G., V. Buscaglia, M. Leoni, and P. Nanni, *Solid-state and surface spectroscopic characterization of BaTiO₃ fine powders*. Chemistry of Materials, 1994. **6**(7): 955-961.

182. Green, I.X., W. Tang, M. Neurock, and J.T. Yates, *Mechanistic insights into the partial oxidation of acetic acid by O₂ at the dual perimeter sites of a Au/TiO₂ catalyst*. Faraday discussions, 2013. **162**: 247-265.
183. Hennings, D., G. Rosenstein, and H. Schreinemacher, *Hydrothermal preparation of barium titanate from barium-titanium acetate gel precursors*. Journal of the European Ceramic Society, 1991. **8**(2): 107-115.
184. Hwang, U.-Y., H.-S. Park, and K.-K. Koo, *Behavior of barium acetate and titanium isopropoxide during the formation of crystalline barium titanate*. Industrial & Engineering Chemistry Research, 2004. **43**(3): 728-734.
185. Adam, J., G. Klein, and T. Lehnert, *Hydroxyl content of BaTiO₃ nanoparticles with varied size*. Journal of the American Ceramic Society, 2013. **96**(9): 2987-2993.
186. Veith, M., S. Mathur, N. Lecerf, V. Huch, T. Decker, H.P. Beck, W. Eiser, and R. Haberkorn, *Sol-gel synthesis of nano-scaled BaTiO₃, BaZrO₃ and BaTi_{0.5}Zr_{0.5}O₃ oxides via single-source alkoxide precursors and semi-alkoxide routes*. Journal of Sol-gel Science and Technology, 2000. **17**(2): 145-158.
187. Phule, P. and S. Risbud, *Low temperature synthesis and dielectric properties of ceramics derived from amorphous barium titanate gels and crystalline powders*. Materials Science and Engineering: B, 1989. **3**(3): 241-247.
188. Hennings, D. and S. Schreinemacher, *Characterization of hydrothermal barium titanate*. Journal of the European Ceramic Society, 1992. **9**(1): 41-46.
189. Lee, S., C.A. Randall, and Z.K. Liu, *Factors limiting equilibrium in fabricating a simple ferroelectric oxide: BaTiO₃*. Journal of the American Ceramic Society, 2009. **92**(1): 222-228.
190. Miot, C., E. Husson, C. Proust, R. Erre, and J. Coutures, *X-ray photoelectron spectroscopy characterization of barium titanate ceramics prepared by the citric route. Residual carbon study*. Journal of Materials Research, 1997. **12**(9): 2388-2392.
191. Beauger, A., J. Mutin, and J. Niepce, *Synthesis reaction of metatitanate BaTiO₃*. Journal of Materials Science, 1983. **18**(10): 3041-3046.
192. Frey, M.H. and D.A. Payne, *Grain-size effect on structure and phase transformations for barium titanate*. Physical Review B, 1996. **54**(5): 3158-3168.
193. Robins, L.H., D.L. Kaiser, L.D. Rotter, P.K. Schenck, G.T. Stauf, and D. Rytz, *Investigation of the structure of barium titanate thin films by Raman spectroscopy*. Journal of Applied Physics, 1994. **76**(11): 7487-7498.
194. Lee, S., C.A. Randall, and Z.K. Liu, *Modified phase diagram for the barium oxide–titanium dioxide system for the ferroelectric barium titanate*. Journal of the American Ceramic Society, 2007. **90**(8): 2589-2594.
195. Pfaff, G., *Synthesis and characterization of Ba₂TiO₄*. Journal of Materials Science Letters, 1991. **10**(18): 1059-1060.
196. Teleki, A., R. Wengeler, L. Wengeler, H. Nirschl, and S. Pratsinis, *Distinguishing between aggregates and agglomerates of flame-made TiO₂ by high-pressure dispersion*. Powder Technology, 2008. **181**(3): 292-300.
197. Grewe, T. and H. Tüysüz, *Activated-Carbon-Templated Crystalline Tantalates for Photocatalytic Water Splitting*. ChemNanoMat, 2016. **2**(4): 273-280.
198. Grewe, T. and H. Tüysüz, *Alkali metals incorporated ordered mesoporous tantalum oxide with enhanced photocatalytic activity for water splitting*. Journal of Materials Chemistry A, 2016. **4**(8): 3007-3017.
199. Mahesh, M., V.B. Prasad, and A. James, *Effect of sintering temperature on the microstructure and electrical properties of zirconium doped barium titanate ceramics*. Journal of Materials Science: Materials in Electronics, 2013. **24**(12): 4684-4692.

200. Yu, Z., R. Guo, and A. Bhalla, *Dielectric behavior of Ba (Ti_{1-x}Zr_x)O₃ single crystals*. Journal of Applied Physics, 2000. **88**(1): 410-415.
201. Dobal, P., A. Dixit, R. Katiyar, Z. Yu, R. Guo, and A. Bhalla, *Micro-Raman scattering and dielectric investigations of phase transition behavior in the BaTiO₃-BaZrO₃ system*. Journal of Applied Physics, 2001. **89**(12): 8085-8091.
202. Deluca, M., C.A. Vasilescu, A.C. Ianculescu, D.C. Berger, C.E. Ciomaga, L.P. Curecheriu, L. Stoleriu, A. Gajovic, L. Mitoseriu, and C. Galassi, *Investigation of the composition-dependent properties of BaTi_{1-x}Zr_xO₃ ceramics prepared by the modified Pechini method*. Journal of the European Ceramic Society, 2012. **32**(13): 3551-3566.
203. Li, W., Z. Xu, R. Chu, P. Fu, and G. Zang, *Dielectric and piezoelectric properties of Ba(Zr_xTi_{1-x})O₃ lead-free ceramics*. Brazilian Journal of Physics, 2010. **40**(3): 353-356.
204. Ciomaga, C.E., M.T. Buscaglia, V. Buscaglia, and L. Mitoseriu, *Oxygen deficiency and grain boundary-related giant relaxation in Ba(Zr,Ti)O₃ ceramics*. Journal of Applied Physics, 2011. **110**(11): 114110.
205. Philippot, G., E.D. Boejesen, C. Elissalde, M. Maglione, C. Aymonier, and B.B. Iversen, *Insights into BaTi_{1-y}Zr_yO₃ (0 ≤ y ≤ 1) Synthesis under Supercritical Fluid Conditions*. Chemistry of Materials, 2016. **28**(10): 3391-3400.
206. Ihlefeld, J., J. Maria, and W. Borland, *Dielectric and microstructural properties of barium titanate zirconate thin films on copper substrates*. Journal of Materials Research, 2005. **20**(10): 2838-2844.
207. Wu, Y.J., Y.H. Huang, N. Wang, J. Li, M.S. Fu, and X.M. Chen, *Effects of phase constitution and microstructure on energy storage properties of barium strontium titanate ceramics*. Journal of the European Ceramic Society, 2017. **37**(5): 2099-2104.
208. Irvine, J.T., D.C. Sinclair, and A.R. West, *Electroceramics: characterization by impedance spectroscopy*. Advanced Materials, 1990. **2**(3): 132-138.
209. Hennings, D., A. Schnell, and G. Simon, *Diffuse ferroelectric phase transitions in Ba(Ti_{1-y}Zr_y)O₃ ceramics*. Journal of the American Ceramic Society, 1982. **65**(11): 539-544.
210. Ciomaga, C., M. Buscaglia, M. Viviani, V. Buscaglia, L. Mitoseriu, A. Stancu, and P. Nanni, *Preparation and dielectric properties of BaZr_{0.1}Ti_{0.9}O₃ ceramics with different grain sizes*. Phase Transitions, 2006. **79**(6-7): 389-397.

List of publications and conferences

Peer-reviewed journals:

- **A. Tarasov**, V. V. Shvartsman, S. Shoja, D. Lewin, D. C. Lupascu, H. Wiggers, “*Spray-flame synthesis of $BaTi_{1-x}Zr_xO_3$ nanoparticles for energy storage applications*”. *Ceramics International*, 2020. **46**(9): 13915-13924.
- **A. Tarasov**, M. Rehosek, F. Marlow, H. Wiggers, “*Spray-flame synthesis of Sr-doped $BaTiO_3$ for photocatalytic hydrogen production*”, in preparation

Conferences:

- **A. Tarasov**, Y. Xiong, F. Marlow, C. Schulz, H. Wiggers, “*Spray-flame synthesis of barium titanate nanoparticles for photocatalytic applications*”, EMRS-2017. 2017: Strasbourg, France
- **A. Tarasov**, Y. Xiong, F. Marlow, C. Schulz, H. Wiggers, “*Spray-flame synthesis of barium titanate nanoparticles for electro- and photochemical applications*”, EAC-2017. 2017: Zürich, Switzerland
- **A. Tarasov**, M. Rehosek, F. Marlow, H. Wiggers, “*Spray-flame synthesis of $Ba_{1-x}Sr_xTiO_3$ nanoparticles for photocatalytic hydrogen production*”, MRS-2018. 2018, Boston, USA

Acknowledgements

Here I would like to express my gratitude towards the people, who helped me and supported me throughout the course of my work and without whom it would not have been possible to write this thesis.

First of all, I would like to thank my supervisors Prof. Dr. Christof Schulz and Prof. Dr. Hartmut Wiggers for giving me the opportunity to work at the University of Duisburg-Essen. Especially Hartmut Wiggers, who has been mentoring and advising me all these years, often providing excellent suggestions and ideas and sharing his personal experience. I also would like to thank my second advisor Dr. Frank Marlow for fruitful scientific discussions and helpful suggestions, frequently showing a new perspective on things.

Words are not enough how I would like to thank my wife for her nearly infinite patience, endless support, and understanding. The same applies to my parents, who have always supported, encouraged and never doubted me.

I am very grateful to Dr. Vladimir Shvartsman for very useful scientific recommendations and his help with dielectric measurements. I also wish to thank Dr. Yan Xiong and Marko Rehosek for the help with photocatalytic experiments.

I would like to thank my colleagues, with whom I had the pleasure to work with. I have really had a great time here with you. I want to thank Bariş for very intense and extremely helpful scientific discussions and with whom I shared my office for three years. A special thank you goes to Malini and Yusuf, who turned the last year of my PhD into an even more pleasant experience. and I would like to additionally acknowledge Bariş, Steven, and Malini for their precious time spent on XRD measurements. I also did not want to forget Adrian, Florian, and Samer for the nice occasions we had and help they provided.

A huge thank you is dedicated to the ICAN team, without whom material characterization would not have been possible. I therefore would like to thank Dr. Markus Heidelmann for the hours we spent in front of a TEM, Dr. Ulrich Hagemann for his support, discussions, and innumerable advices with XPS and Raman measurements, and Marcel Wienand for taking care of the organisational routine.

My former student Shayan Shoja also deserved to be mentioned here for the enormous work he carried out while working on his master thesis, which eventually has become a huge part of my work. I am grateful to Thomas Lange, who spent time reading the theory chapter on catalysis and suggested various improvements.

I am most grateful to Barbara Nota, who enormously helped me on my first days in Germany and throughout all these years. I am truly thankful to Ludger Jerig, Beate Endres, Natascha Schlösser, Birgit Nelius, Sebastian Rosendahl, Erdal Akyildiz, and Jörg Albrecht for the technical assistance they provided and casual conversations we had.

Lastly, I would like to thank SurMat doctoral program for providing financial support and Elke Gattermann for considering my application in the first place and being very helpful in various aspects.

DuEPublico

Duisburg-Essen Publications online

UNIVERSITÄT
DUISBURG
ESSEN

Offen im Denken

ub | universitäts
bibliothek

Diese Dissertation wird über DuEPublico, dem Dokumenten- und Publikationsserver der Universität Duisburg-Essen, zur Verfügung gestellt und liegt auch als Print-Version vor.

DOI: 10.17185/duepublico/71942

URN: urn:nbn:de:hbz:464-20200708-144228-2



Dieses Werk kann unter einer Creative Commons Namensnennung - Nicht kommerziell 4.0 Lizenz (CC BY-NC 4.0) genutzt werden.